Search for R-parity violating Supersymmetry in multi-lepton final states with the ATLAS detector

Dissertation
zur
Erlangung des Doktorgrades (Dr. rer. nat.)
der
Mathematisch-Naturwissenschaftlichen Fakultät
der
Rheinischen Friedrich-Wilhelms-Universität Bonn

von
Robert Michael Zimmermann
aus
Hamm

Bonn, März 2014

Dieser Forschungsbericht wurde als Dissertation von der
Mathematisch-Naturwissenschaftlichen Fakultät der Universität Bonn angenommen und ist
auf dem Hochschulschriftenserver der ULB Bonn
`http://hss.ulb.uni-bonn.de/diss_online` elektronisch publiziert.

1. Gutachter: Prof. Dr. Klaus Desch
2. Gutachter: Prof. Dr. Ian C. Brock

Tag der Promotion: 05.03.2014
Erscheinungsjahr: 2014

Contents

CHAPTER 1

Introduction

People have always been driven by curiosity going well beyond immediate necessity and asked questions of how or why things work and what they are made of. Experiences gained in experiments, ranging from the simplest trial and error to today's most advanced methods, have developed into a working understanding of the four forces governing our every day world. This working understanding has been met by theories thought up to explain or model the observations of the past and to make predictions for the future.

The currently accepted working theory for the gravitational force, governing the movement of falling apples as well as clusters of galaxies and predicting the existence of black holes, is the very successful theory of “General Relativity”. While obviously showing its presence, gravity is by far the weakest of the four forces at the typical energies and length scales we encounter in microcosm.

The other three forces are described by the “Standard Model” (SM) of particle physics. This theory contains a model for all electromagnetic phenomena, including electricity, magnetism and the propagation of light and is responsible for binding atoms and molecules to each other in chemistry and at even smaller scales binding electrons to the nucleus in atoms. Closely linked to and in the SM even combined with the electromagnetic force is the short-ranged weak force, mostly known as the cause of radioactivity, but also involved in fusion processes in the sun. Third is the strong force, which keeps protons and neutrons bound to each other in an atom's nucleus, overcoming the electric repulsion of the protons. At scales below that, it is also responsible for having the quarks and gluons combine into these protons and neutrons in the first place. Furthermore, the SM contains a mechanism for providing masses to the known elementary particles.

The predictions of both theories have been the target of extensive experimental scrutiny and found to be very precise, as necessary for today's applications for example in satellite-based global positioning or microelectronics.

Focussing on the SM, it was conceived in its current form in the 1970s, describing the combined electroweak and the strong interactions in a common mathematical framework. It was able to explain the observations made by prior experiments and predicted further elementary particles that were, with one exception, found by the year 2000 using high energy particle accelerators and detectors.

Despite its huge success, the SM still raises a number of questions, even beyond finding the, as of 2000, last missing particle, the Higgs boson. These questions are addressed by many different theories beyond the standard model (BSM), which are usually either direct extensions of the SM or try to embed it into more fundamental theories.

The Large Hadron Collider (LHC) was built to collide protons at center-of-mass energies of up to 14 TeV, expected to be in range of the mass of the SM Higgs boson as well as that of new elementary particles predicted by BSM theories. The first major goal was achieved in mid-2012 when the ATLAS and CMS experiments announced the observation of a SM-compatible Higgs boson in their detectors. More detailed studies of this boson as well as the search for BSM signals are still ongoing.

One BSM model which has been studied in much detail is “Supersymmetry” (SUSY). It proposes a symmetry between matter particles and force carriers and as a result predicts new elementary particles. This symmetry has to be broken, though, to explain why the new particles have not been seen so far. To still solve the Higgs mass related problems of the SM, as intended, many implementations of SUSY breaking predict at least some of the new particles to have masses at or below the TeV scale, in reach of the LHC.

A further prediction of SUSY is the possibility of rapid proton decay. As experimental observation places lower limits on the proton’s lifetime above 10^{29} years, in most cases an additional ad-hoc symmetry, called R-parity, is imposed on the models to forbid such decays. While this approach has so far been widely favored in experimental SUSY searches in ATLAS, it is not without equally well motivated alternatives.

The BC1 model was introduced as a benchmark for one class of such R-parity violating models, incorporating a non-standard candidate for the lightest SUSY particle and focussing on a part of parameter space not open in models with conserved R-parity. BC1 and some of the surrounding parameter space were previously studied only in simulations, though.

In this thesis, the phenomenological studies of this parameter space are extended and the predictions of the simulation are confronted with the first $2\,\text{fb}^{-1}$ of data taken with the ATLAS detector in 2011. This is done by interpreting the results of a search for new physics in final states with multiple leptons and missing transverse momentum.

The thesis is structured as follows: Chapter 2 will introduce the LHC and the ATLAS detector, which were used to collect the experimental data for the search. Chapter 3 will start with a brief overview of the SM, including some of its open questions. This will be followed by an introduction to SUSY, R-parity violation and the benchmark point BC1. Chapter 4 will describe the analysis devised for the search in detail. Chapter 5 will provide a phenomenological overview of the BC1 model and the surrounding parameter space, and will show the results of interpreting the findings of the analysis in terms of these models. Chapter 6 finally will contain a short summary and some conclusions.

CHAPTER 2

Accelerator and Detector

Probing small scales requires high energies. In elementary particle physics, these energies are typically achieved by colliding particles, either in particle beam on target or beam on beam configurations. The desired information then has to be extracted from the scattering products. To undertake such experiments on the one hand a source of high energy particles is required. Due to the small probability of the events that are of most interest to particle physicists today, these colliding particles usually have to be provided by a particle accelerator to reach the necessary energies and to observe sufficient numbers of the studied type of event. On the other hand, detectors capable of measuring the properties of the particles produced in the collision with a suitable precision are required as well.

This chapter will introduce the Large Hadron Collider (LHC) and the main detector experiments built to study its output in Sec. 2.1. This will be followed by a closer look at the ATLAS detector and its components in Sec. 2.2, which provided the data analyzed for this thesis.

2.1 The Large Hadron Collider

The LHC [1] is a ring accelerator with a circumference of 26.7 km, located roughly 100 m underground, at the Franco–Swiss border near Geneva. It is part of the CERN[1] accelerator complex, schematically shown in Fig. 2.1. Following pre-acceleration in the LINAC, PS and SPS stages of the complex, two counter-rotating beams consisting of protons or heavy ions (lead nuclei) are injected into the two rings of the LHC at energies of 450 GeV. After further acceleration up to the final center-of-mass energy of 7 TeV to 14 TeV for the run, the particle bunches that make up these beams can then be brought to collisions at a number of interaction points.

Four of the interaction points are equipped with major detectors. Two of these, ATLAS [3] and CMS [4], are multipurpose experiments, built to search for the Higgs boson and to be able to measure a broad range of signatures expected from processes beyond the current standard

---

[1] European Organization for Nuclear Research

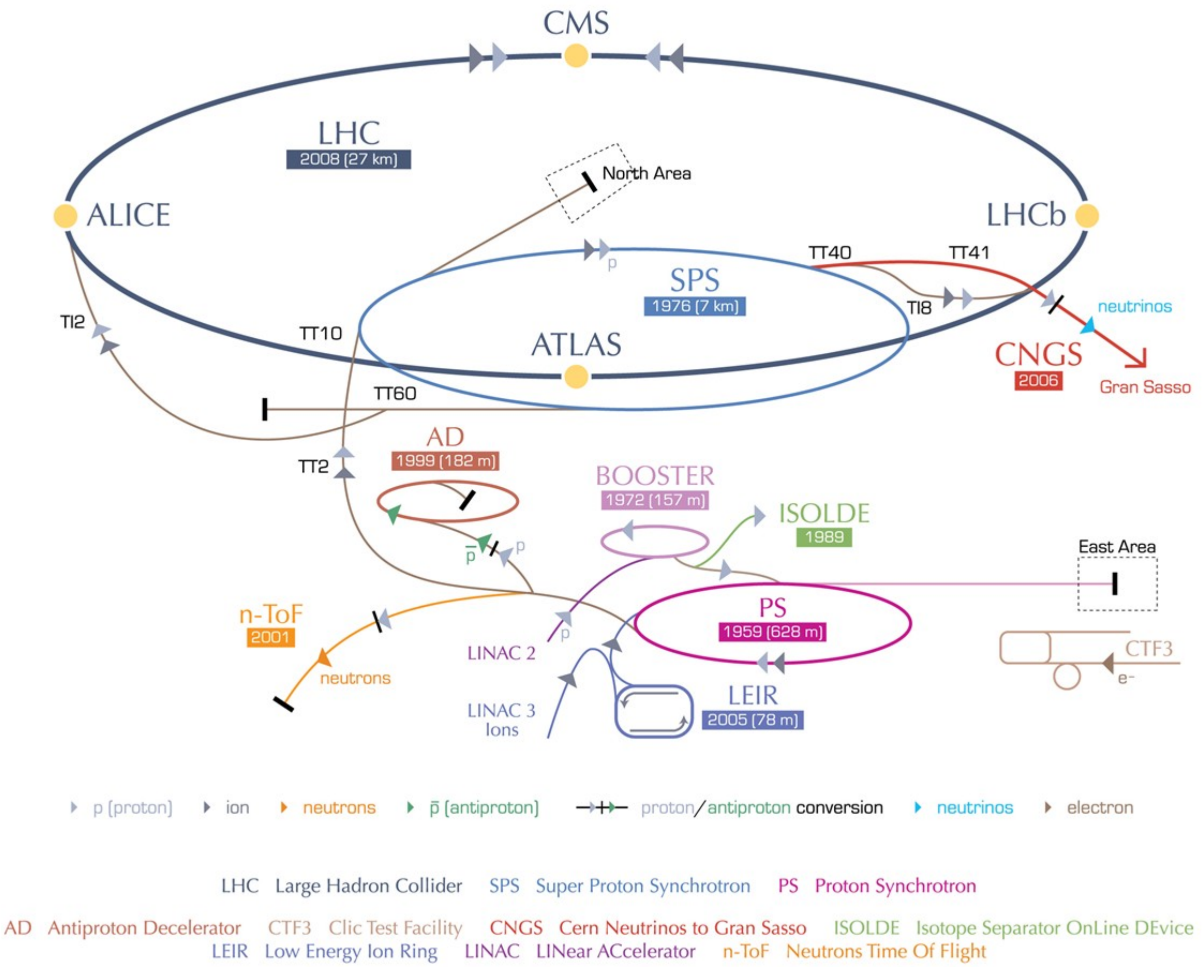

Figure 2.1: Schematic view of the CERN accelerator complex. [2]

model. Employing different solutions for the same problems, they are able to cross-check each other. The LHCb [5] experiment is dedicated to B-physics and CP-violation, featuring a detector with forward angular coverage only. The ALICE [6] detector was designed to investigate the quark–gluon plasma that is expected to be created in heavy ion collisions.

In addition there are a number of smaller detectors. The TOTEM [7] experiment's goal is to measure the total *pp* cross section and study elastic and diffractive scattering. Its detectors are located in the (very) forward region of CMS and are technically integrated into the bigger experiment. The LHCf [8] experiment's detectors were located ±140 m from ATLAS. They were designed to measure neutral particle production at very small angles to provide input for modeling cosmic ray showers in the atmosphere. They were removed in July 2010 after successful data-taking and upgrades for future operations are planned. The MoEDAL [9] experiment is the newest of the LHC experiments. It was approved in 2010 and will share the interaction point of LHCb, covering the opposite hemisphere. It was designed to search for magnetic monopoles and other highly ionizing (pseudo)stable massive particles.

The LHC was built to probe physics at very small scales, among other things by searching for the last missing part of the SM, the Higgs boson, or by hunting for new heavy particles and

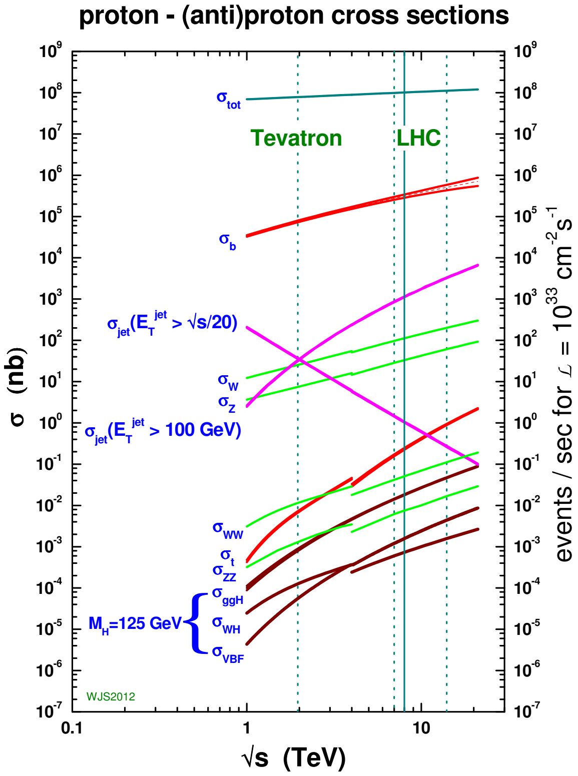

Figure 2.2: Standard Model cross sections as a function of the collider energy, including a 125 GeV Higgs boson [10]. The discontinuity of some curves is due to differences between $p\bar{p}$ (left) and pp (right) collision cross sections.

resonances, predicted by its extensions. The rate $R_{pp\to X}$ at which any such event is produced is given by

$$R_{pp\to X} = \mathcal{L} \cdot \sigma_{pp\to X} \tag{2.1}$$

where $\mathcal{L}$ is the instantaneous luminosity and $\sigma_{pp\to X}$ is an energy-dependent cross section, giving the probability to produce this type of event.

While a high instantaneous luminosity seems favorable, it comes at the cost of a so-called "pileup" of events, which has to be taken into account in simulation and analysis (cf. Secs. 4.2 and 4.4.5). Regarding the energy, a basic problem of hadron colliders like the LHC is the fact that protons have a substructure. According to the QCD factorization theorem (cf. Sec. 3.1.1), the protons' constituents, the so-called partons, can be viewed as the particles actually colliding to produce the observed final states. They only carry the fractions $x_{1/2}$ of the protons' momenta, though, effectively reducing the center-of-mass energy available for the hard interaction by a factor of $\sqrt{x_1 x_2}$.

Examples of SM cross sections and the corresponding event rates are given in Fig. 2.2 for different LHC energies, as well as for the proton–anti-proton collider Tevatron [11] at Fermilab. As shown in the figure, the cross sections generally increase towards higher center-of-mass energies, $\sqrt{s}$, with some of the rarer processes even gaining an order of magnitude between the two accelerators.

The LHC was designed to provide energies of up to 14 TeV in proton–proton collisions, a peak luminosity of $10^{34}\,\mathrm{cm}^{-2}\,\mathrm{s}^{-1}$ with 1.15×10^{11} protons per bunch and a bunch spacing of 25 ns. The energy will be limited by the 8.33 T superconducting magnets necessary to keep the beams in their orbits, while the luminosity depends on beam parameters like the number of bunches per beam, the number of protons per bunch and the sizes of the beam profiles (see Eq. 2.2), which allow for some tuning.

The accelerator has been successfully delivering beams since Nov. 2009, starting with runs at $\sqrt{s} = 900\,\mathrm{GeV}$ and 2.36 TeV, running at 7 TeV in 2010 and 2011 and reaching 8 TeV in 2012. During these three years maximum peak instantaneous luminosities of $2 \times 10^{32}\,\mathrm{cm}^{-2}\,\mathrm{s}^{-1}$, $3.6 \times 10^{33}\,\mathrm{cm}^{-2}\,\mathrm{s}^{-1}$ and $7.7 \times 10^{33}\,\mathrm{cm}^{-2}\,\mathrm{s}^{-1}$ were reached, respectively. While at design parameters the LHC beam can provide a maximum of 2808 bunches for collisions with a spacing of 25 ns, for the 2011/12 runs a bunch spacing of 50 ns was chosen, allowing for a maximum of 1380 colliding bunches.

A further increase of the center-of-mass energy to its design value of 14 TeV is planned after a longer technical shutdown in 2013/14.

2.2 The ATLAS Detector

The ATLAS[2] detector [3, 12, 13] is one of the general-purpose experiments at the LHC, designed to observe a variety of potential new physics phenomena predicted at the TeV scale and at the same time allowing for a precise measurement of Standard Model parameters at the LHC's unprecedented collision energies.

A cut-away view of the detector is shown in Fig. 2.3. Surrounding the nominal interaction point inside the beam pipe at its center, it contains sub-detectors for precision tracking, including (secondary) vertexing and momentum measurement, as well as calorimeters for measuring the energies of particles and jets, while the outermost part is designed for the detection of muons. The magnetic field necessary for the momentum measurements in the inner tracking detectors is provided by a solenoid magnet, while further out toroid magnets allow the muon tracking to work independently. To cover as much of the solid angle as possible the detector layers are arranged cylindrically in the central, so-called barrel region and perpendicular to the beam axis in the so-called end-caps, with overlap in many places and the highest coverage realized by the calorimeters. With a length of about 44 m and a diameter of about 25 m the ATLAS detector is the largest experiment at the LHC, while 7000 t are not enough to make it the heaviest.

Using the nominal interaction point (IP) as origin, the z-axis of the ATLAS coordinate system is defined to point along the beam direction, the positive x-axis towards the center of the LHC ring and the positive y-axis upwards, completing the orthogonal system. The azimuthal angle ϕ is measured in the x–y or "transverse" plane. Since the longitudinal component of the initial momentum is usually not known, the transverse components of the momentum, $p_\mathrm{T} = \sqrt{p_x^2 + p_y^2}$, and (missing) energy, $E_\mathrm{T}^{(\mathrm{miss})}$, are often used. The polar angle θ is measured from the beam axis,

---

[2] A Toroidal LHC ApparatuS

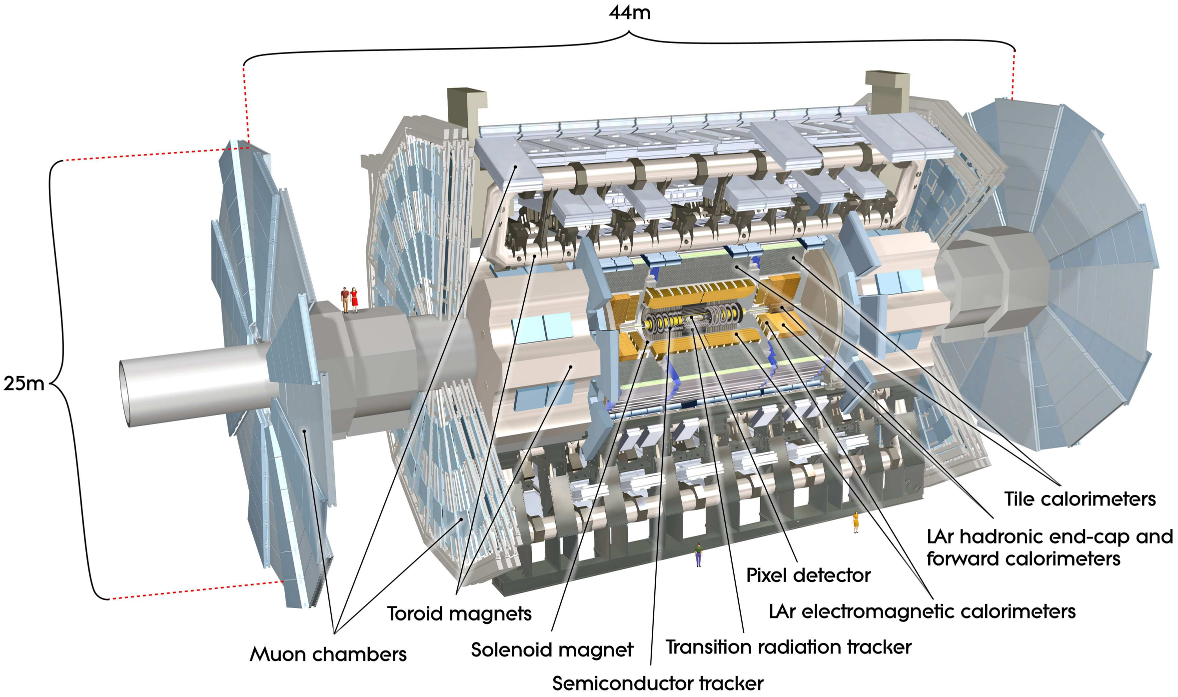

Figure 2.3: Cut-away view of the ATLAS detector. [3]

while the so-called pseudorapidity is defined as $\eta = -\ln\tan(\theta/2)$. Finally, distances between objects in the η–ϕ plane are measured by $\Delta R = \sqrt{(\Delta\eta)^2 + (\Delta\phi)^2}$.

The main detector components will be summarized in the following sections. Further details as well as information on support systems and structures can be found in the references given above.

2.2.1 The Inner Detector

A cut-away view of the Inner Detector is shown in Fig. 2.4. Its three independent sub-detectors are located within a cylindrical volume of about 1 m radius and about 6 m length around the beam pipe. Starting from the inside these are the Silicon Pixel Detector (Pixel), the Semiconductor Tracker (SCT) and the Transition Radiation Tracker (TRT). Their task is to sample the trajectories of charged particles with high precision, such that the “tracks” of these particles can be reconstructed later using pattern recognition algorithms. Extrapolating these tracks back inwards then allows finding the primary and secondary interaction points or “vertices” of the collision event(s). The inner detector is surrounded by a superconducting solenoid, which creates a homogeneous 2 T magnetic field parallel to the beam direction, deflecting particles in ϕ. By measuring the curvature of the tracks it is then possible to calculate the momentum of the particles. In addition to basic tracking the TRT helps to identify electrons by also detecting transition radiation.

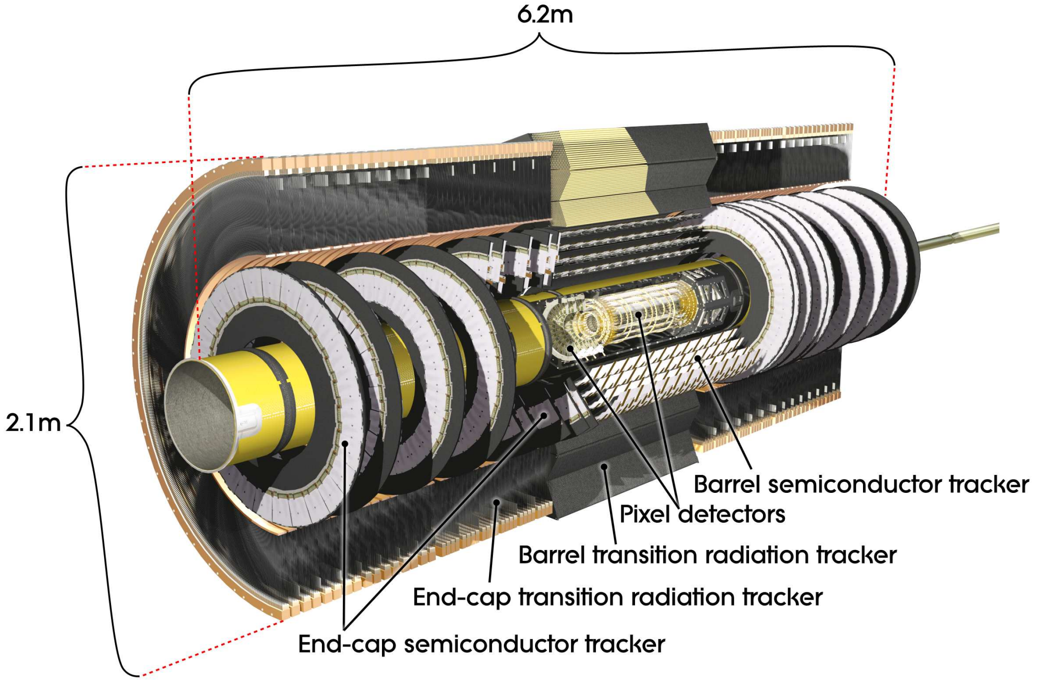

Figure 2.4: Cut-away view of the ATLAS Inner Detector. [3]

The Silicon Pixel Detector

The Pixel Detector is a precision silicon tracking detector with high granularity in R–ϕ and z and covers pseudorapidities up to 2.5. It consists of three concentric cylinders around the beam axis in the barrel, with the innermost sensitive layer at a radius of around 5 cm, very close to the outer edge of the beam pipe at 3.6 cm. In both end-caps the sensitive layers take the shape of three discs perpendicular to the beam axis, such that a typical track crosses three layers over the full $|\eta|$ range of the inner detector. The intrinsic accuracy of the Pixel Detector is 10 µm in R–ϕ and 115 µm in z or R for barrel or end-caps, respectively.

The Semiconductor Tracker

The SCT is a silicon micro strip detector consisting of four concentric cylinders around the beam axis in the barrel and nine discs perpendicular to the beam axis in each end-cap. It has the same angular coverage as the Pixel Detector, but achieves its accuracy in z or R by combining two strip layers positioned at a stereo angle of 40 mrad with respect to each other to get one space point. With this setup the information of four such space points is typically available for pattern matching for a track traversing this sub-detector. The SCT's intrinsic accuracy is 17 µm in R–ϕ and 580 µm in z or R for barrel or end-caps, respectively.

The Transition Radiation Tracker

The TRT contains many single wire drift tubes (“straws”) interleaved with material that can emit transition radiation photons. The orientation of the straws is axial in the 73 barrel planes and radial in the 160 end-cap planes. The TRT only covers $|\eta|$ up to 2.0 and has an electrical division near $z = 0$, but typically collects 30 hits for an average track. The TRT has an intrinsic accuracy of 130 µm in R–ϕ and does not provide z information, apart from which half-barrel was hit, but still contributes significantly to the momentum measurement with the much higher number of hits and a longer lever arm than the two silicon detectors. Signals created in the straws by transition radiation photons, which are larger than those created by tracking hits, provide additional information for electron identification.

2.2.2 The Calorimeter

Continuing outwards there are the sampling electromagnetic and hadronic calorimeters, a cut-away view of which can be seen in Fig. 2.5. The individual sub-detectors are the Electromagnetic Calorimeter (EMCal), the Scintillator Tile Calorimeter (Tile), the Liquid Argon Hadronic End-Cap Calorimeter (HEC) and the Forward Calorimeter (FCal). Their task is to measure the energy and direction of outgoing charged and neutral particles up to $|\eta| = 4.9$. The high granularity of the EMCal in the η-region matching the inner detector is ideal for measuring electrons and photons, while the coarser granularity in the remaining calorimeter is sufficient for a good measurement of jets and missing transverse energy ($E_\mathrm{T}^\mathrm{miss}$). The whole calorimeter provides a total thickness equivalent to at least ten interaction lengths. This is enough to deliver a good resolution for high energy jets and to reduce the so-called “punch-through” such that it does not influence the muon measurement further out. The EMCal provides at least 22 and 24 radiation lengths in the barrel and end-caps, respectively.

The Electromagnetic Calorimeter

The EMCal uses liquid Argon (LAr) as active material and lead absorber plates. It has accordion-shaped electrodes to provide ϕ symmetry without azimuthal cracks and consists of two half-barrel parts, covering $|\eta|$ up to 1.475 and two end-caps, covering $|\eta|$ between 1.375 and 3.2. Radially it extends from 1.4 m to 2 m. It has three layers in the precision physics region of $|\eta|$ up to 2.5, which includes the cylindrical barrel and the radially outer of two coaxial wheels in the end-caps, while the inner wheels have only two layers and a lower lateral granularity. The first layer is finely segmented in η to allow accurate position measurements, e.g. of photons. A thin pre-sampler detector in front of the inner calorimeter surface, made of an active LAr layer allows correcting for energy losses of electrons and photons before reaching the calorimeter for $|\eta|$ up to 1.8 (overlapping the HEC).

The Scintillator Tile Calorimeter

The Tile calorimeter, located outside the EMCal, is a hadronic calorimeter with steel as absorber and scintillator tiles as active material. It consists of a barrel part, covering $|\eta|$ up to 1.0 and

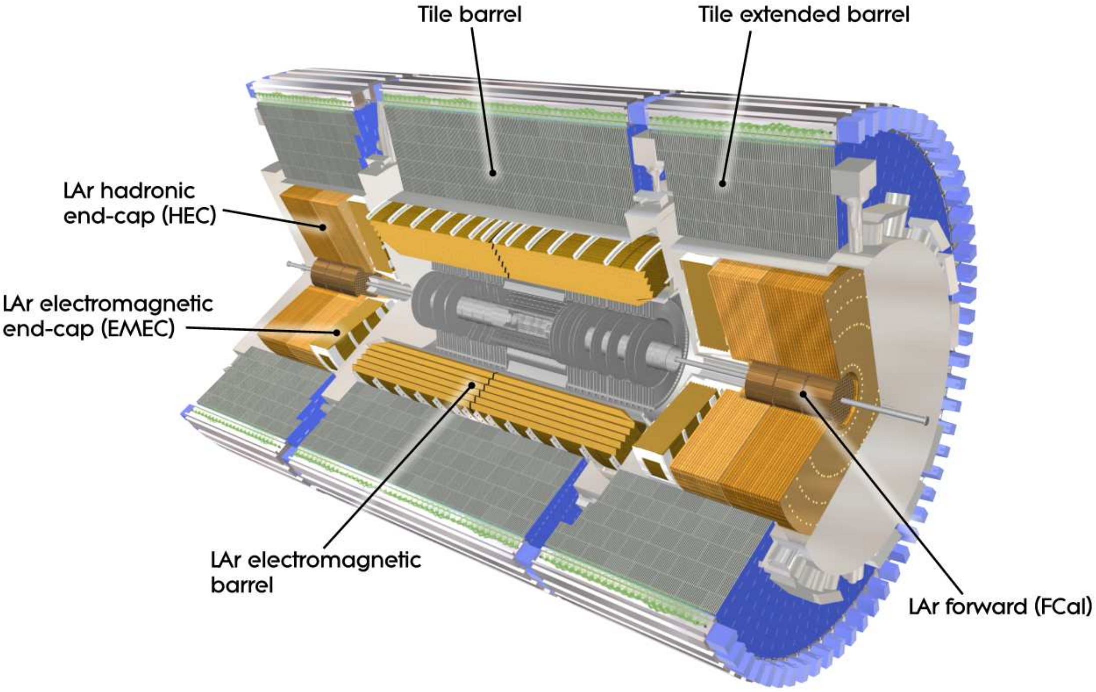

Figure 2.5: Cut-away view of the ATLAS Calorimeter. [3]

two extended barrel parts, covering $|\eta|$ between 0.8 and 1.7. It provides about 7.4 interaction lengths in three layers between 2.28 m and 4.25 m radius from the interaction point.

LAr Hadronic End-Cap Calorimeter

The HEC is located outside the EMCal's end-caps and is using copper as the absorber and LAr as active material. It covers $|\eta|$ between 1.5 and 3.2, overlapping with Tile and FCal to reduce the drop in material density in those areas. Radially it extends from 0.475 m (0.372 m where it overlaps with FCal) to 2.03 m. The HEC consists of two wheels, providing a total of four layers per end-cap, with the wheel closer to the IP having higher granularity. It also has the ability to detect muons.

The Forward Calorimeter

The FCal covers the forward region of $|\eta|$ between 3.1 and 4.9. As it has to cope with high particle fluxes it is recessed in z by about 4.7 m from interaction point, while still providing a thickness of ten interaction lengths. It consists of three layers per end-cap, the innermost optimized for electromagnetic showers and using copper as absorber material, the outer two for hadronic ones, using tungsten as absorber. Because of its intrinsic radiation hardness LAr is used as active material for the whole FCal.

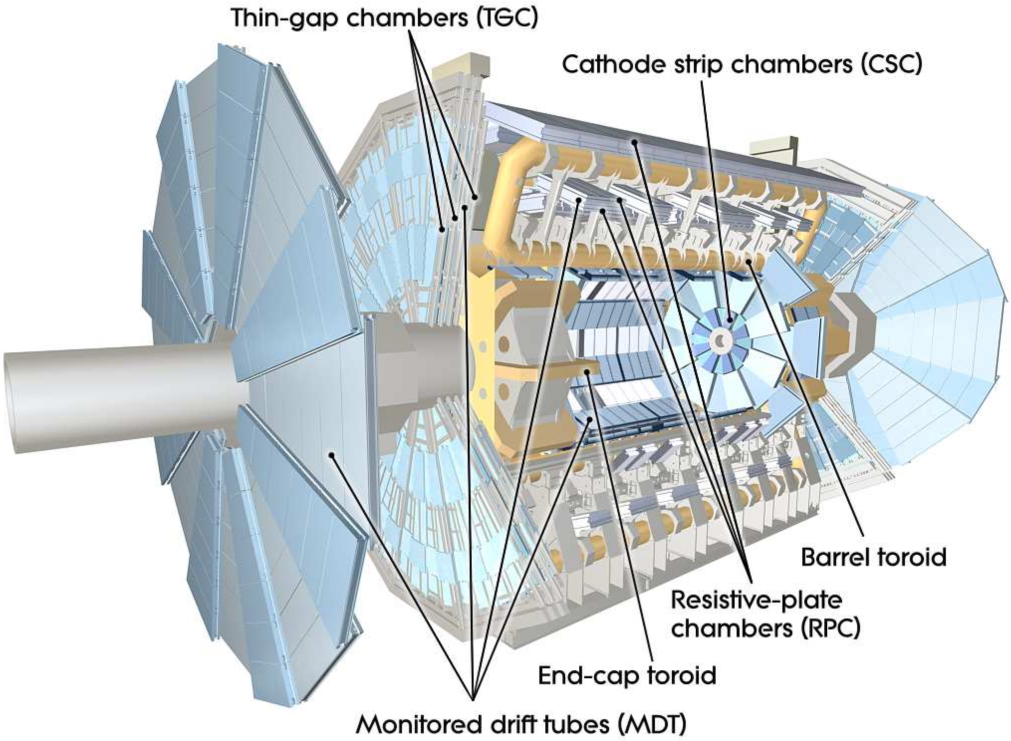

Figure 2.6: Cut-away view of the ATLAS Muon Spectrometer. [3]

2.2.3 The Muon Spectrometer

The outermost sub-detector is the muon spectrometer, shown in Fig. 2.6. The three essential design criteria for the muon spectrometer were a reliable beam-crossing identification, fast triggering on muon tracks up to $|\eta| = 2.4$ and good stand-alone muon transverse momentum (p_T) measurement. There are four types of muon chambers to provide these capabilities. For the high precision measurement there are the Monitored Drift Tube Chambers (MDT) and the Cathode Strip Chambers (CSC), while for triggering there are the Resistive Plate Chambers (RPC) and Thin Gap Chambers (TGC). To provide the magnetic field necessary for the momentum measurement in the muon system, superconducting air-core toroid magnets are part of the ATLAS detector design. The main barrel toroid bends tracks in the $|\eta|$-range up to 1.4 with an average field of 0.5 T, the two end-cap toroids for tracks with $|\eta|$ between 1.6 and 2.7 have an average strength of 1 T. They create a toroidal magnetic field deflecting in η-direction. The precision tracking chambers in the barrel are located between the eight coils of the magnet, as shown in the figure, while they are in front of and behind the magnet in the end-caps. The timing resolution of the trigger chambers is between 1.5 ns and 4 ns.

Monitored Drift Tube Chambers

The MDT chambers deliver the main precision track coordinate measurement in the principal bending direction for barrel and end-caps in the pseudorapidity range up to 2.7 (2.0 in innermost end-cap layer). In the barrel the MDT has three concentric cylindrical shells of chambers, at radii of 5 m, 7.5 m and 10 m. In the end-caps there are four layers of wheels, perpendicular to the beam axis, at z of about 7.4 m, 10.8 m, 14 m and 21.5 m, with typical muon tracks crossing three of the chambers. Each chamber has three to eight layers of drift-tubes with an average resolution of 35 µm per chamber. Since alignment is very important to achieve the design performance, it is checked within and between chambers using a high-precision laser-based system.

Cathode Strip Chambers

The CSC is used as the innermost layer of precision muon tracking in the forward region of both end-caps with $|\eta|$ from 2 to 2.7 and is designed to cope with the expected higher fluxes. In contrast to the MDT, multi-wire proportional chambers with cathodes segmented into strips are employed in the CSC. Each end-cap has four planes of strips and allows measuring both coordinates by correlating two orthogonal strips. Using this a resolution of 40 µm in the bending plane and 5 mm in the transverse plane can be achieved.

Resistive Plate Chambers

The RPCs are fast trigger chambers located in the barrel region, covering $|\eta|$ up to 1.05. They are gaseous parallel electrode-plate detectors. Two layers of RPCs surround the middle MDT layer, while one is either close to the inside or outside of the outer MDT layer, depending on sector in ϕ. The average chamber resolution is 10 mm in z and ϕ.

Thin Gap Chambers

The TGCs extend the coverage of fast trigger chambers to the end-caps in the $|\eta|$ range from 1.05 to 2.4 They're based on the same principle as multi-wire proportional chambers. The TGCs have four layers per end-cap. One layer is located in front of the inner MDT layer, the next two surround the middle MDT layer and the last is a bit further out. The average chamber resolution is 2 mm to 6 mm in R and 3 mm to 7 mm in ϕ.

Together with the RPCs, the TGCs allow for reliable beam-crossing identification with at least 99 % probability. They also provide a fast and coarse measurement of both coordinates for the high-level trigger. Using the bending plane coordinate to match the MDT, the trigger chamber's perpendicular coordinate is also adopted as second coordinate for the muon tracks.

2.2.4 Luminosity Measurement

In order to convert between cross sections and event rates it is essential to know the luminosity. The LUCID (Luminosity measurement using Cherenkov Integrating Detector) detector was designed as the main online relative luminosity monitor. It is a Cherenkov detector located ±17 m from the interaction point, at a radius of 10 cm from the beam pipe and detects charged particles produced in inelastic proton–proton scattering in the forward direction ($|\eta|$ about 5.8). While the primary purpose of the Beam Condition Monitor (BCM) is to monitor background

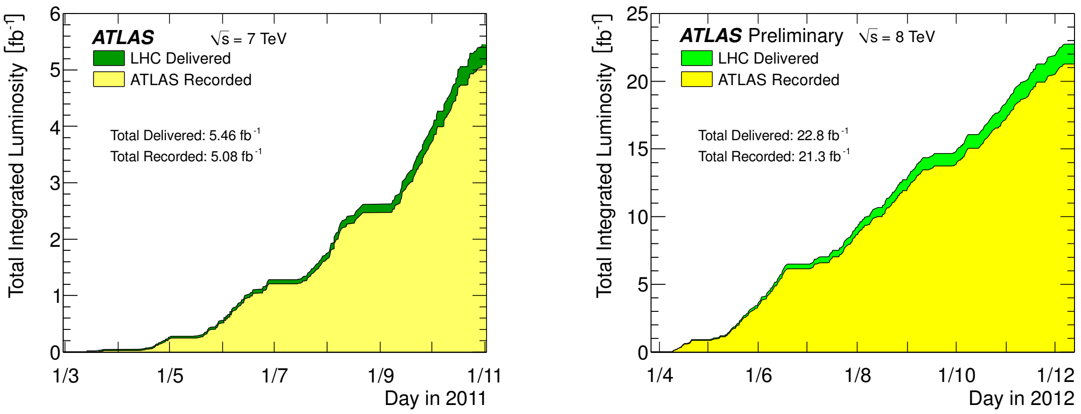

(a) (b)

Figure 2.7: Total integrated luminosity for (a) $\sqrt{s} = 7\,\text{TeV}$ in 2011 and (b) 8 TeV in 2012. [17]

levels and issue beam-abort requests in case of beam losses, its fast readout also allows measuring the relative bunch-by-bunch luminosity. The BCM consists of four small diamond sensors on each side of the beam pipe at $z = \pm 184\,\text{cm}$ and $|\eta| = 4.2$.

The absolute luminosity can be expressed using measurable beam parameters as follows:

$$\mathcal{L} = f_r \frac{n_b n_1 n_2}{2\pi \Sigma_x \Sigma_y} \tag{2.2}$$

where f_r is the revolution frequency (11 246 Hz), n_b the number of colliding bunches, $n_{1/2}$ the number of particles in the colliding bunches and $\Sigma_{x/y}$ are measures of the horizontal and vertical beam profiles[3]. By performing so-called “van-der-Meer” scans, in which beam separations are varied in known step sizes and the resulting changes in collision rates are recorded (e.g. in LUCID), $\Sigma_{x/y}$ can be measured.

Details on the algorithms and additional sub-detectors used for the luminosity measurement can be found in [14–16].

The total integrated luminosities recorded by ATLAS at $\sqrt{s} = 7\,\text{TeV}$ in 2010 and 2011 were $45.0\,\text{pb}^{-1}$ and $5.08\,\text{fb}^{-1}$, respectively. Another $21.3\,\text{fb}^{-1}$ were taken at 8 TeV in 2012. Together this corresponds to a total of about 1.8×10^{15} total proton–proton collisions. This was very close to the luminosity delivered by the LHC, as can be seen in Fig. 2.7, taken from [17]. The delivered luminosity here is the one measured between the start of stable beams, as declared by LHC, and ATLAS putting the detector in “safe standby” mode prior to a beam dump or beam studies. The difference to the recorded luminosity is due to inefficiencies of the data acquisition as well as startup times for high-voltage and preamplifiers in the ATLAS tracking detectors.

The design goal for the relative uncertainty of the measurement of the instantaneous luminosity of less than 5 % was met already for the 2011 data, where 3.7 % was achieved [14], with the measurement of the bunch-charge product ($n_1 \cdot n_2$ in Eq. 2.2) being the dominant contribution.

---

[3] In case of Gaussian beam profiles the $\Sigma_{x/y}$ would be their standard deviations.

2.2.5 The Trigger System

At a design event rate of 40 MHz it is not possible to read out and store all events. To get this rate down to the roughly 200 Hz the offline storage can handle, the ATLAS detector employs a three level trigger system, that searches for interesting signatures, dropping other events in the process.

Level-1 Trigger

Level-1 (L1) is a hardware trigger implemented using electronics designed for this purpose. It uses information from a subset of detectors (muon trigger chambers and all calorimeter sub-detectors) with reduced granularity and searches for signatures from high-p_T muons, electrons/photons, jets, hadronically decaying τ leptons or global quantities, like large overall E_T or $E_\mathrm{T}^\mathrm{miss}$, but only decides based on simple quantities like multiplicities or thresholds. For events passing, it flags so called Regions of Interest (RoI) for the higher level triggers. L1 has to reduce the event rate to a maximum of 75 kHz and provide this decision within 2.5 µs.

Level-2 Trigger

The Level-2 trigger (L2) builds and uses additional information from the RoIs for events passing L1. It can utilize the full granularity and precision in these regions and uses coordinates, energies and types of signatures to make its decision and has to reduce the event rate to below 3.5 kHz. The average processing time per event is about 40 ms.

Event Filter

The Event Filter (EF) uses the offline analysis procedures to fully build all events that passed L2. Only events passing the EF are recorded to disc and later to tape. For this the event rate has to be reduced to about 200 Hz. Processing an event at EF level on average takes about 4 s of processing time and produces $\mathcal{O}(1)$ MB of event output for later analysis.

L2 and EF together are called the High-Level Trigger (HLT) and are both implemented in software and run on off-the-shelf servers.

To allow for optimal use of the available bandwidth, it is possible to “pre-scale” the trigger decisions individually on all levels by discarding an adjustable fraction of otherwise passing events. While this is obviously undesirable for searches for new physics, higher luminosities and numbers of interactions per bunch crossing require either pre-scaling or increasing the thresholds of existing trigger items, as long as “smarter” triggers are not available.

Finally events are sorted into different (possibly overlapping) data “streams” depending on what triggered them. Apart from dedicated streams for performance studies, the streams typically used for physics analysis are called Egamma, Muons and JetTauEtmiss, which are filled by electron/photon, muon and jet/τ/$E_\mathrm{T}^\mathrm{miss}$ triggers, respectively.

CHAPTER 3

Theory

Theory and experiment are complementary. While the theoretical side of particle physics tries to explain and model the observations made by the experiments with the goal of being able to provide further predictions, it also requires the experimental results as input to determine the values of its parameters as well as to support or falsify additions to the model.

Section 3.1 will give a brief overview of the current standard model of particle physics, touching some of its basic concepts, the particles it describes and the forces that govern their interactions in Secs. 3.1.1 and 3.1.2, as well as the mechanism generating the particle masses in Sec. 3.1.3. This will be followed by a short account of some of the unsolved questions of the Standard Model in Sec. 3.1.4.

Section 3.2 will go beyond the Standard Model, introducing the notion of Supersymmetry as a potential solution to some of the open questions. The “minimal” supersymmetric extension to the Standard Model will be introduced in Secs. 3.2.1 and 3.2.2, followed by a description of some important changes to the Standard Model behavior in Secs. 3.2.3 and 3.2.4. In Sec. 3.2.5 a constrained version of the minimal supersymmetric extension will be introduced, which will be the basic framework for a summary of the production processes of new supersymmetric particles in Sec. 3.2.6 as well as for the discussion about the so-called “R-parity” in Sec. 3.2.7. Finally an example of an R-parity violating supersymmetric model will be provided in Sec. 3.2.8, leading to a possible signature to be studied with ATLAS data in the following chapters.

3.1 The Standard Model of Particle Physics

The Standard Model (SM) of particle physics describes our current understanding of the basic building blocks of matter and their interactions on small scales. The model can explain the electromagnetic force as well as the weak and strong forces and its predictions have successfully been tested to very high precision in many experiments. The SM contains two categories of particles: fermions, carrying half-integer spin, providing the elementary constituents of matter and bosons, carrying integer spin, responsible for mediating the interactions between them. Starting with the latter, the electromagnetic force is represented by the photon (γ), the weak

Name	Q	Mass			
electron neutrino	0	< 2			eV
electron	-1	510.998 928	±	0.000 011	keV
muon neutrino	0	< 2			eV
muon	-1	105.658 371 5	±	0.000 003 5	MeV
tau neutrino	0	< 2			eV
tau	-1	1776.82	±	0.16	MeV
up	$\frac{2}{3}$	2.3		$^{+0.7}_{-0.5}$	MeV
down	$-\frac{1}{3}$	4.8		$^{+0.7}_{-0.3}$	MeV
charm	$\frac{2}{3}$	1.275	±	0.025	GeV
strange	$-\frac{1}{3}$	95	±	5	MeV
top	$\frac{2}{3}$	173.5	±	0.6 ± 0.8	GeV
bottom	$-\frac{1}{3}$	4.18	±	0.03	GeV
gluon	0	0			eV
photon	0	$< 10^{-18}$			eV
$W^{\pm}$ bosons	± 1	80.385	±	0.015	GeV
Z^0 boson	0	91.1876	±	0.0021	GeV
Higgs boson	0	125.9	±	0.4	GeV

Table 3.1: Particle content of the Standard Model, including the electric charges and masses as given in [18]. The gluon mass corresponds to the theoretical value. For the Higgs boson mass the value from the 2013 partial update of the 2014 edition of [18] is given.

force by the $W^{\pm}$ and Z^0 bosons and the strong force by eight gluons (g). In addition the SM contains one Higgs boson (h) which is related to the way the masses of the other SM particles are generated. The fermions consist of leptons and quarks. Of the six leptons, three only interact via the weak force while the other three carry electric charge and interact electromagnetically as well. The six quarks in contrast feel all three forces. Leptons as well as quarks can be grouped into three families (or generations) each, with identical quantum numbers, but different masses. Table 3.1 summarizes the particle content of the Standard Model including the electric charges and approximate masses. The model also describes the charge conjugate states of same spin and mass, the so-called anti-particles.

From a theory point of view the SM is formulated in the form of a relativistic quantum field theory. As in all other fields of physics, symmetries and their associated invariants have shown to be an excellent tool in explaining many of the properties of the SM. The first required symmetry is an invariance of the action or the corresponding Lagrangian density under transformations of the Poincaré group (i.e. space-time translations, rotations and boosts), resulting in the same equations of motion in all inertial frames. Next, starting with a theory of free massless fermion fields only, the requirement of invariance under local gauge symmetries (i.e. independent phase shifts and internal rotations of the fields at every point in space-time) automatically introduces gauge fields, whose quanta mediate forces between the original fields. The gauge groups reproducing the experimentally observed phenomenology of the SM are $SU(3)_C \times SU(2)_L \times U(1)_Y$.

An important feature of the SM, caused by its gauge symmetries, is its renormalizability. Computing measurable quantities like masses, cross sections, decay rates, etc. perturbatively beyond the lowest order requires evaluating Feynman diagrams involving particle loops. While naively these loop diagrams diverge, for renormalizable theories these divergencies vanish, when re-expressing the so-called “bare” couplings and masses in the original Lagrangian in terms of measured values. In this way, higher-order contributions to propagators can be included in renormalized masses, while contributions to interaction vertices can be included in couplings (an effect that is sometimes referred to as “integrating out” the high energy or small length-scale details of the theory). The remaining finite contributions usually come in the form of large logarithms, which can be included by treating couplings and masses appearing in the Lagrangian as “running” parameters. Different choices of how these logarithms are treated lead to different renormalization schemes.

This renormalization procedure introduces a renormalization scale μ_R via the measurements. While different choices of this scale will lead to different expansions, in the end physical observables must be independent of this scale. This requirement gives rise to scaling laws for the couplings and masses, the so-called renormalization group (RG) equations, which depend on the details of the theory. The solutions of these equations then allow the prediction of the renormalized parameters at one scale, given a set of values at another.

The next three sections will provide some more details concerning the strong and electroweak forces and introduce the Higgs mechanism, which generates masses for the vector bosons and fermions in the SM. (For additional introductory material see e.g. [19–21]). Following that, some of the questions not addressed or solved by the SM will be discussed, before focussing on Supersymmetry as one possible theory beyond the Standard Model (BSM), which provides answers to some of the open questions.

3.1.1 The Strong Force

The theory of the strong force or “quantum chromodynamics” (QCD) [22] is given by the invariance of the SM Lagrangian under local $SU(3)_C$ transformations[1]. This requires an octet of gauge bosons, the gluons g, coupling to the six quarks, which are often divided into up- and down-type quarks, when only electric charge or weak isospin (cf. Sec. 3.1.2) are important. In contrast to the electrically neutral photon for electromagnetism, the gluons, because of the non-Abelian nature of the gauge group, carry “color” charges and also couple to themselves.

One consequence of this self-coupling is that the running QCD coupling α_s is small at high energies, leading to the “asymptotic freedom” of quarks, but becomes large for low energies, which prevents perturbative QCD calculations in this regime, because the Lagrangian can no longer be expanded in terms of the coupling. A summary of measurements of α_s, together with the QCD prediction is shown in Fig. 3.1.

Caused by the large coupling at low energies quarks form color-neutral bound states, called hadrons. One possibility for this are quark–antiquark states, so-called mesons, like the pion, where color and anti-color compensate each other. Another possible combination are three (anti-)quarks, which form a so-called baryon, like the proton, as the sum of three different (anti-)colors also result in a $SU(3)_C$ singlet.

---

[1] The subscript C is a reminder of the coupling to color.

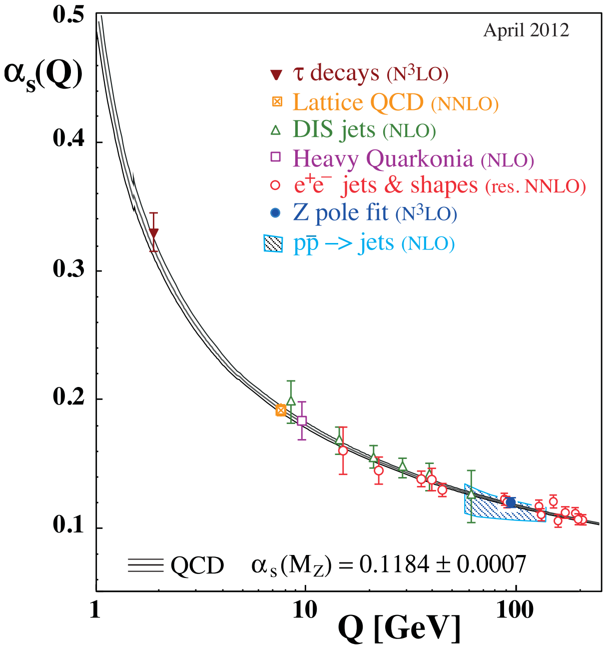

Figure 3.1: Summary of measurements of α_s as a function of the respective energy scale Q. [18]

While hadrons are typically described in terms of these two or three so-called valence quarks, probing the content of a proton in scattering experiments with electrons reveals non-negligible amounts of the other flavors of (anti-)quarks, usually called sea quarks, as well as gluons. Quarks and gluons as constituents of hadrons are called partons.

A relation between the perturbatively computable hard interaction cross section $\hat{\sigma}_{ab\to X}(\hat{s})$ of two partons producing a final state X and the cross section at proton collision level is given by the QCD factorization theorem:

$$\sigma_{pp\to X} = \sum_{a,b} \int_0^1 \int_0^1 \mathrm{d}x_1 \mathrm{d}x_2 \; f_a(x_1, \mu_F)\; f_b(x_2, \mu_F) \times \hat{\sigma}_{ab\to X}(\hat{s}) \tag{3.1}$$

Here $x_{1/2}$ are the longitudinal fractions of the proton momenta that any two interacting partons a and b, which can produce X, carry into the hard interaction. $f_{a/b}(x_{1/2}, \mu_F)$ are the so-called "parton distribution functions" (PDFs), which give the probability density to find each type of parton at the fraction x_i of the proton momentum. The PDFs also depend on a non-physical factorization scale μ_F, which is usually chosen to be equal to the typical momentum transfer $Q^2 = \mu_F^2$ in the hard process and often set to also be equal to the renormalization scale μ_R for the calculation. For the hard interaction only the reduced center-of-mass energy $\sqrt{\hat{s}} = \sqrt{x_1 x_2}\sqrt{s}$ is available.

The PDFs contain the "soft" part of the interaction, which cannot be computed perturbatively. They can be extracted from global fits to data measured in deep inelastic scattering. Such fits are provided by a number of groups. Examples for PDFs provided by the MSTW group [23] can be seen in Fig. 3.2 for two different values of the momentum transfer Q^2.

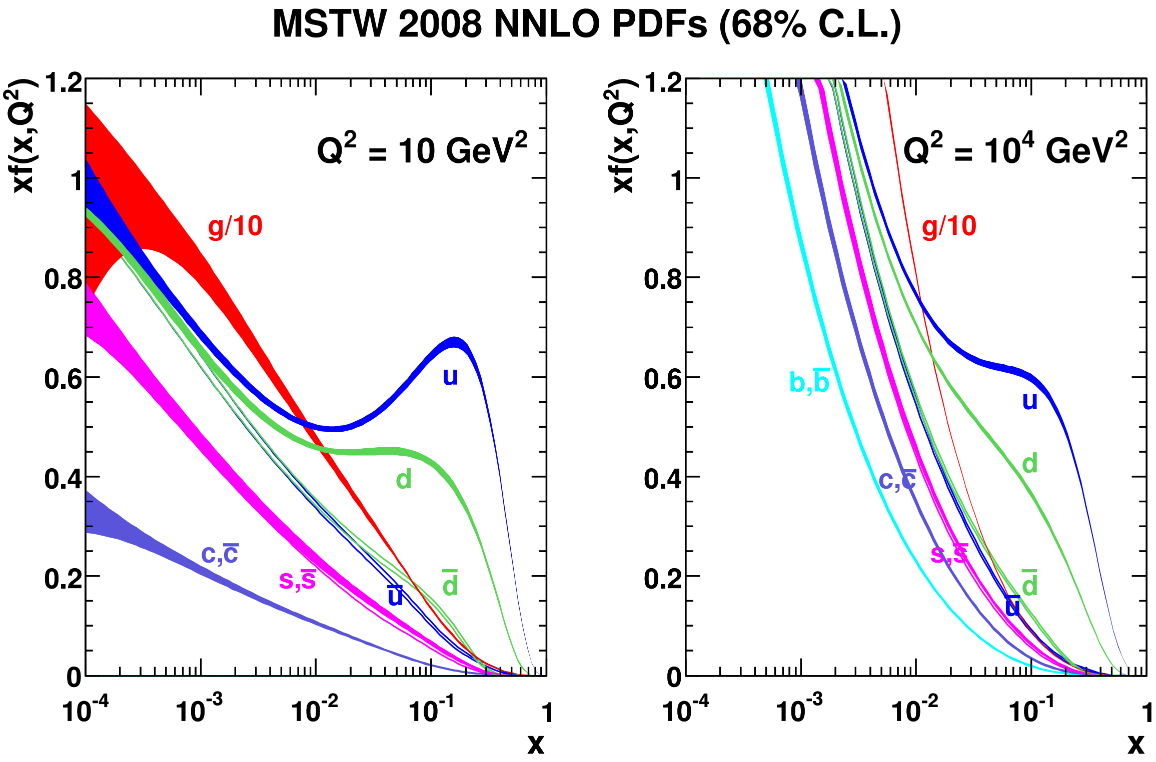

Figure 3.2: MSTW 2008 NNLO PDFs at $Q^2 = 10\,\mathrm{GeV}^2$ and $Q^2 = 10^4\,\mathrm{GeV}^2$ [23]. Note that the gluon curve is scaled down by a factor of 10.

3.1.2 The Electroweak Force

The electroweak (EW) force [24] provides a unified description of the electromagnetic and weak interactions. It corresponds to a symmetry of the Lagrangian under local $SU(2)_L \times U(1)_Y$ transformations[2]. The EW eigenstates of the gauge bosons are the $W_{1,2,3}$ bosons for the $SU(2)_L$ group, and the B^0 boson for the $U(1)_Y$ group. The W bosons only couple to left-handed fermions, which form weak isospin (T) doublets, while the right-handed fermions are singlets, making the SM a chiral theory. The B boson couples to weak hypercharge (Y), carried by all fermions, as well as the Higgs field. The third component of the weak isospin T_3 and Y are related to the electric charge by[3] $Q = T_3 + Y$. The four vector bosons combine to the mass eigenstates

$$W^{\pm} = \frac{1}{\sqrt{2}}\left(W_1 \mp iW_2\right) \quad \text{and} \quad \begin{pmatrix} Z^0 \\ \gamma \end{pmatrix} = \begin{pmatrix} \cos\theta_W & -\sin\theta_W \\ \sin\theta_W & \cos\theta_W \end{pmatrix} \begin{pmatrix} W_3 \\ B^0 \end{pmatrix} \tag{3.2}$$

where θ_W is the weak mixing angle, which can be expressed in terms of the $SU(2)_L$ and $U(1)_Y$ coupling constants g and g' as $\cos\theta_W = g/\sqrt{g^2 + g'^2}$. This mixing also results in a relation

---

[2] The subscripts L and Y are reminders of the couplings to left-handed particles and to the hypercharge, respectively.

[3] An alternative convention, used in Sec. 3.2, is $Q = T_3 + \frac{1}{2}Y$.

between the W and Z masses: $m_W = m_Z \cos\theta_W$.

For quarks the electroweak and mass eigenstates also differ. The resulting mixing can, in the SM, be described by one unitary 3×3 matrix, the “Cabbibo–Kobayashi–Maskawa” or CKM matrix, which experimentally turns out to be mostly diagonal, suppressing the couplings between quarks of different families.

3.1.3 Particle Masses in the Standard Model

The SM fermions, as well as the W and Z bosons experimentally show non-zero masses, as listed in Tab. 3.1. Since explicit mass terms for the fermions ($-m_f \bar{f} f$) as well as the vector bosons ($\frac{1}{2} m_A^2 A_\mu A^\mu$) are forbidden by the gauge symmetries, another mechanism has to explain these masses. In the Standard Model this is done via the introduction of one weakly coupling complex spin 0 doublet field and the Higgs mechanism [25], briefly explained in the following.

To begin with, the Higgs field $\phi = \binom{\phi^+}{\phi^0}$ is added to the Lagrangian, together with a potential $V(\phi^\dagger\phi) = \frac{1}{2}\mu^2\phi^\dagger\phi + \frac{1}{4}\lambda(\phi^\dagger\phi)^2$, where λ has to be positive for the potential to be bounded from below. Initially the μ^2-term seems to be a mass term for the Higgs field. Choosing $\mu^2 < 0$, though, shifts the minimum of the potential away from zero to $v^2 = -\frac{\mu^2}{\lambda}$, where v is the so-called vacuum expectation value (VEV) of the Higgs field. While the theory including this potential is still $SU(2)_L$ symmetric, a non-zero ground state has to be chosen for the Higgs field, because perturbative calculations require an expansion around a minimum. This choice spontaneously breaks the EW symmetry and only the $U(1)_{\mathrm{EM}}$ symmetry of electromagnetism remains.

When re-expanding the Lagrangian in terms of the physical Higgs field, all terms involving powers of the original field split up into one part including the physical field and additional parts containing the VEV instead. Since ϕ originally coupled to the weak vector bosons, the quadratic interaction terms now give rise to masses for the W and Z bosons. The one physical degree of freedom remaining, the real scalar Higgs boson h, also receives a mass from the quartic coupling term in the potential. In addition also the fermions can get their masses via this mechanism, since so-called Yukawa interactions between the fermions and the Higgs field (or its charge-conjugate) of the form $\lambda_f \phi \bar{f} f$ are allowed by the gauge symmetries.

In summary the resulting masses are:

$$m_W = \frac{1}{2} v g \quad , \quad m_Z = \frac{1}{2} v \sqrt{g^2 + g'^2} \quad , \quad m_h = \sqrt{2\lambda v^2} \quad \text{and} \quad m_f = \frac{1}{2}\lambda_f v \tag{3.3}$$

where the value of the Higgs VEV is known, because it is related to the well-measured Fermi constant G_F via the W boson mass: $v \approx 246\,\mathrm{GeV}$.

While the observation of neutrino mixing implies non-zero masses for at least two of the three neutrinos, their masses are so small, compared to the other SM particles, that they usually are neglected. Since right-handed neutrinos would be gauge singlets, which do not interact via any of the three forces, and would only show up in the Yukawa terms, they are (usually) not included in the SM. In some theories that try to explain the neutrino masses, these additional fields are required, though.

Discovering the Higgs boson, as the last unobserved SM particle, has been one of the major goals of the LHC. In July 2012 both the ATLAS and the CMS collaborations published results with "clear evidence for the production of a neutral boson", found in about $10\,\mathrm{fb}^{-1}$ of combined 7 TeV data from 2011 and 8 TeV data from 2012. ATLAS found an excess of 5.9 standard deviations, compatible with production and decay of a SM Higgs boson of $m_h = (126.0 \pm 0.4\,(\mathrm{stat.}) \pm 0.4\,(\mathrm{sys.}))\,\mathrm{GeV}$ [26]. CMS observed 5.8σ for $m_h = (125.3 \pm 0.4\,(\mathrm{stat.}) \pm 0.5\,(\mathrm{sys.}))\,\mathrm{GeV}$ [27]. Because of its decay into two photons, only spin 0 and 2 are possible for this new boson. Further studies of the boson's properties are under way to determine whether it is in fact the SM Higgs boson, as particles or resonances with similar properties are predicted by theories beyond the SM, for instance the lightest Higgs boson in Supersymmetric models.

3.1.4 Open Questions

Most of the predictions of the Standard Model have been confirmed experimentally to high accuracy. Nevertheless there are a number of open questions and problems that hint at or even require additions to the theory at higher energies. Some examples will be given in this section.

The SM has 19 free parameters, which are not predicted by the theory and have to be measured: the nine Yukawa couplings of the Higgs to the fermions, the three couplings for the strong, weak and electromagnetic forces, the three angles and a complex phase of the CKM matrix, the Higgs VEV and self-coupling and a CP-violating phase in the strong sector. (If one includes three massive neutrinos this number is increased by eight: three parameters for the Yukawa couplings and five for the equivalent of the CKM matrix for leptons.) While not strictly necessary, it stands to reason that a more fundamental theory could explain the value of these parameters directly or as effective values at the currently observable energy scales.

The evolution of the inverse running couplings for the three forces in the SM (dashed lines in Fig. 3.4) might be seen as an additional hint in that direction, if one assumes modifications to the theory at higher energies. An example of such a theory, further explained in Sec. 3.2, is shown by the solid lines in the same figure, with a unification scale of roughly 10^{16} GeV.

This unification of the strong and electroweak forces, together with a more fundamental relation between quarks and leptons, is also one of the basic predictions of so-called grand unified theories (GUTs). These usually start from the assumption that some gauge group, like $SO(10)$ or $SU(5)$, containing the SM's $SU(3)_C \times SU(2)_L \times U(1)_Y$ groups, provides the more fundamental description at higher energy scales, with only one force and one gauge coupling. GUTs are able to explain relations between the SM group couplings and the ratio between quark and electron charges as an expression of the respective group structure, but typically have the problem of predicting new gauge bosons coupling to leptons and quarks, which have to be very heavy or only couple very weakly, if at all, to explain the observed proton lifetime.

While negligible at LHC energies, a complete theory will somehow have to include gravity as well, at the latest at the so-called Planck scale M_{Pl} of about 10^{19} GeV, where quantum effects of gravity become important. One of the problems that arise in this context is that the Lagrangian including the force carrier of gravity, the massless spin 2 graviton, is non-renormalizable, which prevents a simple perturbative treatment. Such additional terms might just be an effective approximation of an underlying renormalizable theory (like Fermi's four fermion interaction is of EW theory) for energies small compared to the Planck scale, though, and thus perfectly valid.

Any theory extending the current Standard Model to higher energies, in its effective approximation at energies around the electroweak scale, will at least have to reproduce the SM's successes in explaining experimental observations, though.

Another problem of the Standard Model is the CP-violating phase in the strong sector, already mentioned above, included in a term not forbidden by any of the gauge symmetries. Experimentally a non-zero value of this phase would show up as an electric dipole moment for the neutron. Existing measurements restrict this phase to be extremely small or absent, which is not explained by the SM and could be seen as a case of "fine tuning". This is usually known as the "strong CP problem". A possible solution for this was proposed by Peccei and Quinn [28], introducing a new global $U(1)_{PQ}$ symmetry and a new scalar field. Caused by interactions of the field with the non-trivial QCD vacuum, the VEV it acquires after spontaneously breaking this symmetry then naturally cancels the original phase exactly and a new boson, usually called axion remains, the mass of which depends on the curvature of its potential. So far, though, no conclusive evidence for the existence of axions has been found.

As a final example, the value of the Higgs mass itself is a potential source of concern. Observed properties of weak interactions suggested m_h to be roughly of order 100 GeV, which has now been confirmed by the direct LHC measurements. For consistency the mass is also required to be below the TeV scale, to preserve the unitarity of the WW scattering amplitude at higher energies. The problem of the SM's prediction presents itself when including the modifications of the Higgs mass arising from loop diagrams. For each Dirac fermion f of mass m_f the SM Lagrangian contains a term $\lambda_f h\bar{f}f$, leading to a correction

$$\Delta m_h^2 = -\frac{|\lambda_f|^2}{16\pi^2}\left(2\Lambda^2 + 4m_f^2 \ln\frac{\Lambda}{m_f} + 4m_f^2 + \dots\right) \tag{3.4}$$

Here Λ is a cutoff, regularizing the loop integral, which can be thought of as the scale at which corrections from physics beyond the SM become relevant. This correction will be especially sensitive to the heaviest fermion coupling to the Higgs[4]. Even if using dimensional regularization, where the Λ^2 term is not present, the terms quadratic in the fermion masses would require very fine-tuned cancellations at each order of perturbation theory, which would have to be explained by the new theory, to keep the Higgs boson light. This is often called the "Hierarchy Problem".

3.2 Supersymmetry

Fine-tuned cancellations as required to solve the Hierarchy Problem of the SM might seem unnatural when introduced by hand. They can however occur as a very natural byproduct of symmetries. If a theory extending the SM contained additional complex scalar fields S of mass m_S with the coupling $\lambda_S |S|^2 |h|^2$ to the Higgs field, they would contribute to the Higgs mass

---

[4] This holds even if the coupling is only indirect.

corrections as

$$\Delta m_h^2 = \frac{\lambda_S}{16\pi^2}\left(\Lambda^2 - 2m_S^2 \ln\frac{\Lambda}{m_S} - 2m_S^2 + \dots\right) \tag{3.5}$$

where the opposite sign is due to the loops being bosonic instead of fermionic. Obviously this could exactly cancel the terms in Eq. 3.4 if there were two such scalars per Dirac fermion with $m_f = m_S$ and $\lambda_S = |\lambda_f|^2$. This is precisely what is predicted by "Supersymmetry" (SUSY) [29] which proposes a global symmetry between the bosons and fermions of the underlying theory.

Introductory reviews of SUSY and its phenomenology as an extension of the SM can be found e.g. in [30, 31]. The following sections will introduce the basic ideas relevant in the context of this thesis.

The operator Q generating such a supersymmetric transformation relates fermionic and bosonic fields with

$$Q\,|\text{fermion}\rangle \sim |\text{boson}\rangle, \qquad Q\,|\text{boson}\rangle \sim |\text{fermion}\rangle \tag{3.6}$$

and thus has to be an anti-commuting spinor itself, carrying spin ½. The hermitian conjugate operator $Q^\dagger$ then also is a SUSY generator. These two operators have to satisfy an algebra of (anti-)commutation relations

$$\begin{gathered}\left\{Q_\alpha, Q^\dagger_{\dot\alpha}\right\} = 2\sigma^\mu_{\alpha\dot\alpha}P_\mu \\ \{Q_\alpha, Q_\beta\} = 0, \qquad \left\{Q^\dagger_{\dot\alpha}, Q^\dagger_{\dot\beta}\right\} = 0 \\ [Q_\alpha, P_\mu] = 0\end{gathered} \tag{3.7}$$

where $\alpha, \dot\alpha, \beta, \dot\beta$ are spinor indices, σ^μ are the identity and the three Pauli matrices and P_μ is the four-momentum operator. In addition they also commute with the generators of gauge transformations T^a,

$$[Q_\alpha, T^a] = 0 \tag{3.8}$$

As a result a field and its "superpartner", which together form a so-called "supermultiplet", have the same mass and gauge quantum numbers and only differ by ½ in spin. Each of these supermultiplets has to contain an equal number of bosonic and fermionic degrees of freedom. The two simplest possibilities leading to a renormalizable supersymmetric theory are a Weyl fermion combined with a complex scalar and a vector boson combined with a Weyl fermion. The former combination is called a chiral supermultiplet, the latter a gauge supermultiplet.

To allow the SUSY algebra to also close off-shell, as required by a quantum theory, non-physical auxiliary fields have to be included into the supermultiplets. These fields do not propagate and can be eliminated on-shell using their respective algebraic equation of motion. For the chiral supermultiplets the additional degrees of freedom off-shell require a complex scalar field F, while for the gauge supermultiplets a real scalar D is needed, both carrying the unusual dimension $[\text{mass}]^2$.

The fields of the superpartners are usually marked with a tilde and their names are usually prefixed with the letter "s" for the scalar superpartners, i.e. sfermion, slepton, selectron, squark, etc. and end in "-ino" for the fermionic partners, i.e. gaugino, gluino, higgsino, etc.

The basic SUSY and gauge invariant Lagrangian contains kinetic terms for the scalars, fermions and vector bosons of all chiral and gauge supermultiplets with gauge-covariant derivatives, as well as mass and Yukawa interaction terms for the fermions and scalars, which take the following form:

$$\mathcal{L}_{\text{int}} = -\frac{1}{2}\left(W^{ij}\psi_i\psi_j + \text{h.c.}\right) - W^i W_i^* \tag{3.9}$$

with

$$W^i = \frac{\delta W}{\delta \phi_i} \text{ and } W^{ij} = \frac{\delta^2 W}{\delta \phi_i \, \delta \phi_j} \tag{3.10}$$

Here ψ and ϕ are the fermion and scalar parts of the chiral supermultiplets, respectively and W is the so-called "superpotential", which has to be holomorphic in the fields ϕ. Since they are derived from the same superpotential, the couplings of scalars to scalars and scalars to fermions are related.

The auxiliary fields of the chiral supermultiplets can be expressed in terms of the superpotential as $F_i = -W_i^*$ and $F^{*i} = -W^i$ via their equation of motion $\frac{\delta \mathcal{L}}{\delta F_i} = 0$. Their contribution $W^i W_i^*$ to the scalar potential $V(\phi, \phi^*)$ of the Lagrangian are called "F-terms". Similarly the D auxiliary fields can be replaced for each gauge supermultiplet using $D_a = -g_a \sum_{i,j}(\phi_i^* T_a^{ij} \phi_j)$ (without summing over a), contributing to $V(\phi, \phi^*)$ in form of the so-called "D-terms": $-\frac{1}{2}(g_a \phi^* T_a \phi)^2$, now summing over all ϕ_i and a.

Finally there are also terms in $\mathcal{L}_{SUSY}$ describing fermion–sfermion–gaugino and higgsino–Higgs–gaugino Yukawa couplings of gauge-strength.

3.2.1 The Minimal Supersymmetric Standard Model

Tables 3.2 and 3.3 show the particle content necessary for the minimal supersymmetric extension of the Standard Model, the MSSM. All fermionic fields in the chiral supermultiplets are left-handed. The corresponding scalars carry the index L/R only to denote their SM partners.

Compared to the Standard Model (at least) one additional Higgs doublet is needed in the MSSM. One reason for this is that giving down-type quarks and charged leptons masses using the Higgs field and up-type quarks using the charge conjugate of the Higgs field, as done in the SM, is not possible in the MSSM, since the terms for the conjugate field are not allowed in the superpotential. Another reason shows up on the higgsino side of the supermultiplet. In the SM, to prevent anomalies arising from Feynman graphs containing fermion triangles, the trace over the hypercharges of all fermionic fields has to and does cancel. An additional single higgsino with $Y = -1/2$ would spoil this cancellation. Both of these problems can be solved by introducing a second Higgs supermultiplet with $Y = +1/2$, where the latter (H_u) can then give mass to the up-type quarks, while the former (H_d) can do the same for the down-type quarks and charged leptons.

The most general renormalizable superpotential with this particle content allowed by the SM gauge interactions and SUSY is then given [32] by:

$$W = \epsilon_{ab}\left((\mathbf{Y}_E)_{ij} L_i^a H_d^b \bar{E}_j + (\mathbf{Y}_D)_{ij} Q_i^{ax} H_d^b \bar{D}_{jx} + (\mathbf{Y}_U)_{ij} Q_i^{ax} H_u^b \bar{U}_{jx}\right) - \epsilon_{ab}\mu H_d^a H_u^b \tag{3.11a}$$

$$+ \epsilon_{ab}\left(\frac{1}{2}\lambda_{ijk} L_i^a L_j^b \bar{E}_k + \lambda'_{ijk} L_i^a Q_j^{bx} \bar{D}_{kx}\right) + \frac{1}{2}\epsilon_{xyz}\lambda''_{ijk} \bar{U}_i^x \bar{D}_j^y \bar{D}_k^z - \epsilon_{ab}\kappa^i L_i^a H_u^b \tag{3.11b}$$

Names		spin 0	spin ½	$SU(3)_C$, $SU(2)_L$, $U(1)_Y$
squarks, quarks	Q	$(\tilde{u}_L\ \tilde{d}_L)$	$(u_L\ d_L)$	$(\mathbf{3}, \mathbf{2},\ {}^1\!/_6)$
(×3 families)	$\bar{U}$	$\tilde{u}_R^*$	$u_R^\dagger$	$(\bar{\mathbf{3}}, \mathbf{1}, -{}^2\!/_3)$
	$\bar{D}$	$\tilde{d}_R^*$	$d_R^\dagger$	$(\bar{\mathbf{3}}, \mathbf{1},\ {}^1\!/_3)$
sleptons, leptons	L	$(\tilde{\nu}\ \tilde{e}_L)$	$(\nu\ e_L)$	$(\mathbf{1}, \mathbf{2}, -{}^1\!/_2)$
(×3 families)	$\bar{E}$	$\tilde{e}_R^*$	$e_R^\dagger$	$(\mathbf{1}, \mathbf{1},\ 1\ )$
Higgs, higgsinos	H_u	$(H_u^+\ H_u^0)$	$(\tilde{H}_u^+\ \tilde{H}_u^0)$	$(\mathbf{1}, \mathbf{2},\ {}^1\!/_2)$
	H_d	$(H_d^0\ H_d^-)$	$(\tilde{H}_d^0\ \tilde{H}_d^-)$	$(\mathbf{1}, \mathbf{2}, -{}^1\!/_2)$

Table 3.2: Chiral supermultiplets in the Minimal Supersymmetric Standard Model. The spin 0 fields are complex scalars, the spin ½ fields are left-handed two component Weyl spinors. Adapted from [31].

Names	spin ½	spin 1	$SU(3)_C$, $SU(2)_L$, $U(1)_Y$
gluino, gluon	$\tilde{g}$	g	$(\mathbf{8}, \mathbf{1}, 0)$
winos, W bosons	$\tilde{W}^\pm\ \tilde{W}^0$	$W^\pm\ W^0$	$(\mathbf{1}, \mathbf{3}, 0)$
bino, B boson	$\tilde{B}^0$	B^0	$(\mathbf{1}, \mathbf{1}, 0)$

Table 3.3: Gauge supermultiplets in the Minimal Supersymmetric Standard Model. Adapted from [31]

where i, j, k are generation indices, x, y, z are $SU(3)_C$ and a, b $SU(2)_L$ gauge indices and all involved fields are the scalar parts of the supermultiplets[5]. The $\mathbf{Y}_{E,D,U}$ are 3×3 matrices of Yukawa couplings. The λ_{ijk}, λ'_{ijk} and λ''_{ijk} are Yukawa couplings as well, with λ anti-symmetric in the first two indices and λ'' in the last two. The parameters μ and κ_i have mass dimension one.

The first, second and the last term in Eq. 3.11b violate the conservation of lepton number L, while the third violates the conservation of baryon number B. Allowing combinations of B and L violating terms leads to rapid proton decay, as shown in the example in Fig. 3.3, and thus strongly contradicts observation.

To avoid this, an additional ad-hoc symmetry called R-parity is usually introduced with the multiplicative quantum number

$$R_p = (-1)^{2S+3B+L} \tag{3.12}$$

where S is the particle's spin, being considered a conserved quantity. This explicitly forbids all terms on the second line of Eq. 3.11. For collider experiments this would have a number of consequences. Since all SM particles have $R_p = +1$ while all SUSY partners have $R_p = -1$, SUSY particles at colliders would be produced in even numbers and then decay via the emission of SM particles down to the lightest supersymmetric particle, the so-called "LSP", which would have to be stable. If this LSP additionally was electrically neutral, it would be an interesting candidate for non-baryonic dark matter, an ingredient necessary for most cosmological models. This is often even turned into a requirement for the LSP, leading to the expectation of a missing energy signature for SUSY events at colliders.

---

[5] To reduce clutter the tilde usually signifying the superpartners will be omitted for terms of the superpotential, which only contains scalar fields.

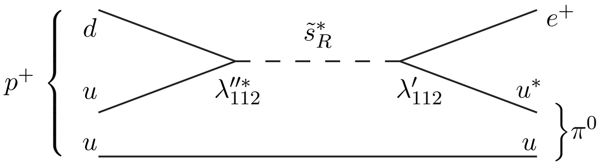

Figure 3.3: Example of a possible proton decay $p \to e^+\pi^0$ via a down-type squark and B and L violating couplings. [31]

To simplify the discussion of the main features of the MSSM, R_p conservation will be assumed for the following sections, before coming back to the consequences of R-parity violation ($\not{R}_p$) in Sec. 3.2.7.

3.2.2 Soft Supersymmetry Breaking

If SUSY was an exact symmetry, all members of a supermultiplet would have the same mass. Since the superpartners of the SM particles have not been found so far by experiments, supersymmetry, if realized in nature, has to be broken.

The SUSY breaking scale cannot be too large, though, and the relation between the dimensionless couplings ($\lambda_S = |\lambda_f|^2$) has to hold, if this theory is still to provide the solution to the hierarchy problem of the SM. The additional SUSY breaking part of the Lagrangian can then only contain mass terms and couplings with positive mass dimension. It can be shown that such a "soft" breaking is free of quadratic divergencies for the masses of the scalar fields to all orders. If the model has to remain valid and perturbative up to the Planck scale, the scale of this soft breaking (m_{soft}) has to be of the order of roughly 1 TeV.

Spontaneously breaking global Supersymmetry at tree-level by allowing non-zero vacuum expectation values in the F-term and/or D-term parts of the scalar potential usually leads to phenomenologically problematic results. Regardless of whether SUSY is broken at tree-level or only indirectly or radiatively, it requires an extension of the MSSM with additional supermultiplets and interactions at high energies.

As there is no obvious choice of breaking mechanism, the MSSM makes no further assumptions on the origin of SUSY breaking and instead adopts a parametrizing approach, by including all terms allowed by the symmetries and the requirements of soft breaking mentioned above. The soft-breaking part of the Lagrangian, $\mathcal{L}_{\text{soft}}$, then contains [31] gaugino mass terms, trilinear scalar interactions, scalar mass terms and bilinear scalar terms:[6]

$$\begin{aligned}\mathcal{L}_{\text{soft}} = &-\frac{1}{2}\left(M_3\tilde{g}\tilde{g} + M_2\tilde{W}\tilde{W} + M_1\tilde{B}\tilde{B} + h.c.\right)\\ &-\left(\tilde{\bar{\bar{U}}}\mathbf{a_U}\tilde{Q}H_u - \tilde{\bar{\bar{D}}}\mathbf{a_D}\tilde{Q}H_d - \tilde{\bar{\bar{E}}}\mathbf{a_E}\tilde{L}H_d + h.c.\right)\\ &-\left(\tilde{Q}^\dagger\mathbf{m^2_{\tilde{Q}}}\tilde{Q} + \tilde{L}^\dagger\mathbf{m^2_{\tilde{L}}}\tilde{L} + \tilde{\bar{\bar{U}}}\mathbf{m^2_{\tilde{U}}}\tilde{\bar{\bar{U}}}^\dagger + \tilde{\bar{\bar{D}}}\mathbf{m^2_{\tilde{D}}}\tilde{\bar{\bar{D}}}^\dagger + \tilde{\bar{\bar{E}}}\mathbf{m^2_{\tilde{E}}}\tilde{\bar{\bar{E}}}^\dagger\right)\\ &-m^2_{H_u}H_u^*H_u - m^2_{H_d}H_d^*H_d - (bH_uH_d + h.c.)\end{aligned} \tag{3.13}$$

---

[6] If the MSSM contained gauge singlets, linear terms would be allowed, too.

where generation and gauge indices have now been suppressed. $M_{1/2/3}$ are gaugino mass terms, $\mathbf{m^2_{\tilde{Q}}}$, $\mathbf{m^2_{\tilde{L}}}$, $\mathbf{m^2_{\tilde{U}}}$, $\mathbf{m^2_{\tilde{D}}}$ and $\mathbf{m^2_{\tilde{E}}}$ are hermitian 3×3 mass-squared matrices for the squarks and sleptons, $\mathbf{a_U}$, $\mathbf{a_D}$ and $\mathbf{a_E}$ complex 3×3 dimension mass matrices, analogue to the trilinear Yukawa couplings in the superpotential, $m^2_{H_{u/d}}$ are explicit contributions to the squared masses of the two Higgs doublets and b is a dimension mass-squared bilinear coupling between the Higgs doublets. This results in over 100 unknown real parameters introduced by the soft SUSY breaking, which is far from predictive.

As the general form of terms in $\mathcal{L}_{\text{soft}}$ implies SUSY contributions to flavor changing neutral currents as well as CP violation, the terms are severely constrained by experiment. A common assumption is that of so-called "universal" SUSY breaking, which can be defined as

$$\mathbf{m^2_{\tilde{X}}} = m^2_{\tilde{X}}\,\mathbf{1} \quad \text{for } X \in \{Q, \bar{U}, \bar{D}, L, \bar{E}\} \tag{3.14a}$$

$$\mathbf{a_X} = A_{X0}\mathbf{Y_X} \quad \text{for } X \in \{U, D, E\} \tag{3.14b}$$

$$\Im(M_1) = \Im(M_2) = \Im(M_3) = \Im(A_U) = \Im(A_D) = \Im(A_E) = 0 \tag{3.14c}$$

where $\mathbf{1}$ is the 3×3 unit matrix in family space and $\mathbf{Y_X}$ are the corresponding Yukawa matrices in the superpotential. This results in flavor-blind mass terms and trilinear scalar couplings which are large only for the third family fields, i.e. $\tilde{t}$, $\tilde{b}$ and $\tilde{\tau}$, while the vanishing imaginary parts of the parameters lead to a suppression of SUSY contributions to CP violation. Under this assumption the number of free parameters of the MSSM would be reduced to three real gaugino masses, five real squark and slepton mass parameters, three real scalar-cubed couplings and four Higgs mass parameters in addition to the SM parameters.

3.2.3 Electroweak Symmetry Breaking and Mass Eigenstates in the MSSM

As an extension of the SM, the MSSM should of course be able to reproduce the experimentally observed features of the broken electroweak symmetry. In contrast to the SM, the quartic Higgs coupling is not a free parameter in the MSSM, but given by the electroweak gauge couplings. In addition the two soft-breaking Higgs masses $m^2_{H_{u/d}}$, which also contribute to the scalar potential via $\mathcal{L}_{\text{soft}}$, have to differ at the weak scale to provide a minimum which breaks the EW symmetry. Since the SUSY conserving contributions to the two Higgs doublet masses are identical, this provides another reason for Supersymmetry to be broken in the MSSM.

Via the Higgs mechanism three of the now eight degrees of freedom provided by the two Higgs doublets give rise to the W and Z boson masses, as in the SM. In addition to that, the remaining five degrees of freedom result in three neutral real scalars: a lighter and a heavier CP-even Higgs boson, h^0 and H^0 respectively, a CP-odd Higgs, A^0, as well as two charged scalars, H^+ and H^-. The VEVs of the two Higgs doublets v_u and v_d are related to the SM Higgs VEV v via

$$v_u^2 + v_d^2 = v^2 \tag{3.15}$$

and one usually also defines the ratio

$$\tan\beta = \frac{v_u}{v_d} \tag{3.16}$$

After the electroweak symmetry is broken, all MSSM fields with the same $SU(3)_C \times U(1)_{\mathrm{EM}}$ quantum numbers can mix. The W^0 and the B^0 again form the Z^0 and the massless photon. For the leptons and quarks the masses and CKM mixing angles are mainly determined by the Yukawa coupling matrices in the superpotential.

The charged higgsinos mix with the charged winos into two “charginos”, $\tilde{\chi}_1^\pm$ and $\tilde{\chi}_2^\pm$, while the neutral higgsinos, the neutral wino and the bino combine into four Majorana fermions, the “neutralinos”, $\tilde{\chi}_1^0$, $\tilde{\chi}_2^0$, $\tilde{\chi}_3^0$ and $\tilde{\chi}_4^0$. By convention these are numbered according to their mass, starting with 1 for the lightest.

If the mixing between different sfermion generations can be neglected, the mass-squared matrices decompose into 2×2 blocks for each pair of $SU(2)_L$ doublet and corresponding singlet state. Since the mixing is proportional to the mass of the SM partner, this is mostly relevant for the third generation squarks and sleptons. The mass eigenstates e.g. of the $\tilde{\tau}_{\mathrm{L}}$ and $\tilde{\tau}_{\mathrm{R}}$ are called $\tilde{\tau}_1$ and $\tilde{\tau}_2$, where the first is again the lighter one, by convention.

3.2.4 Renormalization Effects in the MSSM

The parameters in $\mathcal{L}_{\mathrm{soft}}$ as well as in the superpotential are subject to renormalization. This includes the universal breaking conditions mentioned in Sec. 3.2.2 or any alternatives, which have to be understood as boundary conditions at some input scale and will in general only hold approximately at the EW scale.

The input scale is often chosen to be the scale of the apparent gauge coupling unification in the MSSM when assuming a supersymmetric GUT theory at higher energies or as the value at which g_1 and g_2 meet, as g_3 tends to be slightly bigger there, which can be due to threshold corrections of new physics becoming important.

The one-loop RG equations for the three gauge couplings are [31]

$$\frac{d}{dt} g_a = \frac{1}{16\pi^2} b_a g_a^3 \qquad \text{with} \quad (b_1, b_2, b_3) = \begin{cases} (41/10, -19/6, -7) & \text{SM} \\ (33/5, 1, -3) & \text{MSSM} \end{cases} \tag{3.17}$$

where t is the log of the ratio between the input and the renormalization scale and $g_1 = \sqrt{5/3}\, g'$, to have the canonical normalization for a $SU(5)$ or $SO(10)$ GUT. Apart from the modified values of the coefficients note the different sign for b_2 and recall that the contributions of the new SUSY fields only affect the running above their mass scale.

The result of plotting the RG evolution for the inverse couplings, $\alpha_a = \frac{g_a^2}{4\pi}$, versus energy scale for a fixed input scale, including two-loop effects is shown in Fig. 3.4.

An example of the effects of RG evolution on the scalar and gaugino mass parameters can be seen in Fig. 3.5. Here a specific model called mSUGRA, which is even more predictive than the universal SUSY breaking assumptions of Sec. 3.2.2 and which is further explained in Sec. 3.2.5, is assumed to provide the boundary conditions at high energies[7]. For the squarks and sleptons the solid lines mark the evolution of the mass parameters of the first two generations, while the dashed lines stand for the third family. While the parameters for both Higgs fields start out

---

[7] The model parameters used are $m_0 = 200\,\mathrm{GeV}$, $m_{1/2} = -A_0 = 600\,\mathrm{GeV}$, $\tan\beta = 10$, $\mathrm{sgn}(\mu) = +1$.

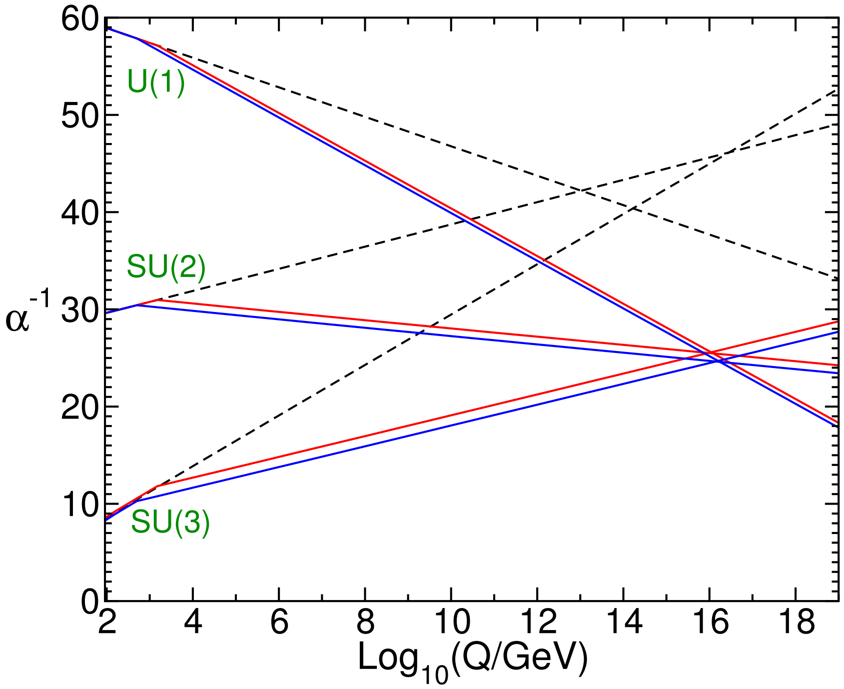

Figure 3.4: Two-loop renormalization group evolution of the inverse gauge couplings $\alpha_a^{-1}(Q)$ in the Standard Model (dashed lines) and the MSSM (solid lines). In the MSSM case, the sparticle masses are treated as a common threshold varied between 500 GeV and 1.5 TeV, and $\alpha_3(m_Z)$ is varied between 0.117 and 0.121. [31]

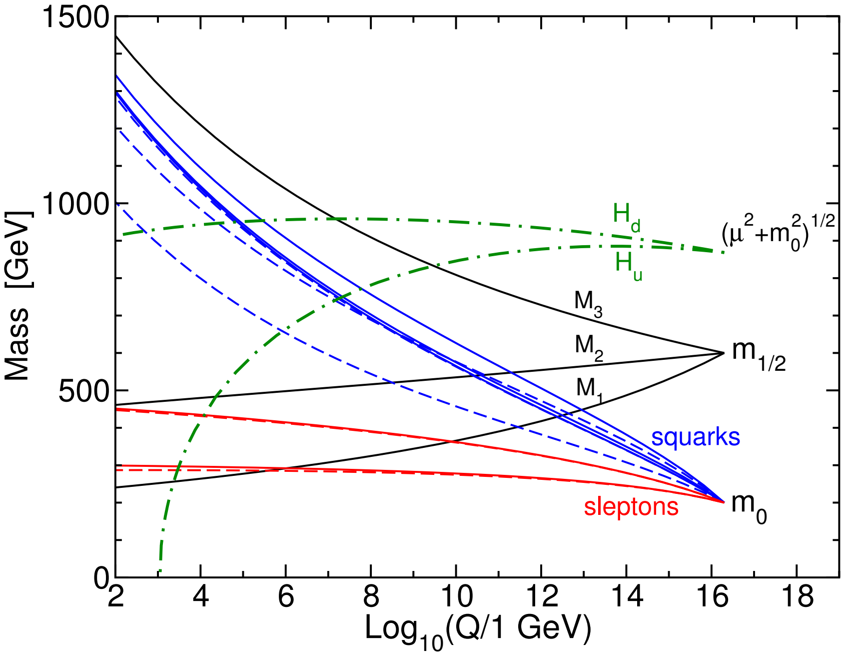

Figure 3.5: Example of RG evolution of scalar and gaugino mass parameters in the MSSM with mSUGRA boundary conditions imposed at $Q_0 = 2 \times 10^{16}$ GeV. The parameter $\mu^2 + m_{H_u}^2$ runs negative, provoking electroweak symmetry breaking. [31]

at the same value, the one for H_u runs negative, because of the contribution of the large top Yukawa coupling, triggering a radiative electroweak symmetry breaking.

3.2.5 Minimal Supergravity/The Constrained MSSM

To get around the phenomenological problems arising when spontaneously breaking Supersymmetry, one can assume that the breaking happens in a "hidden" sector of new supermultiplets, which have no or only very small direct couplings to the chiral supermultiplets of the MSSM (the "visible" sector). This breaking then has to be mediated to the visible sector by some shared interactions, effectively resulting in some of the soft-breaking terms in Eq. 3.13.

One interesting candidate for such an interaction is gravity. Since including gravity implies invariance under local coordinate changes and the SUSY algebra (Eq. 3.2) includes the generator of space-time translations P_μ, SUSY has to be promoted to a local symmetry as well. Such a theory is called "supergravity" (SUGRA).

The full SUGRA Lagrangian can be expanded in powers of E/M_{Pl}, resulting in non-renormalizable contributions to the effective MSSM Lagrangian, which describe the interactions between some hidden sector field X and the usual chiral supermultiplets of the visible sector of the MSSM. When the generalized auxiliary field F of this theory acquires a VEV $\langle F\rangle$ and the Lagrangian is re-expanded, it will contain soft breaking terms as in Eq. 3.13. The parameters of these terms are proportional to powers of $\frac{\langle F\rangle}{M_{\mathrm{Pl}}}$ and to the original couplings of X to the visible sector fields.

Requiring X to have only one common coupling to all MSSM gauginos and common, real couplings to all MSSM scalars and aligning the other couplings with their superpotential counterparts[8] leads to a "minimal" model in which the soft terms of the MSSM are determined by just four parameters: a common gaugino mass $m_{1/2}$ with

$$M_1 = M_2 = M_3 = m_{1/2} \tag{3.18a}$$

a common scalar mass m_0 with

$$\mathbf{m}^2_{\mathbf{Q}} = \mathbf{m}^2_{\mathbf{L}} = \mathbf{m}^2_{\mathbf{U}} = \mathbf{m}^2_{\mathbf{D}} = \mathbf{m}^2_{\mathbf{E}} = m_0^2\mathbf{1}, \qquad m^2_{H_u} = m^2_{H_d} = m_0^2 \tag{3.18b}$$

a common trilinear coupling A_0 with

$$\mathbf{a}_{\mathbf{U}} = A_0\mathbf{Y}_U, \quad \mathbf{a}_{\mathbf{D}} = A_0\mathbf{Y}_D, \quad \mathbf{a}_{\mathbf{E}} = A_0\mathbf{Y}_E \tag{3.18c}$$

and B_0, relating the μ term of the superpotential and the b term in $\mathcal{L}_{\mathrm{soft}}$ as

$$b = B_0\mu \tag{3.18d}$$

If $m_{1/2}$, A_0 and B_0 have the same complex phase this describes a stronger version of the universality conditions given in Eq. 3.14.

---

[8] This can be achieved by imposing an additional $U(N)$ symmetry on the so-called "Kähler metric" of the SUGRA theory, where N is the number of supermultiplets in the visible sector ($N = 17$ for the MSSM).

By requiring the radiative electroweak symmetry breaking to reproduce the measured Z mass, one can replace b or B_0 and the unknown parameter μ of the superpotential with the ratio of the two Higgs VEVs $\tan\beta$ and the sign of μ. This model, consisting of only four parameters and a sign, is called minimal Supergravity (mSUGRA) or the constrained MSSM (CMSSM)[9].

As mentioned in Sec. 3.2.4, these conditions have to be seen as boundary conditions. While the corresponding scale should in principle be M_{Pl}, in practice often the unification scale (of order 2×10^{16} GeV) is chosen instead, neglecting the evolution between these scales.

As a final remark, a supersymmetric QFT including gravity also has to include the massless spin 2 graviton and its spin 3⁄2 superpartner, the gravitino. When SUSY is spontaneously broken a massless neutral Weyl fermion called goldstino emerges and is absorbed by the gravitino, which thus acquires a mass. In analogy to the way the vector bosons acquire mass in the SM, this is called the “super Higgs mechanism”. While the gravitino mass typically is comparable to the other sparticle masses in mSUGRA, its interactions are only of gravitational strength and usually can be neglected for collider phenomenology.

3.2.6 Sparticle Production at the LHC

Supersymmetric particles, just like their SM partners, are produced in parton interactions, i.e. in those of quarks, anti-quarks and gluons contained in the protons brought to collision at the LHC.

Possible production processes of squarks and gluinos via strong couplings (so-called “strong production”) of the type $pp \to \tilde{g}\tilde{g}$, $pp \to \tilde{q}\tilde{q}$ and $pp \to \tilde{q}\tilde{g}$ are shown in more detail in Figs. 3.6 and 3.7. These are the dominant production processes at the LHC’s center-of-mass energies, as long as squarks and gluinos are not too heavy to be produced directly.

Squarks or gluinos can also be produced together with charginos or neutralinos in mixed electroweak and strong processes (so-called “associated production”) of the type $pp \to \tilde{q}\tilde{\chi}$ or $pp \to \tilde{g}\tilde{\chi}$ as schematically shown in Fig. 3.8. For many models the cross sections for this type of production process are predicted to be very small, though.

Sparticles can also be produced in electroweak processes of the type $pp \to \tilde{\chi}\tilde{\chi}$, $pp \to \tilde{\ell}\tilde{\ell}$, $pp \to \tilde{\nu}\tilde{\nu}$ or $pp \to \tilde{\ell}\tilde{\nu}$, shown in Fig. 3.9.

---

[9] CMSSM is also used sometimes to indicate a model with the parameters given here, but without implying a specific SUSY-breaking mechanism. Conversely, mSUGRA is also used to name models including further relations e.g. between A_0 and B_0.

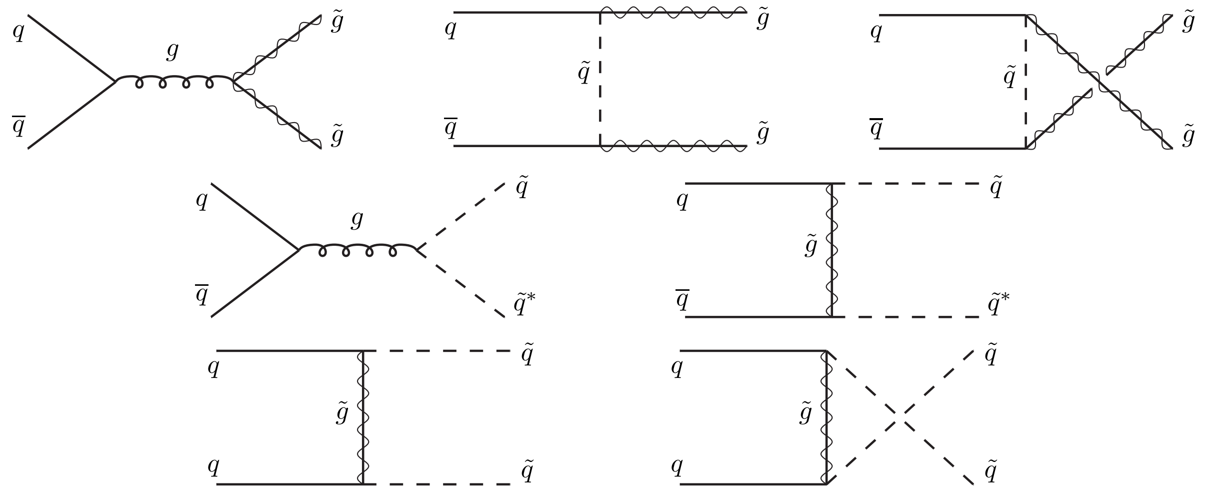

Figure 3.6: Feynman diagrams for gluino and squark production at hadron colliders from strong quark–antiquark annihilation and quark–quark scattering. Adapted from [31].

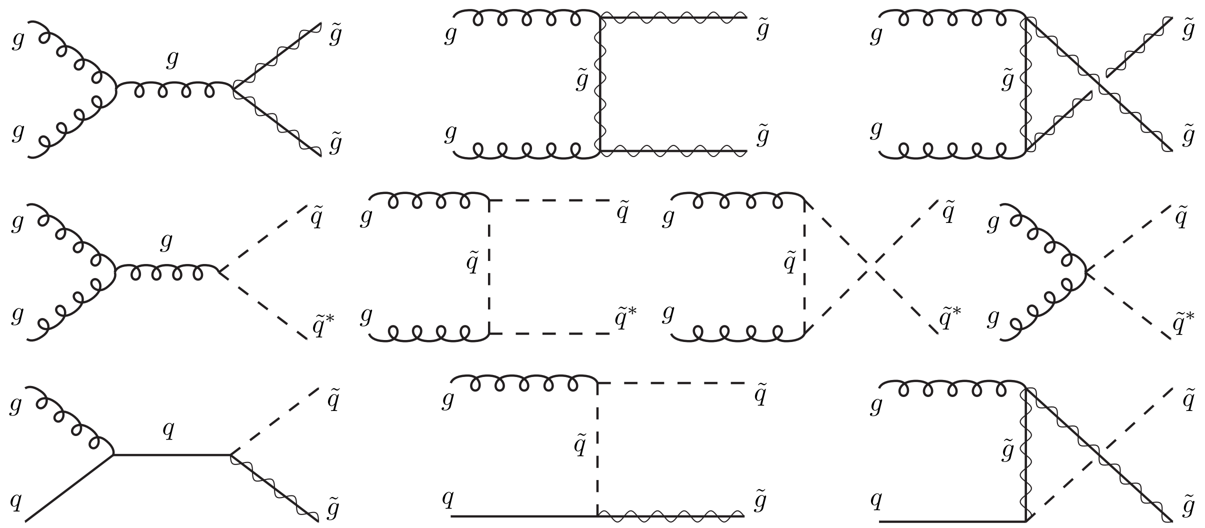

Figure 3.7: Feynman diagrams for gluino and squark production at hadron colliders from gluon–gluon and gluon–quark fusion. Adapted from [31].

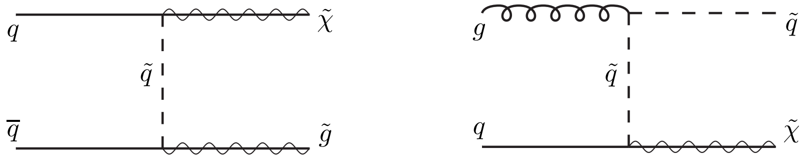

Figure 3.8: Example Feynman diagrams for associated (mixed electroweak and strong) production of squarks/gluinos and neutralinos/charginos at hadron colliders from quark–antiquark annihilation and gluon–quark fusion.

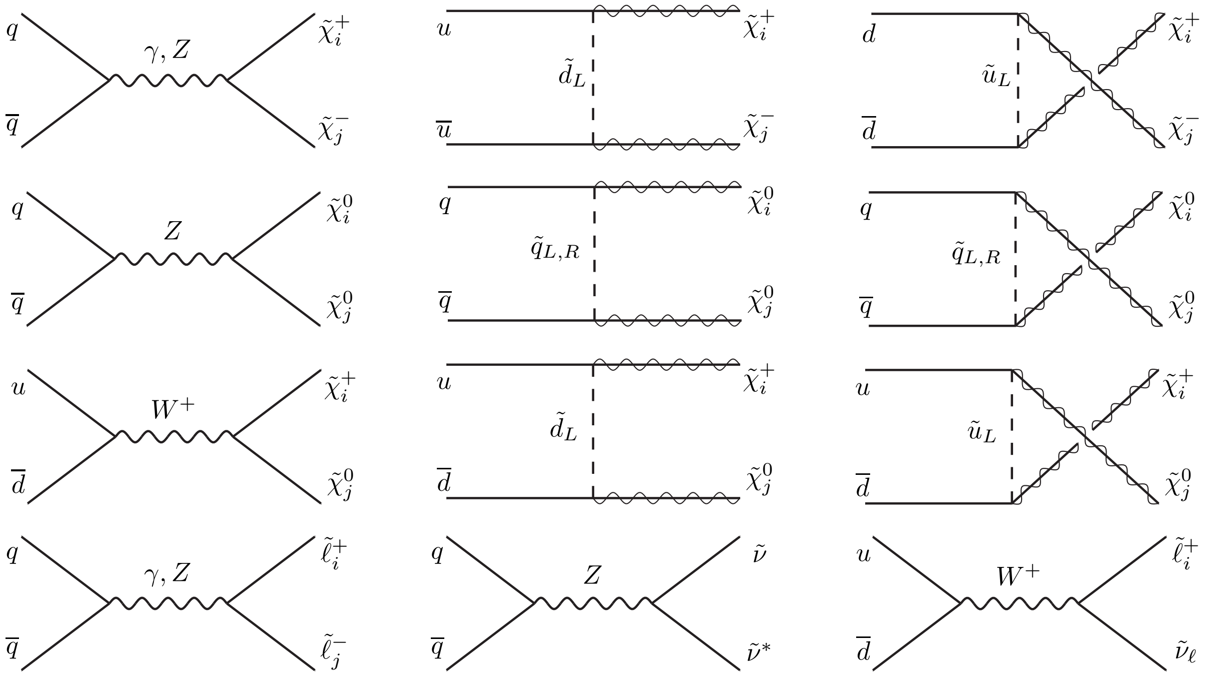

Figure 3.9: Feynman diagrams for electroweak production of sparticles at hadron colliders from quark–antiquark annihilation. The charginos and neutralinos in the t-channel diagrams only couple because of their gaugino content, for massless initial-state quarks, and so are drawn as wavy lines superimposed on solid. Adapted from [31].

3.2.7 Consequences of R-Parity Violation

While excluding all R-parity violating ($\not{R}_p$) terms in Eq. 3.11b from the superpotential can prevent the proton decay, the introduction of R-parity is somewhat ad hoc and more restrictive than necessary, as preventing either baryon or lepton number violating couplings is in principle enough to achieve the same.

All anomaly-free discrete gauge symmetries for the MSSM that are suitable for this purpose without introducing new light particles were studied systematically in [32] for Z_2 and Z_3 symmetries and in [33] for the general Z_N case. The number of viable symmetries was found to be severely restricted by the following phenomenologically motivated requirements:

- allowing the presence of the μ term in the low-energy effective superpotential,
- baryon number conservation up to non-renormalizable dimension-five operators, which are allowed if the MSSM is only an effective theory and
- allowing the presence of a LH_uLH_u term, which can incorporate neutrino masses into the model without introducing additional fields.

In addition the discrete symmetry was required to be the remnant of a spontaneously broken abelian gauge symmetry, as *global* discrete symmetries are typically violated by quantum gravity effects, as found e.g. in supergravity models. The authors found that only two symmetries fulfill all of these requirements: “proton hexality”, which can be seen as a generalized form of the usual R-parity[10], and “baryon triality”, defined as

$$B_3 = \exp(2\pi i[B - 2Y]/3) \tag{3.19}$$

which forbids the baryon number violating, but allows the lepton number violating terms in the superpotential (including dimension-five operators) and in fact absolutely forbids proton decay as it only allows baryon number to change in multiples of three units.

In the general $\not{R}_p$ case, B- or L-violating couplings are allowed, but their magnitude is often severely restricted by experiment. Upper bounds on single $\not{R}_p$ couplings, derived from particle decay ratios and atomic parity violation can be found in [34] and bounds for the lepton number violating couplings in a B_3 mSUGRA model, resulting from the cosmological bound on the sum of neutrino masses, are given in [35]. Bounds on products of couplings can be found in [36], for example.

A full description of an R-parity violating mSUGRA model is given in [32]. A closer look at the mass spectrum in this framework, concentrating on the B_3 case, as well as a proposal for four benchmark points, specifically designed to not have the neutralino LSP typical for the R_p case, is given in [37].

The remainder of this section contains a short summary of some of the changes of the $\not{R}_p$ models given in the two references above compared to the phenomenology of the R_p conserving case discussed so far. Some more details on one of the benchmark point chosen for further experimental study will follow in Sec. 3.2.8.

---

[10] In fact proton hexality is isomorphic to the direct product of B_3 and matter parity, which is equivalent to R-parity, when looking at the resulting superpotential.

Looking at Tab. 3.2 one can see that, in case L is not conserved, the lepton doublet and the down-type Higgs supermultiplets will in general form mixed states, since they have the same gauge quantum numbers. One effect of this can be seen in the superpotential, where the L-violating terms in Eq. 3.11b follow from the R_p conserving terms when replacing $H_d \to \tilde{L}_i$. The actual mixing of the four supermultiplets depends on the parameters μ and κ_i.

The $\not{R}_p$ terms in the superpotential are accompanied by corresponding additions to the soft-breaking part of the Lagrangian which was given in Eq. 3.13 [31, 32]:

$$\begin{aligned}\mathcal{L}^{\not{R}_p}_{\text{soft}} = &- h_{ijk}\tilde{L}_i\tilde{L}_j\tilde{\bar{E}}_k - h'_{ijk}\tilde{L}_i\tilde{Q}_j\tilde{\bar{D}}_k - h''_{ijk}\tilde{\bar{U}}_i\tilde{\bar{D}}_j\tilde{\bar{D}}_k - \tilde{D}_i\tilde{L}_iH_u \\ &- H_d^*\mathbf{m}^2_{\mathbf{H_d\tilde{L}_i}}\tilde{L}_i - h.c.\end{aligned} \tag{3.20}$$

where h, h' and h'' are couplings of mass dimension one and the $\tilde{D}_i$[11] couplings of mass dimension two. The last term results from the soft-breaking squared mass term for $\tilde{L}_i$, when $\tilde{L}_i$ and H_d mix. These new terms contribute to the scalar potential, too, of course.

The three sneutrinos can now also acquire vacuum expectation values v_i, modifying the relation of the two MSSM Higgs VEVs to the SM Higgs VEV in Eq. 3.15 into

$$v_u^2 + v_d^2 + \sum_i v_i^2 = v^2 \tag{3.21}$$

For comparison with the R_p conserving case, in particular when $v_i \ll v$, it is usually more convenient to keep the definition of $\tan\beta$ as in Eq. 3.16.

After breaking the EW symmetry the mixing of fields as described in Sec. 3.2.3 is modified in the following ways:

- the electrically neutral Higgs bosons can now mix with the (anti-)sneutrinos, influenced by the coefficients of the bilinear soft-breaking terms and the v_i,
- the charged Higgs bosons can mix with the charged sleptons, the off-diagonals containing λ_{ijk} and h_{ijk} terms and v_i,
- the down- and up-type squark mass matrices are modified by terms proportional to products of the sneutrino VEVs and λ'_{ijk} as well as h'_{ijk},
- the down quark mass matrix receives a contribution from $\lambda'_{ijk}v_i$ terms,
- the neutrinos can mix with neutralinos, depending on ratios of Higgs and sneutrino VEVs
- and the charged leptons can mix with the charginos with contributions depending on $\lambda_{ijk}v_i$.

The full mass matrices are given in [32].

The mixing of neutrinos and neutralinos leads to another important feature of the B_3 MSSM. Apart from four massive neutralinos, it can also predict one massive neutrino at tree level and two additional massive neutrinos once loop corrections are taken into account. In contrast to other neutrino mass models, no additional fields (e.g. right-handed neutrinos) have to be

---

[11] Note that the couplings $\tilde{D}_i$ do not carry a bar, in contrast to the down-type $SU(2)_L$ singlet supermultiplets $\bar{D}_i$ and their scalar parts $\tilde{\bar{D}}_i$.

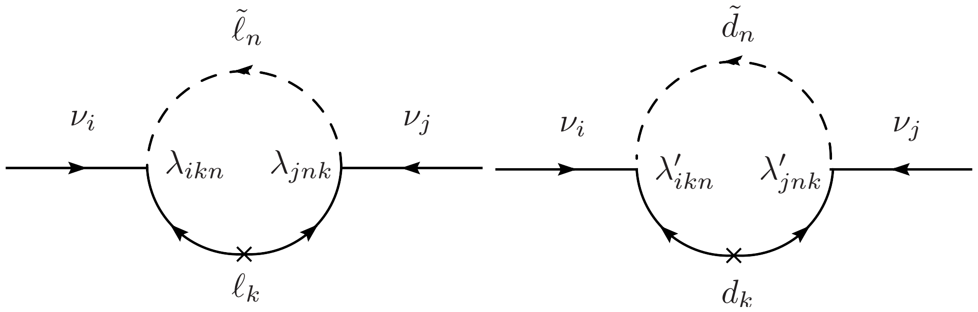

Figure 3.10: Loop contribution to the neutrino mass matrix via non-vanishing λ (left) or λ' (right) couplings. [35]

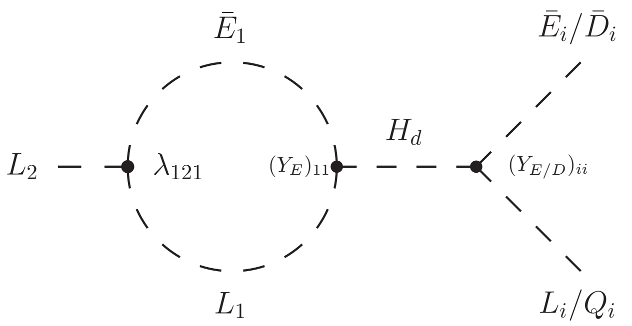

Figure 3.11: Dynamical generation of the $\not{R}_p$ couplings λ_{i2i} and λ'_{2ii} from non-zero λ_{121} at the GUT scale.

introduced into the theory for this. Feynman graphs for such loop contributions are shown in Fig. 3.10.

As mentioned above this can be used to derive upper bounds on the lepton number violating couplings in B_3 mSUGRA models at the GUT scale, by expressing the generated neutrino masses as functions of the $\not{R}_p$ couplings.

While bounds on combinations of $\not{R}_p$ couplings at the GUT scale indicate that starting with just one non-zero coupling is a very good approximation, additional couplings can dynamically be generated in the RG evolution down to the EW scale via loops like the one shown in Fig. 3.11. The example shows λ_{121} generating all other λ_{i2i} and λ'_{2ii} couplings. Because of the small size of the Yukawa factors $\mathbf{Y}_{E/D}$ the most relevant contributions are those for the third family ($i = 3$). Note that the generated couplings scale with size of the original $\not{R}_p$ coupling.

The violation of R-parity can also have an influence on the expected SUSY signatures at colliders, compared to the R_p conserving case. To begin with, SUSY particles do not have to be produced in pairs any more, allowing single slepton/sneutrino or squark production at hadron colliders like the LHC in case of a non-zero λ' or λ'' coupling, as schematically shown in Fig. 3.12a and b, respectively, or single slepton production via a non-zero λ coupling at a lepton collider, as shown in Fig. 3.12c. Whether or not this is the primary production mechanism of course depends on the relative strengths of the couplings, the mass spectrum of the model in question and on the available center-of-mass energy.

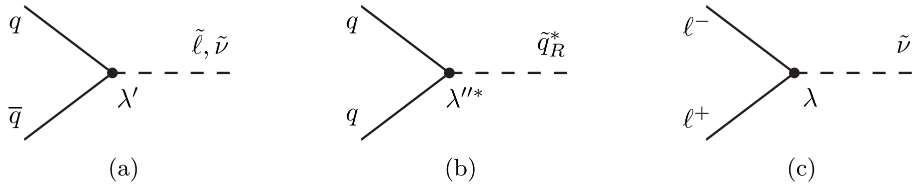

Figure 3.12: Feynman diagrams schematically showing resonant production of sleptons/sneutrinos (a,c) and squarks (b) in case of non-zero $\not{R}_p$ couplings.

Even if the single sparticle production is impossible or highly suppressed, the expected final states can be very different from the R_p conserving case, as the LSP is no longer cosmologically constrained to be weakly interacting and neutral and can in principle be any SUSY particle. In mSUGRA models, for example, the $\tilde{\tau}_1$ is the LSP in large parts of the parameter space. In addition all sparticles coupling to the non-zero $\not{R}_p$ operator(s) can directly decay to SM particles. While typically not the dominant decay mode when compared to gauge-strength interactions, this allows the LSP to decay, without necessarily leaving the missing transverse energy signature expected in R_p conserving models. In principle this even allows a direct reconstruction of the LSP's mass in $\not{R}_p$ models where its decay does not involve neutrinos.

As the lifetime of the LSP increases with smaller values of the $\not{R}_p$ coupling, it can become large enough to show up in searches for signatures expected from long-lived particles, like displaced vertices, or even seem stable on the length scales of today's detectors. This effect can be enhanced if the LSP does not couple to the $\not{R}_p$ operator directly and has to decay via one or two off-shell sparticles.

3.2.8 The Benchmark Point BC1

An example for an R_p violating, but B_3 conserving SUSY model is the benchmark point BC1. It was proposed in [37] and describes a no-scale mSUGRA scenario with one non-zero lepton number violating $\not{R}_p$ coupling at the GUT scale (M_{GUT}). The values of the model parameters are as follows:

- $m_0 = A_0 = 0\,\mathrm{GeV}$
- $m_{1/2} = 400\,\mathrm{GeV}$
- $\tan\beta = 13$
- $\mathrm{sgn}(\mu) = +1$
- $\lambda_{121} = 0.032$ at M_{GUT} $\quad$ (0.048 at M_{EW})

At the LHC with $\sqrt{s} = 7\,\mathrm{TeV}$ the production cross section for this model is about $0.35\,\mathrm{pb}$ at leading order (LO) and $0.42\,\mathrm{pb}$ at next-to-leading order (NLO), including next-to-leading-logarithmic (NLL) corrections from resummation of soft gluon emissions for squark and gluino production. At this point in parameter space about ⅔ of the produced sparticles originate from strong and about ¼ from electroweak production processes. Details on how these numbers were obtained will be provided in Chapter 5.

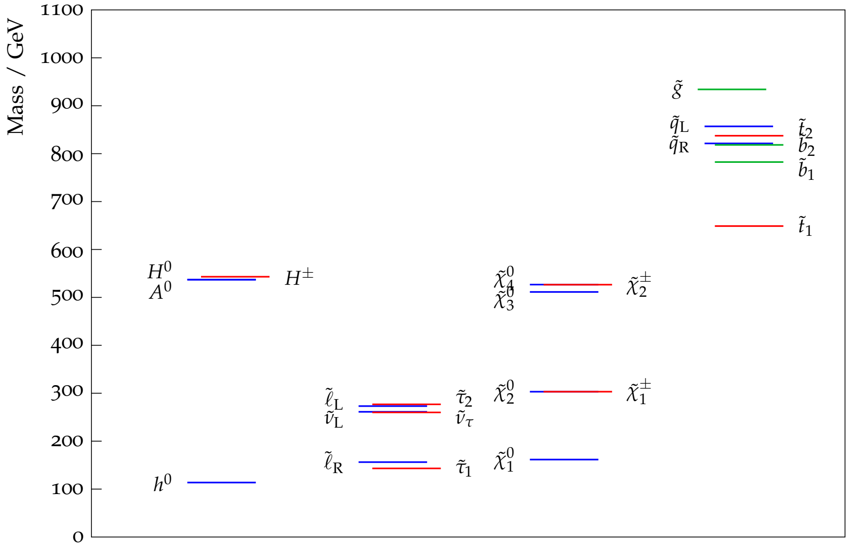

Figure 3.13: Mass spectrum of the benchmark point BC1.

	Mass [GeV]	Decay	BR [%]
$\tilde{\tau}_1^\pm$	143	$e^\mp \overset{(-)}{\nu}_\mu e^\pm \tau^\pm$ $\mu^\mp \overset{(-)}{\nu}_e e^\pm \tau^\pm$	50.1 49.8
$\tilde{e}_R^\pm$	156	$e^\pm \overset{(-)}{\nu}_\mu$ $\mu^\pm \overset{(-)}{\nu}_e$	50.0 50.0
$\tilde{\mu}_R^\pm$	157	$\tilde{\tau}_1^\mp \tau^\pm \mu^\pm$	100.0
$\tilde{\chi}_1^0$	162	$\tilde{\tau}_1^\pm \tau^\mp$ $\tilde{e}_R^\pm e^\mp$ $\tilde{\mu}_R^\pm \mu^\mp$	85.0 8.2 6.8

Table 3.4: Masses and decays of the four lightest supersymmetric particles in the BC1 benchmark model.

The high scale parameters of the model were chosen such that the $\tilde{\tau}_1$ is the LSP, while $\tilde{e}_R$ and $\tilde{\mu}_R$ are co-NLSPs (next-to-lightest supersymmetric particles) and the $\tilde{\chi}_1^0$ is the fourth lightest sparticle only. The remainder of the generated mass spectrum can be seen in Fig. 3.13, where the labels for the almost mass-degenerate sleptons and squarks of the first two families were merged into $\tilde{\ell}_R$, $\tilde{\ell}_L$, $\tilde{q}_R$ and $\tilde{q}_L$, respectively.

At the LHC sparticles in BC1 events would be produced in pairs, like in the typical R_p conserving case, with almost all sparticles cascade-decaying to the LSP. The biggest exception to this decay pattern is the $\tilde{e}_R$, which always decays to an electron or muon and a neutrino. The other sparticles that couple to λ_{121} ($\tilde{\nu}_e$, $\tilde{\nu}_\mu$, $\tilde{e}_L$ and $\tilde{\mu}_L$) only directly decay into SM particles about 8 % of the time. Masses and decays, including the respective branching ratios, of the four lightest SUSY particles in this model are shown in Tab. 3.4[12].

The $\tilde{\tau}_1$, which does not couple directly to the $\not{R}_p$ operator, decays via a virtual $\tilde{\chi}_1^0$ and a virtual $\tilde{e}$ or $\tilde{\mu}$, producing three charged leptons, one of them a tau, and a neutrino. An example of

---

[12] Differences between the table shown here and the numbers given in the paper defining BC1 are due to the use of a newer version of SOFTSUSY for the former.

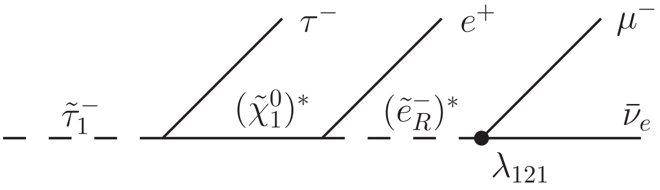

Figure 3.14: Example of a $\tilde{\tau}_1$ LSP four-body decay in the BC1 model.

this is shown in Fig. 3.14. In a typical BC1 event the decays of the two $\tilde{\tau}_1$ will thus result in a final state with at least four light charged leptons (electrons or muons) and missing transverse momentum/energy. The taus resulting from production and decay of the two LSPs can either add jets or further electrons, muons and $E_{\mathrm{T}}^{\mathrm{miss}}$ to this signature.

The discovery potential for the original BC1 model as well as BC1-like models in the surrounding $m_{1/2}$–$\tan\beta$ parameter space, as expected for the early LHC data taking, was studied in [38]. For the evaluation of the signal and the dominant SM background expectations, the fast generic detector simulation Delphes [39] was employed with ATLAS-like settings. The study was updated to use the full ATLAS simulation for the background estimate in [40], where the event selection cuts were re-optimized as well. The search strategy that was proposed in both cases required minimal transverse momenta for at least one muon and at least two electrons as well as additional cuts on the sum of momenta of all leptons. Assuming a strong production scenario, the sum of momenta of the first four jets was chosen to suppress diboson backgrounds, while cuts on $E_{\mathrm{T}}^{\mathrm{miss}}$ were explicitly excluded to stay complementary to R_p conserving SUSY searches. No LHC data was analyzed.

Depending on the measure of significance and the expected size of systematic uncertainties on the background prediction, integrated luminosities between about $5\,\mathrm{fb}^{-1}$ and $50\,\mathrm{fb}^{-1}$ were found [40] to be sufficient to discover BC1-like models up to $m_{1/2} \approx 620\,\mathrm{GeV}$.

In addition, the selection efficiency for hadronic τ leptons using the ATLAS tau identification algorithms was studied in the same reference. It was more than a factor of two below the one found in typical reference events ($Z \to \tau\tau$), discouraging a use of taus for the selection of BC1-like events.

For this thesis a different search strategy was adopted, which will be described in Sec. 4.1.

CHAPTER 4

Analysis

Due to the large number of possible supersymmetric models, searches are usually split into separate analyses based on the predicted final state features, like the number of jets or charged leptons or whether or not missing transverse energy is expected, as this allows choosing the analysis cuts best suited to separate the predicted signal from the expected SM backgrounds. At the same time, finite human and computing resources as well as the desire to combine the results of different searches require a grouping of analyses with common SM backgrounds and object definitions so that for example simulated background events, corrections for known effects and uncertainty estimates can be shared.

Considering this, the search for signals predicted by BC1 or similar models was realized in two steps. It first was combined with similar efforts for R-parity conserving SUSY models into a more general search for supersymmetry in final states containing at least four prompt leptons (electrons or muons, including those from non-hadronic τ decays) and missing transverse energy, which in the following will be referred to as "four lepton analysis". This general search was conducted in collaboration with the ATLAS multi-lepton group and focused on all steps common to SUSY analyses with this final state, while leaving interpretations in terms of specific SUSY models for further studies. A short summary of the analysis was publicly reported in [41] and further details were presented in the internal note [42].

The subsequent interpretation in terms of BC1-like models, which is the main focus of this thesis, will be the subject of Chapter 5.

The following sections will describe the four lepton analysis, beginning with the targeted event signature and the main expected SM backgrounds in Sec. 4.1. A summary of the simulated samples used to estimate the SM backgrounds will be given in Sec. 4.2, followed by a description of the reconstructed electron, muon and jet objects as well as the missing transverse energy as they were used in the analysis in Sec. 4.3. Section 4.4 will describe the preselection of events from the base dataset, followed by an intermediate summary of events with at least four leptons in Sec. 4.5 and the definition of the two signal regions in Sec. 4.6. The next two sections, 4.7 and 4.8, will cover the topics of background estimation and validation as well as the systematic uncertainties. Section 4.9, finally, will summarize the number of events found in the signal regions as well as the resulting limits on SUSY models with final states consisting of four leptons and $E_{\mathrm{T}}^{\mathrm{miss}}$, which can be deduced from them.

4.1 Targeted Event Signature and SM Backgrounds

As explained in Sec. 3.2.8, for the BC1 model, at least four light charged leptons and $E_{\mathrm{T}}^{\mathrm{miss}}$ are expected from the decays of the two $\tilde{\tau}_1$ LSPs. Thus in a search for BC1 it is reasonable to look for a signature of

$$pp \to \quad \geq 4\ell + E_{\mathrm{T}}^{\mathrm{miss}} \quad + X$$

where ℓ now only denotes electrons or muons[1].

In R_p conserving SUSY models the same signature can be found. The two escaping LSPs are a source of $E_{\mathrm{T}}^{\mathrm{miss}}$ and the leptons can be produced in the cascade decays of the initial pair of sparticles, for example in the production and decay of sleptons in the chain, as in $\tilde{\chi}_2^0 \to \ell\tilde{\ell} \to \ell\ell\tilde{\chi}_1^0$, or by radiating electroweak or Higgs bosons, as in $\tilde{q} \to \tilde{q}Z \to \tilde{q}\ell\ell$. Whether or not such decays are possible or maybe even enhanced strongly depends on the sparticle mass spectrum of the particular SUSY model.

Standard model backgrounds for this final state, especially fully hadronic ones, are severely suppressed by the requirement of four or more leptons already. This leaves mainly diboson decays in the form of $ZZ \to 4\ell$ and decays of top quark pairs as in $t\bar{t} \to b\bar{b}\,WW \to c\bar{c}\,WWWW \to$ 2jets + 4ℓ + $E_{\mathrm{T}}^{\mathrm{miss}}$ or top quarks in association with a vector boson as in $t\bar{t}Z \to b\bar{b}\,WWZ \to$ 2(b-)jets + 4ℓ + $E_{\mathrm{T}}^{\mathrm{miss}}$ as real backgrounds. On top of that processes in which one or more “fake” leptons originate from misidentification of a jet have to be taken into account, as in $WZ+\mathrm{jet} \to 3\ell + E_{\mathrm{T}}^{\mathrm{miss}} + "\ell"$ or $Z+2\mathrm{jets} \to 2\ell + 2"\ell"$. To reduce the contribution of these backgrounds, cuts on a minimal $E_{\mathrm{T}}^{\mathrm{miss}}$ are introduced as well as an optional veto of Z bosons, realized by cutting on the invariant mass of lepton pairs with the same flavor and opposite sign.

To study the SM backgrounds and determine cuts compatible with a variety of possible SUSY models, Monte Carlo (MC) simulated events were used.

4.2 Monte Carlo Simulated Background Samples

This section will summarize the samples of MC events which were used to estimate the standard model background for the SUSY four lepton analysis.

The diboson samples containing ZZ, WZ and opposite-sign W^+W^- processes (including off-shell bosons) were produced using the event generator Herwig [43] with the MRST2007/LO* set of modified leading-order parton distribution functions (PDFs) [44]. Their cross sections, rescaled to NLO values [45], as well as the integrated luminosity corresponding to the number of

---

[1] As the identification of electrons and muons is much simpler than that of taus and the presence of neutrinos only leads to additional $E_{\mathrm{T}}^{\mathrm{miss}}$, in an experimental context the meaning of “(charged) lepton” is often reduced to designate electron and muon only. It will be used as such in the following and taus or neutrinos will be mentioned explicitly.

events produced are listed in Tab. 4.1. The ZZ and WZ samples were filtered at generator level to require at least one W or Z boson to decay into a lepton with $p_{\mathrm{T}} > 10\,\mathrm{GeV}$ and $|\eta| < 2.8$. The WZ sample required at least three such leptons. The reduced cross sections, taking into account the generator filter efficiencies (ϵ), are given in the same table. The same-sign $W^{\pm}W^{\pm}$(+jet) samples were produced unfiltered, using Madgraph [46] to simulate the tree-level processes.

The $W^{\pm}/Z + \gamma$ samples, subdivided into separate weak boson decay channels, were also generated using Madgraph, but were filtered at generator level requiring the W or Z to decay to leptons with $p_{\mathrm{T}} > 10\,\mathrm{GeV}$ and $|\eta| < 2.5$ and to contain a photon with $p_{\mathrm{T}} > 7\,\mathrm{GeV}$ and $|\eta| < 2.5$. The samples' LO cross sections [47] as well as their integrated luminosities can be found in the second part of Tab. 4.1. The Madgraph samples used the PDF set CTEQ6L1 [48].

Table 4.2 shows the NNLO cross sections [49–52], that the samples containing $t\bar{t}$ and single top processes were normalized to, as well as their integrated luminosities. The samples were generated using the NLO MC generator MC@NLO [53] with CTEQ6.6 NLO PDFs [48]. The sample tagged "not all-hadronic" was filtered at generator level to require at least one leptonically decaying top quark. MC events of $t\bar{t}$ processes including additional weak bosons (and jets) were simulated as well, using Madgraph with CTEQ6L1 PDFs. The cross sections, rescaled to NLO [54], and the corresponding integrated luminosities are given in Tab. 4.3.

Samples of processes involving a single weak boson and additional jets were generated using Alpgen [55] with the same set of PDFs as for Madgraph. Individual subsamples were produced for each type of lepton resulting from the boson decay (e.g. $Z \to ee$ or $W \to \tau\nu_{\tau}$) and number of additional partons generated in the process (NpX). The samples with light-flavor (u, d, s) and c jets, designated $Z/W+$ jets, were filtered on generator level to include only Z and W bosons with an invariant mass of the resulting lepton pair of more than $40\,\mathrm{GeV}$. Samples with pairs of b jets, tagged Z/Wbb, were produced with a generator boson mass cut of $30\,\mathrm{GeV}$. In addition, the $Zbb \to ee/\mu\mu/\tau\tau$ samples were filtered to contain three leptons (here e, μ or τ) from the Z and b decays with $p_{\mathrm{T}} > 5\,\mathrm{GeV}$ and $|\eta| < 10$. In order to cover the boson mass range between $10\,\mathrm{GeV}$ and $40\,\mathrm{GeV}$, Drell–Yan samples ($Z^{*}/\gamma^{*} +$ jets) were used as well. The corresponding cross sections, normalized to NNLO [56–58], and sample luminosities are given in Tab. 4.4.

Samples of fully hadronic events were analyzed as well, but their contribution was found to be negligible after the four lepton requirement, as expected.

The generator level cuts mentioned above did not affect the analysis, as the individual and combined requirements placed on the analysis objects given in Sec. 4.3 were more restrictive.

The Herwig, Alpgen and MC@NLO samples used Herwig to simulate the hadronization process of the partons generated in the hard interaction and Jimmy [59] to model the "underlying event", i.e. the additional soft interactions caused by the proton remnants. The Madgraph samples used Pythia [60] for these purposes. Simulation of the full detector response was performed as described in [61] with a program based on GEANT4 [62]. Background effects originating from processes in the ATLAS cavern, from the interaction of the beam with the upstream accelerator elements and the residual gasses in the beam pipe were taken into account by overlaying detector hits from events separately generated. Additional proton–proton interactions in the same bunch crossing as well as overlapping signals in the detector from interactions in neighboring bunch crossings ("in-time" and "out-of-time pileup", respectively) had to be modeled as well, by overlaying a number of soft-scattering events, to account for the resulting effects in the readout

Process	Generator	σ [pb]	$\sigma \times \epsilon$ [pb]	$\int \mathcal{L}\, dt$ [fb^{-1}]
ZZ	Herwig	7.08	1.31	190.4
WZ	Herwig	19.11	0.25	199.4
W^+W^-	Herwig	52.5	17.02	14.7
$W^\pm W^\pm + \text{jet}$	Madgraph	0.22	0.22	433.03
$W^+\gamma$ $(e\nu)$	Madgraph	27.97	27.97	1.8
$W^+\gamma$ $(\mu\nu)$	Madgraph	27.94	27.94	1.8
$W^+\gamma$ $(\tau\nu)$	Madgraph	25.42	4.32	11.0
$W^-\gamma$ $(e\nu)$	Madgraph	18.59	18.59	2.7
$W^-\gamma$ $(\mu\nu)$	Madgraph	18.59	18.59	2.7
$W^-\gamma$ $(\tau\nu)$	Madgraph	16.86	2.87	17.1
$Z\gamma$ (ee)	Madgraph	10.02	10.02	5.0
$Z\gamma$ $(\mu\mu)$	Madgraph	10.02	10.02	5.0
$Z\gamma$ $(\tau\tau)$	Madgraph	9.76	1.66	29.6

Table 4.1: The diboson samples used for the four lepton analysis, generated with Herwig and Madgraph. The NLO (LO for $W^\pm/Z\gamma$) cross sections are given without and including the generator filter efficiency. The integrated luminosities corresponding to the total statistics in each sample are also given. Adapted from [42].

Process		σ [pb]	$\int \mathcal{L}\, dt$ [fb^{-1}]
$t\bar{t}$	not all-hadronic	89.36	129.49
	all-hadronic	75.21	12.34
Single t	t-channel $e\nu$	7.12	24.95
	t-channel $\mu\nu$	7.12	24.93
	t-channel $\tau\nu$	7.10	24.97
	s-channel $e\nu$	0.47	540.04
	s-channel $\mu\nu$	0.47	539.50
	s-channel $\tau\nu$	0.47	539.67
	Wt	14.59	54.65

Table 4.2: The top-quark samples used for the four lepton analysis, generated with MC@NLO. The NNLO cross sections are given, taking into account any generator filter efficiency as well as the k-factors used to rescale the cross sections. The integrated luminosities corresponding to the total statistics in each sample are also given. Adapted from [42].

Process	σ [pb]	$\int \mathcal{L}\, dt$ [fb^{-1}]
$t\bar{t}\,W$	0.17	577.7
$t\bar{t}\,W + \text{jet}$	0.12	861.1
$t\bar{t}\,Z$	0.13	752.0
$t\bar{t}\,Z + \text{jet}$	0.11	880.6
$t\bar{t}\,WW$	0.002	57 541.3

Table 4.3: The top+boson samples used for the four lepton analysis, generated with Madgraph. The NLO cross sections are given, taking into account any generator filter efficiency as well as the k-factors used to rescale the cross sections. The integrated luminosities corresponding to the total statistics in each sample are also given. Adapted from [42].

Process		σ [pb]	$\int \mathcal{L}\, dt$ [fb^{-1}]	Process		σ [pb]	$\int \mathcal{L}\, dt$ [fb^{-1}]
Z+jets	(ee+Np0)	835.40	7.9	W+jets	($e\nu$+Np0)	8305.92	0.4
	(ee+Np1)	167.95	7.9		($e\nu$+Np1)	1565.16	0.4
	(ee+Np2)	50.68	8.0		($e\nu$+Np2)	453.95	8.3
	(ee+Np3)	13.95	7.9		($e\nu$+Np3)	121.72	8.3
	(ee+Np4)	3.60	8.3		($e\nu$+Np4)	31.04	8.0
	(ee+Np5)	1.04	8.7		($e\nu$+Np5)	8.40	8.3
	($\mu\mu$+Np0)	835.85	7.9		($\mu\nu$+Np0)	8303.52	0.4
	($\mu\mu$+Np1)	167.68	8.0		($\mu\nu$+Np1)	1565.04	0.4
	($\mu\mu$+Np2)	50.41	8.0		($\mu\nu$+Np2)	453.40	8.3
	($\mu\mu$+Np3)	13.99	7.9		($\mu\nu$+Np3)	122.26	8.3
	($\mu\mu$+Np4)	3.44	8.7		($\mu\nu$+Np4)	30.90	8.2
	($\mu\mu$+Np5)	0.96	10.4		($\mu\nu$+Np5)	8.30	8.4
	($\tau\tau$+Np0)	835.50	7.9		($\tau\nu$+Np0)	8302.32	0.4
	($\tau\tau$+Np1)	168.51	7.9		($\tau\nu$+Np1)	1563.84	0.4
	($\tau\tau$+Np2)	50.45	8.0		($\tau\nu$+Np2)	453.82	8.3
	($\tau\tau$+Np3)	14.06	7.8		($\tau\nu$+Np3)	121.81	8.3
	($\tau\tau$+Np4)	3.49	8.6		($\tau\nu$+Np4)	30.77	8.1
	($\tau\tau$+Np5)	0.96	10.4		($\tau\nu$+Np5)	8.45	7.5
Zbb	(ee+Np0)	1.03	200.2	Zbb	($\mu\mu$+Np0)	1.03	194.2
	(ee+Np1)	0.59	170.7		($\mu\mu$+Np1)	0.61	166.6
	(ee+Np2)	0.25	163.2		($\mu\mu$+Np2)	0.24	166.4
	(ee+Np3)	0.13	157.8		($\mu\mu$+Np3)	0.13	152.6
Zbb	($\tau\tau$+Np0)	11.50	13.0	Wbb	(W+Np0)	4.01	1.6
	($\tau\tau$+Np1)	4.36	22.9		(W+Np1)	3.22	1.7
	($\tau\tau$+Np2)	1.56	25.7		(W+Np2)	1.67	1.8
	($\tau\tau$+Np3)	0.68	13.2		(W+Np3)	0.79	1.9
DY	(ee+Np0)	3819.00	0.3	DY	($\mu\mu$+Np0)	3818.63	0.3
	(ee+Np1)	106.15	2.8		($\mu\mu$+Np1)	106.09	2.8
	(ee+Np2)	51.75	9.7		($\mu\mu$+Np2)	51.81	9.6
	(ee+Np3)	10.48	14.3		($\mu\mu$+Np3)	10.48	14.3
	(ee+Np4)	2.31	17.3		($\mu\mu$+Np4)	2.31	17.3
	(ee+Np5)	0.58	17.4		($\mu\mu$+Np5)	0.58	17.4
DY	($\tau\tau$+Np0)	3818.88	0.3				
	($\tau\tau$+Np1)	106.16	2.8				
	($\tau\tau$+Np2)	51.84	9.6				
	($\tau\tau$+Np3)	10.45	14.3				
	($\tau\tau$+Np4)	2.31	17.3				
	($\tau\tau$+Np5)	0.58	17.4				

Table 4.4: The Z+jets, W+jets, Zbb, Wbb and Drell–Yan (DY) samples used for the four lepton analysis generated using Alpgen. The NNLO cross sections are given, taking into account any generator filter efficiency as well as the k-factors used to rescale the cross sections. The integrated luminosities corresponding to the total statistics in each sample are also given. Adapted from [42].

and reconstruction. The number of such simulated pileup events was varied when generating the MC samples to cover the initially estimated distribution for the 2011 data-taking periods. For the further treatment of pileup see Sec. 4.4.5 below.

To give an impression of possible signal contributions, some of the figures below also include distributions for two SUSY models that were used as benchmark scenarios for the analysis. The first model, labelled "DGwSL"[2], was an R_p conserving scenario where charginos and neutralinos were directly produced, leading to a multi-lepton and $E_{\mathrm{T}}^{\mathrm{miss}}$ signature by decaying into the lightest neutralinos via sleptons. The second model, labelled "RPV", was an $\not{R}_p$ scenario very similar[3] to BC1.

4.3 Analysis Object Definitions

While analysis strategies or search channels are typically thought of in terms of "physical" objects or quantities like "electron", "jet" or "total missing transverse energy", the reconstruction and identification used to extract this type of high-level information from the raw data measured in the sub-detectors leaves quite a number of choices, including the type and settings of the algorithms used for tasks like calibration, pattern matching or combining the response of different sub-detectors. Achieving the best possible performance and understanding for these high-level objects and quantities in data and MC requires a dedicated effort, in this case provided by the ATLAS sub-detector experts and the EGamma Working Group, the Muon Combined Performance Group and the Jet/$E_{\mathrm{T}}^{\mathrm{miss}}$ Working Group. As different types of analyses still have varying requirements e.g. concerning the identification efficiencies/purities of the objects actually used, typically a number of recommendations of possible "working points" are provided by these groups together with uncertainty estimates.

To allow for the combination of results, the definitions used in the ATLAS SUSY searches follow the same or at least compatible recommendations.

The remainder of this section will give a brief overview of the definitions as they were used in the four lepton analysis, starting with the charged leptons, followed by jets, which were needed for the basic "event cleaning" (cf. Sec. 4.4.1), for the removal of objects that fulfill the requirements of more than one identification hypothesis (cf. Sec. 4.3.4), as well as for the $E_{\mathrm{T}}^{\mathrm{miss}}$ definition, given in Sec. 4.3.6.

4.3.1 Electrons

The electron objects were based on two algorithms. The first was seeded by "clusters" of energy deposits in the EM calorimeter, found using a sliding-window algorithm, which could be matched to an inner detector track, and was optimized for high-p_{T} electrons. The second was seeded by tracks in the inner detector and optimized for soft electrons as well as electrons within jets. The electrons were required to pass a number of low-level cuts based on information about the shower shape in the EM calorimeter, energy leakage into the hadronic calorimeters

---

[2] short for: Direct Gaugino production with SLeptons in the decay chain

[3] $\tan\beta$ was set to 22 instead of 13.

and the quality of the track as well as the track–cluster matching, equivalent to the medium-level selection as described in [63].

The E_{T}- and η-dependent electron energy scale (EES) and resolution (EER) and their uncertainties were determined by the EGamma Working Group with the tag-and-probe method given in the reference above, using $Z \to ee$, $W \to e\nu$ and, for low-p_{T} electrons, $J/\Psi \to ee$ events from $40\,\mathrm{pb}^{-1}$ of 2010 data. The scale was found to be compatible with unity. The constant part of the relative resolution $\frac{\sigma_E}{E}$ was about 1.2 % in the barrel region and 1.8 % in the end-caps.

In MC the electron energy was smeared to reproduce the resolution observed in data, as recommended by the ATLAS EGamma Working Group.

The following additional cuts were applied for the "baseline electron" objects:

- $E_{\mathrm{T}} > 10\,\mathrm{GeV}$ (15 GeV in the barrel/end-cap transition region $1.37 < |\eta^{\mathrm{cl}}| < 1.52$)
- $|\eta^{\mathrm{cl}}| < 2.47$, where $|\eta^{\mathrm{cl}}|$ is the pseudorapidity of the associated calorimeter cluster
- Electrons affected by the LAr calorimeter readout problem mentioned in Sec. 4.4.1 below were discarded.

4.3.2 Muons

The muon objects were reconstructed using a statistical combination ("STACO") algorithm [13, 64], combining either a reconstructed muon spectrometer (MS) track with a matched inner detector (ID) track ("combined muons") or an extrapolated ID track and one or more track segments in the MS ("segment-tagged muons").

The muon momentum resolution was studied in cosmic-ray events recorded in 2009 [65]. For combined muons the constant and linear (in p_{T}) parts of the relative resolution $\frac{\sigma_{p_{\mathrm{T}}}}{p_{\mathrm{T}}}$ were determined as about 1.6 % and 23×10^{-3} %/GeV, respectively.

To reproduce the resolution observed in data, the p_{T} of muons had to be shifted and smeared in MC. The procedure recommended by the ATLAS Muon Combined Performance Group [66] was followed. It required separate smearing of the ID and MS measurements and an additional smearing of the p_{T} of the re-combined muon, as well as a shift of the combined scale.

For "baseline muon" objects additional cuts were applied:

- $p_{\mathrm{T}} > 10\,\mathrm{GeV}$
- $|\eta| < 2.40$
- Further track quality cuts based on the number of hits, holes and outliers in the Pixel, SCT and TRT.

4.3.3 Jets

Jets were reconstructed using the anti-k_T jet algorithm [67] with a radius parameter $R = 0.4$, based on “topological” clusters of calorimeter cells. These clusters were seeded by calorimeter cells with energy significantly above the measured noise and neighboring cells were iteratively added as long as above a lower threshold, as described in [68].

The measured jet energies were corrected for the fact that the ATLAS calorimeter’s response is tuned to be suitable for electromagnetic showers und systematically underestimates the energy deposited by hadronic objects, as well as for dead material and other effects, using p_T- and η-dependent “jet energy scale” (JES) calibration factors obtained from MC simulation [69] and validated with test-beam and collision data [70].

The jet energy resolution was studied in [71] for 2010 data and recently updated for a dataset of $4.5\,\mathrm{fb}^{-1}$ recorded in 2011 [72]. For the jet objects used in the four lepton analysis the relative resolution $\frac{\sigma_{p_\mathrm{T}}}{p_\mathrm{T}}$ was found to be about 25 %, 13 % and 7.5 % for jets with a p_T of 25 GeV, 100 GeV and 400 GeV, respectively, in the lowest rapidity[4] bin, $|y| \leq 0.8$, and smaller for higher rapidities.

Jets had to meet the following requirements:

- $p_\mathrm{T} > 20\,\mathrm{GeV}$
- $|\eta| < 2.8$

4.3.4 Overlap Removal

By construction, electrons seeded by calorimeter information are reconstructed both by the electron and jet finding algorithms. Jet objects therefore were discarded, if they were found to be closer than $\Delta R = 0.2$ to a baseline electron object.

The jets remaining after the overlap removal with electrons still can contain leptons from semileptonic b or c decays, which were not part of the SUSY signature searched for. While such leptons generally are rejected by requiring “signal leptons” to be isolated within narrow cones (cf. Sec. 4.3.5), a considerable number of leptons, mainly muons, was still found to be close to some jet’s axis. To specifically target these, all leptons were required to be separated by more than $\Delta R = 0.4$ from the closest jet.

If a muon produces bremsstrahlung in the detector the photon can sometimes be misidentified as an electron, resulting in two closely overlapping badly reconstructed muon and electron objects. To prevent using such objects, if an electron and a muon were found to overlap within $\Delta R = 0.1$, they were both discarded.

---

[4] The rapidity is defined as $y = 0.5 \ln \frac{E+p_z}{E-p_z}$.

4.3.5 Isolation Requirements for Signal Leptons

Following the overlap removal, “signal electrons” and “signal muons” were required to be isolated. Good measures of isolation were studied separately, e.g. in the ATLAS cross section measurement of W + jets events [73]. The two variables that were used for the four lepton analysis were the summed p_{T} of other tracks within a cone of $\Delta R \leq 0.2$ around the lepton ($p_{\mathrm{T}}^{\mathrm{cone20}}$) and the summed E_{T} in the calorimeter within $\Delta R \leq 0.3$ of the lepton ($E_{\mathrm{T}}^{\mathrm{cone30}}$).

A signal electron required:

- $p_{\mathrm{T}}^{\mathrm{cone20}}/E_{\mathrm{T}} < 0.1$

while the requirements for a signal muon were chosen to be:

- $p_{\mathrm{T}}^{\mathrm{cone20}} < 1.8\,\mathrm{GeV}$ and
- $E_{\mathrm{T}}^{\mathrm{cone30}} < 4\,\mathrm{GeV}$

where the $E_{\mathrm{T}}^{\mathrm{cone30}}$ cut for muons was added to work around some discrepancies seen between data and MC in the muon channels of several other analyses.

The lepton isolation efficiency was determined using $Z/\gamma^* \to \ell^+\ell^-$ events from a dataset of $1\,\mathrm{fb}^{-1}$ from 2011 and corresponding Z/γ^* + jets MC events. To do this, the tag-and-probe method used in [74] was adapted to the specific isolation cuts and jet overlap removal used in the four lepton analysis. For electrons efficiencies between 98 % and 100 % were found, depending on the event’s jet multiplicity and η, with the lowest values for higher jet multiplicities and the barrel–end-cap transition region. In the case of muons efficiencies between 66 % and 97 % were determined, again depending on jet multiplicity and η, with higher jet multiplicities and more central values of η leading to the lower efficiency values.

4.3.6 Missing Transverse Energy

The definition of the “missing transverse energy”, $E_{\mathrm{T}}^{\mathrm{miss}}$, was based on the vector sum of the transverse momenta of the reconstructed objects:

$$E_{x/y}^{\mathrm{miss}} = E_{x/y}^{\mathrm{miss,e}} + E_{x/y}^{\mathrm{miss},\mu} + E_{x/y}^{\mathrm{miss,jets}} + E_{x/y}^{\mathrm{miss,cl}} \tag{4.1}$$

and

$$E_{\mathrm{T}}^{\mathrm{miss}} = \sqrt{(E_x^{\mathrm{miss}})^2 + (E_y^{\mathrm{miss}})^2}$$

where the electron term ($E_{x/y}^{\mathrm{miss,e}}$) was calculated using the signal electrons and the muon term ($E_{x/y}^{\mathrm{miss},\mu}$) using all muons passing the basic selections (i.e. not requiring isolation). The jet term ($E_{x/y}^{\mathrm{miss,jets}}$) was calculated using all jet objects as defined above, but extending the angular coverage to $|\eta| < 4.9$. The contributions of all topological clusters not associated with reconstructed electrons or jets ($E_{x/y}^{\mathrm{miss,cl}}$[5]) were added as well.

---

[5] This is also called the “CELLOUT” term in some support documents.

The $E_{\mathrm{T}}^{\mathrm{miss}}$ resolution was studied in $Z \to \ell\ell$ and $W \to \ell\nu$ events for $36\,\mathrm{pb}^{-1}$ of 2010 data in [75] and more recently for $4.2\,\mathrm{fb}^{-1}$ of data taken in 2011 in [76]. The resolution of $E_{x/y}^{\mathrm{miss}}$ can be parametrized as $\sigma_{E_{x/y}^{\mathrm{miss}}} = k \cdot \sqrt{\sum E_{\mathrm{T}}}$. For the pileup conditions of 2010 and 2011 values of $k \approx 0.5\,\mathrm{GeV}^{1/2}$ and $0.7\,\mathrm{GeV}^{1/2}$ were determined.

4.4 Event Preselection

The analysis was based on a subset[6] of the data taken by ATLAS in 2011. At the most general level all considered runs were delivered during stable beam conditions as declared by the LHC and were flagged by the ATLAS data quality monitoring to have been recorded while the detector was at nominal high voltage and operating properly overall. Additionally the ATLAS solenoid and toroid magnets were on and the sub-detectors necessary for electron, muon and jet identification and reconstruction were running at nominal conditions. These requirements amounted to a base dataset with an integrated luminosity of $2.06\,\mathrm{fb}^{-1}$.

Events from this base dataset were further required to pass a set of basic cleaning cuts and to have fired a subset of triggers, as given below, where additional event preselection cuts and event weight corrections for MC are summarized as well.

4.4.1 Event Cleaning

In data, events were discarded if they contained objects that were identified as jets with $p_{\mathrm{T}} > 20\,\mathrm{GeV}$ and $|\eta| < 2.8$ and passed overlap removal with electrons, but could be associated with calorimeter effects, like coherent noise in the EM calorimeter, energy “spikes” in the hadronic end-caps or energy deposits from cosmic muons or beam background. Data events which exhibited data integrity errors in the LAr calorimeters were removed as well.

With the leading primary vertex of the reconstructed event defined as the one with the largest sum of squared transverse momenta of the associated tracks, events were required to have more than four tracks associated to that vertex, to ensure that only actual collision events were selected.

If a baseline muon passed the requirements of overlap removal, but had a longitudinal impact parameter $|z_0| > 1\,\mathrm{mm}$ or a transverse impact parameter $|d_0| > 0.2\,\mathrm{mm}$, both with respect to the primary vertex, the event was discarded as a possible cosmic ray candidate.

In addition about 42 % of the dataset suffered from a readout problem of the LAr calorimeter in an area given by: $-0.1 < \eta < 1.5$ and $-0.9 < \phi < -0.5$. As this caused mis-measurements for jets and electrons and influenced the $E_{\mathrm{T}}^{\mathrm{miss}}$ measurement, events in the affected data periods and a corresponding fraction of MC were discarded, if a jet was found inside this region with $p_{\mathrm{T}} > 40\,\mathrm{GeV}$ (with p_{T} corrected for dead calorimeter cells, to provide a response similar to MC).

---

[6] up to and including period K

4.4.2 Trigger

Events in data were required to have been flagged by the high-level trigger, requiring a single electron with $E_\mathrm{T} > 20\,\mathrm{GeV}$ or a single muon with $p_\mathrm{T} > 18\,\mathrm{GeV}$. For the later data taking periods the threshold for the electron trigger had to be raised to 22 GeV to cope with higher trigger rates at increasing luminosity. To ensure that the corresponding trigger efficiencies were in their plateau region, the triggering signal leptons were required to have $E_\mathrm{T} > 25\,\mathrm{GeV}$ for an electron or $p_\mathrm{T} > 20\,\mathrm{GeV}$ for a muon. To meet the requirements used to derive the weights necessary for the MC reweighting explained below, the leptons also had to unambiguously match an object reconstructed at trigger level within $\Delta R < 0.15$.

For MC, instead of using the existing trigger simulation, a trigger efficiency measurement was performed on data, using a $Z \to \ell^+\ell^-$ tag-and-probe method to determine the trigger response to signal electrons or muons in bins of η, ϕ and E_T for electrons and p_T for muons, respectively. Different types of muon reconstruction (combined/segment-tagged muon) were treated separately.

In case of electrons efficiencies between 96 % and 98 % in E_T and ϕ were found and between 87 % and 99 % in η, with the smallest values in the barrel–end-cap transition region and for η close to 2.47, at the edge of the acceptance region. For muons the plateau efficiencies were determined to be on average about 77 % (70 % for some data taking periods with slightly different trigger definitions) in the barrel and about 87 % in the end-caps.

The resulting trigger efficiency maps were then applied to the MC in the form of event weights. In this way a larger fraction of the available MC sample statistics could be kept and only a single efficiency measurement was necessary per trigger. In cases where more than one lepton was capable of triggering the event, the event weight was corrected using a factor of

$$\varepsilon = 1 - \prod_i (1 - \varepsilon_i) \tag{4.2}$$

where ε_i are the efficiencies for the individual leptons ℓ_i. The $E_\mathrm{T}/p_\mathrm{T}$ and trigger object matching requirements for the leptons were the same as for data events.

4.4.3 Low Invariant Mass Cut

In order to suppress potential backgrounds due to Drell–Yan, $W/Z\gamma$ and photon conversion processes or decays of low-mass particles such as J/Ψ resonances, events were discarded if they contained baseline lepton pairs of same flavor and opposite sign (SFOS), passing overlap removal, with a combined invariant mass below 20 GeV.

4.4.4 Correction of the Lepton Identification and Reconstruction Efficiency

The identification and reconstruction efficiencies for electrons, as reported in [77], were determined based on the tag-and-probe method explained in [63], using $Z \to ee$, $W \to e\nu$ and $J/\psi \to ee$ events, but updated for the full 2011 dataset ($4.7\,\mathrm{fb}^{-1}$). Identification efficiencies between 77 % and 92 % were found, depending on E_T. The η-averaged reconstruction efficiency was between 90 % and 96 %, depending on E_{T}, with slightly lower values for high-$|\eta|$ and slightly higher values in the central region.

The reconstruction efficiency for muons was reported in [78], based on a tag-and-probe method using $Z \to \mu\mu$ and $J/\psi \to \mu\mu$ events selected from $42\,\mathrm{pb}^{-1}$ of 2010 data. In η the efficiency varied between 95 % (close to $|\eta| \approx 2.47$) and 100 %, with the exception of a small region around $\eta \approx 0$, which had a lower value of about 87 %, as the muon system has less chambers there to provide the space necessary for servicing the inner detector and calorimeters. The η-averaged efficiency was between 97 % and 99 %, depending on p_{T}.

To account for the differences between data and simulation, corrections in the form of event weights were applied to MC events, as recommended by the EGamma Working Group and the Muon Combined Performance Group. These weights consisted of the product of scale factors applied for each signal lepton. The electron efficiency scale factor was η- and E_{T}-dependent, taking values between 0.95 and 0.99 for electrons with $p_{\mathrm{T}} > 20\,\mathrm{GeV}$ and starting from 0.84 for electrons with p_{T} between 10 GeV and 20 GeV. The muon efficiency scale factor was η- and p_{T}-dependent, with values between 0.91 and 1.01 for the muons considered.

4.4.5 Correction of the MC-Based Estimate of Pileup Effects

As mentioned in Sec. 4.2 the initial distribution of pileup included in the samples of simulated events could only be estimated based on the expectations for 2011 data taking. In order to correct for the differences compared to the actually observed pileup distributions for each data-taking period, MC events were reweighted to match the observed average number of interactions per bunch crossing. The average was taken across all bunch crossings of a “luminosity block”[7] (LB) as well as across all bunches of the 50 ns-spaced groups of protons called “bunch-trains”, as this best described the effects of the out-of-time pileup.

---

[7] the smallest amount of data the luminosity is determined for

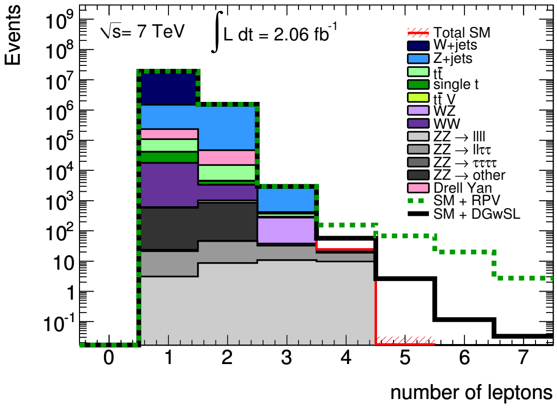

Figure 4.1: Multiplicity of baseline leptons for events passing the preselection. At least one lepton had to fulfill the trigger requirements. [42]

$\geq 4\ell$	All	$eeee$	$eee\mu$	$ee\mu\mu$	$e\mu\mu\mu$	$\mu\mu\mu\mu$
$t\bar{t}$	0.22 ± 0.15	0.012 ± 0.042	0.06 ± 0.06	0.10 ± 0.07	0.05 ± 0.07	0 ± 0.018
Single t	0 ± 0.04	0 ± 0.04	0 ± 0.04	0 ± 0.04	0 ± 0.04	0 ± 0.04
$t\bar{t}V$	0.59 ± 0.26	0.086 ± 0.043	0.14 ± 0.07	0.17 ± 0.08	0.13 ± 0.06	0.07 ± 0.04
ZZ	19 ± 5	3.8 ± 1.0	0.16 ± 0.08	10.0 ± 2.5	0.17 ± 0.07	4.9 ± 1.2
WZ	0.54 ± 0.17	0.06 ± 0.03	0.07 ± 0.04	0.17 ± 0.07	0.24 ± 0.09	0 ± 0.011
WW	0 ± 0.015	0 ± 0.015	0 ± 0.015	0 ± 0.015	0 ± 0.015	0 ± 0.015
$Z\gamma$	0 ± 0.5	0 ± 0.5	0 ± 0.5	0 ± 0.5	0 ± 0.5	0 ± 0.5
Z+LFjets	3.8 ± 1.6	1.8 ± 0.9	0 ± 0.29	1.5 ± 1.1	0.6 ± 0.6	0 ± 0.29
Z+HFjets	0.26 ± 0.28	0.022 ± 0.037	0.06 ± 0.07	0.13 ± 0.14	0.05 ± 0.06	0.0021 ± 0.0034
Drell–Yan	0 ± 0.29	0 ± 0.14	0 ± 0.018	0 ± 0.14	0 ± 0.06	0 ± 0.014
$\sum$ SM	25 ± 5	5.8 ± 1.4	0.5 ± 0.6	12.0 ± 2.8	1.2 ± 0.7	5.0 ± 1.4
Data	24	8	2	8	0	6

Table 4.5: Number of events passing preselection and with at least four signal leptons for SM MC and $2.06\,\mathrm{fb}^{-1}$ of 2011 data. Adapted from [41].

4.5 Events with at least Four Signal Leptons

Following the event preselection, only events with four or more signal leptons were selected for the analysis described here. This was done to remove the overlap with similar SUSY searches, targeting signatures for which exactly one, two or three leptons were expected, to allow for a later combination of results.

This requirement already causes a big reduction of expected SM background, as can be seen in Fig. 4.1, which shows the lepton multiplicity of the SM backgrounds, where at least one of the selected leptons had to pass the harder $E_\mathrm{T}/p_\mathrm{T}$ cuts given in Sec. 4.4.2 to match the trigger requirement in data.

A summary of the number of events that passed the preselection requirements and had at least four signal leptons are shown in Tab. 4.5, for all leptons combined as well as separated into the different lepton flavor combinations found. The expected numbers given for the SM MC samples include statistical and systematic (covered in Sec. 4.8) uncertainties, added in quadrature.

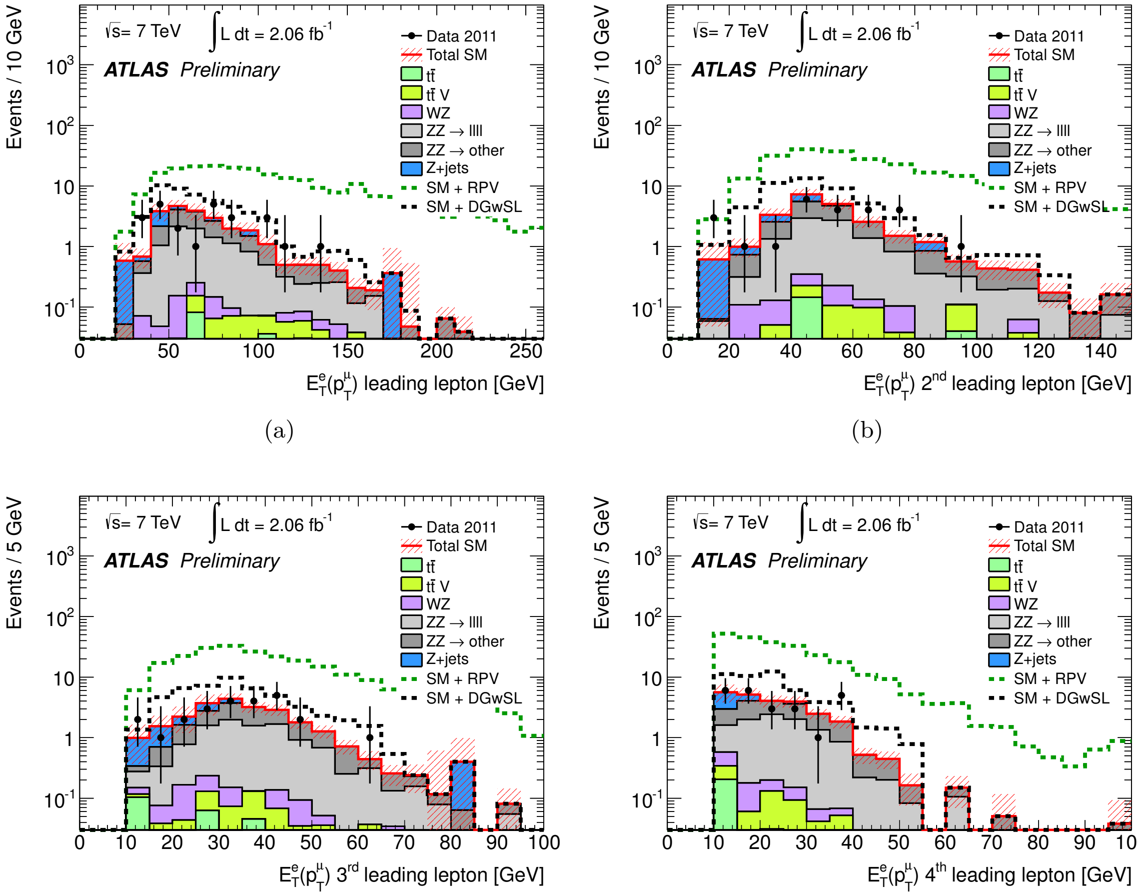

(a)

(b)

(c)

(d)

Figure 4.2: $E_{\mathrm{T}}^{e}/p_{\mathrm{T}}^{\mu}$ distributions of (a) the leading, (b) second-leading, (c) third-leading and (d) fourth-leading lepton in events passing preselection and with at least four signal leptons for 2011 data and MC simulation. The hashed band represents statistical and systematic uncertainties added in quadrature. [41]

In general the statistical uncertainties given for MC samples in the tables in this and the following sections were calculated as $\sigma_{\text{stat.}} = s \times \sqrt{\sum \omega^2}$, where ω is the MC event weight combining the scale factors for trigger, lepton efficiencies and pileup, and s is the factor applied to scale the MC events to a luminosity of $2.06\,\mathrm{fb}^{-1}$. In cases where at least two real leptons were expected for a MC sample i, but no events remained after a cut, an upper limit of $1.1 \cdot \mathcal{L}^{\text{data}}/\mathcal{L}_i^{\text{MC}}$ was used to estimate the uncertainty. The factor of 1.1 is given by the mean of a Poisson distribution, which yields zero events with a probability of 0.32%. For the low mass Drell–Yan samples ($10\,\mathrm{GeV} < m_Z < 40\,\mathrm{GeV}$) it was possible to get a better estimate, based on the ratio of the number of low mass DY to Z+jets ($m_Z > 40\,\mathrm{GeV}$) events in two and three lepton events, for which much higher MC statistics was available. As a result an upper limit on the uncertainty was applied given by 5% of the sum of the nominal Z+jets (all flavors) value and its uncertainty.

The $E_{\mathrm{T}}/p_{\mathrm{T}}$ distributions (for electrons and muons, respectively) of the four signal leptons at this stage are shown in Fig. 4.2. Figure 4.3 contains the distributions of jet multiplicity, $E_{\mathrm{T}}^{\text{miss}}$,

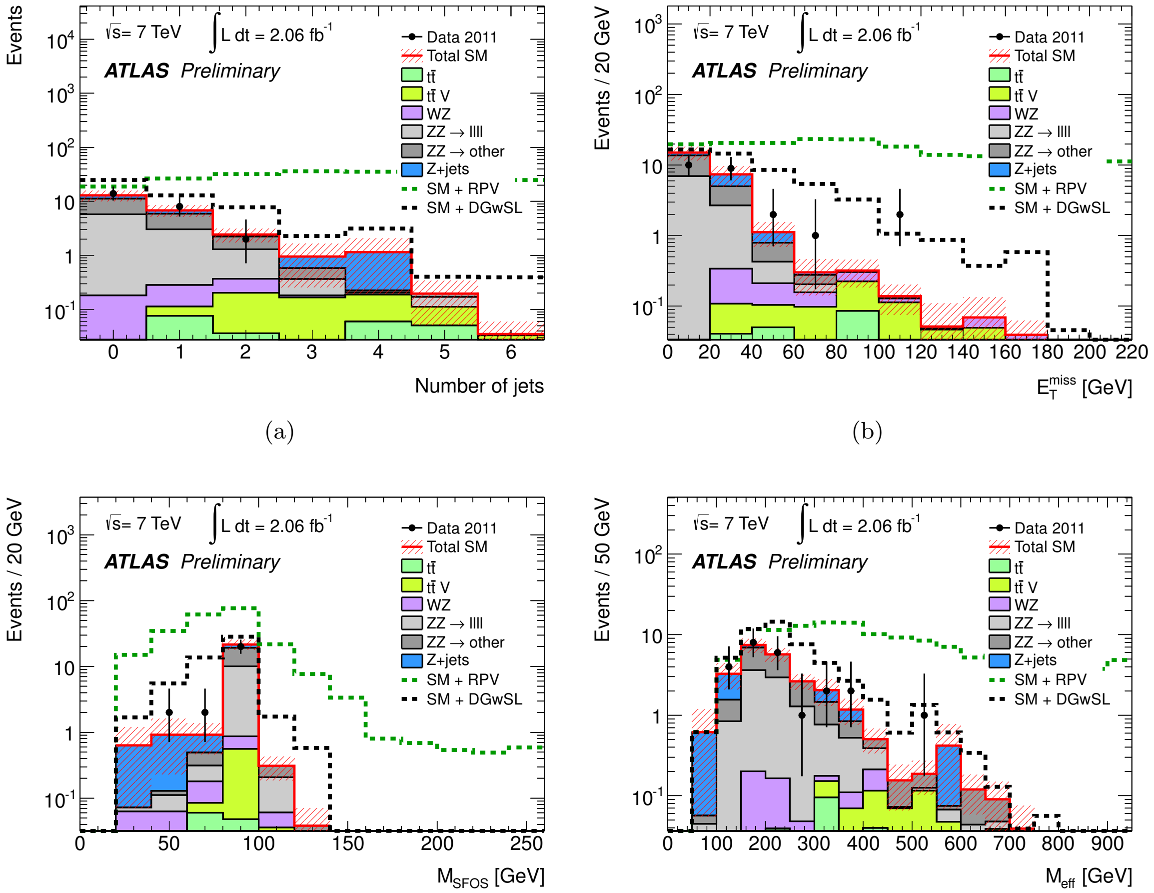

(a)

(b)

(c)

(d)

Figure 4.3: Distributions of (a) the jet multiplicity, (b) $E_{\mathrm{T}}^{\mathrm{miss}}$, (c) M_{SFOS} and (d) M_{eff} in events passing preselection and with at least four signal leptons for 2011 data and MC simulation. In events with multiple SFOS lepton pairs, the pair with invariant mass closest to the Z boson mass is plotted. M_{eff} is defined as the scalar sum of the $E_{\mathrm{T}}^{\mathrm{miss}}$, the p_{T} of the leptons and the p_{T} of jets with $p_{\mathrm{T}} > 40\,\mathrm{GeV}$ in the event. The hashed band represents statistical and systematic uncertainties added in quadrature. [41]

the invariant mass of that SFOS lepton pair in each event, which is closest to the Z mass, M_{SFOS}, and the "effective mass", M_{eff}, defined as the scalar sum of the $E_{\mathrm{T}}^{\mathrm{miss}}$, the p_{T} of the leptons and the $E_{\mathrm{T}}/p_{\mathrm{T}}$ of all jets with $p_{\mathrm{T}} > 40\,\mathrm{GeV}$ in an event. The hashed band represents the combined statistical and systematic uncertainties on the SM MC predictions. All of these distributions exhibit good overall agreement within uncertainties.

4.6 Definition of Signal Regions

Figure 4.3b shows the distribution of the missing transverse energy $E_{\mathrm{T}}^{\mathrm{miss}}$ for events with at least four signal leptons. To further suppress the components of the remaining SM backgrounds, which have little or no (real) sources of missing transverse energy, like the dominant $ZZ \to 4\ell$, a moderate $E_{\mathrm{T}}^{\mathrm{miss}}$ cut was chosen. While the expectations for the number of SM background and signal events for a variety of models similar to the two above-mentioned SUSY benchmark models were taken into account, the cut was not optimized for any one of these models.

The first signal region (SR1) was then defined by requiring events to

- pass the event preselection,
- contain ≥ 4 signal leptons and
- have $E_{\mathrm{T}}^{\mathrm{miss}} > 50\,\mathrm{GeV}$.

To further suppress Z backgrounds for models where the signal leptons are typically not expected to originate from Z decays, a second signal region (SR2), with a corresponding veto condition was defined. In SR2 events had to

- pass the event preselection,
- contain ≥ 4 signal leptons,
- have $E_{\mathrm{T}}^{\mathrm{miss}} > 50\,\mathrm{GeV}$ and
- not contain a SFOS lepton pair with $|m_{\mathrm{SFOS}} - m_Z| \leq 10\,\mathrm{GeV}$ (“Z-veto”).

In data the signal regions were initially blinded to prevent bias, that is, before actually applying these cuts to the data samples, the modeling of the SM backgrounds as well as the description of the $E_{\mathrm{T}}^{\mathrm{miss}}$ distribution and lepton isolation were validated and the sources of systematic uncertainties studied.

4.7 Background Estimation and Validation

As the small number of events left after the four signal lepton requirement was not enough to use data-driven techniques for background estimation in most cases, the predictions of the SM MC samples had to be used for this purpose. Only backgrounds with at least two expected prompt leptons (from $W/Z^{(*)}/\tau$ decays) were considered, as prior dedicated studies of W+jets MC simulation found the contribution of backgrounds with a smaller number of leptons to be negligible. In order to validate the predictions of the background model, data and MC were compared in a number of control regions, separated from the signal regions defined in Sec. 4.6, for example by inverting the $E_{\mathrm{T}}^{\mathrm{miss}}$ cut and/or by requiring one or more leptons to fail the jet overlap or isolation criteria (called “fake” leptons below).

Furthermore, the method that was used to estimate the background from internal conversions, as well as the dedicated validation of the missing transverse energy and the lepton isolation are summarized below.

4.7.1 Validation in Control Regions

Control regions aiming to enrich the contribution of the samples containing top quarks were defined by first requiring two opposite-flavor opposite-sign (OFOS) signal leptons and one b-tagged jet. The b-tagging algorithm used impact parameter and secondary vertex information as described in [79]. In one region then two or more signal leptons and $E_{\mathrm{T}}^{\mathrm{miss}} < 50\,\mathrm{GeV}$ were required, while for the other two regions two fake leptons and $E_{\mathrm{T}}^{\mathrm{miss}} > 50\,\mathrm{GeV}$ or $E_{\mathrm{T}}^{\mathrm{miss}} > 30\,\mathrm{GeV}$ were selected, respectively. For all three regions lepton pairs within $10\,\mathrm{GeV}$ of the Z mass were vetoed. The two regions with two fake leptons and higher $E_{\mathrm{T}}^{\mathrm{miss}}$ were found to be dominated by the targeted $t\bar{t}(+V)$ backgrounds, as expected.

Three regions were defined to target ZZ and Z-rich backgrounds. For the first only the $E_{\mathrm{T}}^{\mathrm{miss}}$ cut was inverted (4 signal leptons and $E_{\mathrm{T}}^{\mathrm{miss}} < 50\,\mathrm{GeV}$) and no further Z requirements were applied. For the other two regions events with two SFOS signal leptons with an invariant mass in the Z peak (as above) and either two more signal leptons and $E_{\mathrm{T}}^{\mathrm{miss}} < 50\,\mathrm{GeV}$ or two fakes and $E_{\mathrm{T}}^{\mathrm{miss}} > 50\,\mathrm{GeV}$ were selected. Both low-$E_{\mathrm{T}}^{\mathrm{miss}}$ regions were dominated by ZZ events, followed by Z+LFjets, while $t\bar{t}$ was the biggest contribution in the region with two fake leptons and higher $E_{\mathrm{T}}^{\mathrm{miss}}$.

Finally two control regions were defined focussing on events with two SFOS signal leptons in the Z peak, one additional signal lepton and one fake, as expected for example in WZ events, but also in ZZ, $Z\gamma$ and Z+jets. In one region a cut of $E_{\mathrm{T}}^{\mathrm{miss}} < 50\,\mathrm{GeV}$ was applied, while in the second case ($20\,\mathrm{GeV} < E_{\mathrm{T}}^{\mathrm{miss}} < 50\,\mathrm{GeV}$) some missing transverse energy was required to further suppress the ZZ contribution.

In all regions the total number of selected MC events were compared to the number observed in data. Where possible the comparison was repeated for separate (fake) lepton flavor (combinations). The distributions of the $E_{\mathrm{T}}/p_{\mathrm{T}}$ of the four leptons, $E_{\mathrm{T}}^{\mathrm{miss}}$, the number of jets or the invariant mass of SFOS pairs of leptons were studied as well.

Overall, good agreement between the simulated SM backgrounds and data was found, within uncertainties, in all aforementioned validation regions.

4.7.2 Background from Internal Conversions

Another possible contribution to a real four lepton final state is given by internal conversions of final state radiation photons: $Z \to \ell\ell\gamma^* \to \ell\ell\ell\ell$. As this process was not described by the MC samples used, a data-driven approach was employed to estimate its contribution in the signal regions. For this the photon conversion probability was measured outside the signal region (by inverting the $E_{\mathrm{T}}^{\mathrm{miss}}$ cut), using the ratio of events found where $M_{\ell\ell\gamma^*}$ or $M_{\ell\ell\ell\ell}$ were within $10\,\mathrm{GeV}$ of m_Z. The measured conversion rates for electrons and muons were then applied to the number of $\ell\ell\gamma$ events found in the signal region. The resulting contribution was found to be negligible, though.

Similarly, the contribution of $W \to \nu\ell\gamma^* \to \nu\ell\ell\ell$ to the signal region was estimated to be negligible by comparing it to the Z case, since the enhanced cross section for the W case is more than compensated for by the low probability to find a fake fourth lepton.

4.7.3 Missing Transverse Energy Validation

As the missing transverse energy was one of the main signal region cuts, its distribution in the SM MC samples was compared to the one observed in data for all events with at least four leptons. Additionally events with opposite-sign lepton pairs with an invariant mass within 10 GeV of the Z mass were compared as well, to test the description of $Z \to \ell^+\ell^-$ and $\ell^+\ell'^-$ (where the second case can result from τ decays). The distributions were checked separately for all lepton flavor combinations, as well as for each of the $E_{\mathrm{T}}^{\mathrm{miss}}$ components (cf. Eq. 4.1). While statistics for the flavor-separated distributions in the four lepton case was very limited, good agreement was still found within uncertainties in all cases.

4.7.4 Lepton Isolation Validation

The MC simulation of the lepton isolation, used in the definition of signal leptons, was validated using a tag-and-probe method. Events containing $W \to \ell\nu$ decays, but no b-jets, were selected in data and MC and the distributions of the values used to define the isolation (cf. Sec. 4.3.5) for electrons and muons were compared for a second opposite-flavor probe lepton, for which the isolation criterion was dropped. Within uncertainties, the comparison showed the isolation to be well modeled.

4.8 Systematic Uncertainties

In addition to an estimate of the SM backgrounds and their statistical uncertainties, the potential impact of systematic effects on this prediction was studied. While in the simplest cases the uncertainty due to, for example, a systematically shifted energy scale can be estimated by retracing all analysis steps with that scale set to another value and just comparing the resulting number of events, dedicated studies are often required to disentangle the influences of separate effects. Results of such studies were provided by the ATLAS performance groups in the form of parametrized uncertainty estimates or scaling recommendations and used to derive some of the systematic uncertainties for the four lepton analysis.

The percentages given below for the individual systematic effects studied always reflect the changes in the final number of events in the signal regions, if not explicitly stated otherwise.

The changes due to variations of the jet energy scale [80] were found to be one of the leading systematic effects at $\sim 20\,\%$ for SR1 and $\sim 50\,\%$ for SR2. The method, as recommended by the Jet/$E_{\mathrm{T}}^{\mathrm{miss}}$ Working Group, also included a p_{T}- and η-dependent uncertainty ($2\,\%$ to $7\,\%$) to account for the effect of out-of-time pileup in multi-jet environments. The jet energy resolution had an effect of comparable strength ($\sim 20\,\%$ for SR1 and $\sim 50\,\%$ for SR2). To estimate this, the p_{T} of each jet was smeared according to a Gaussian distribution with unit mean and a width given by a p_{T}- and η-dependent resolution function, further explained in [81].

The typical EES uncertainty per electron was $< 1\,\%$, but increased up to $\sim 9\,\%$ for low-p_{T} (10 GeV to 20 GeV) electrons, due to the low number of W and J/Ψ events in the study [63] of the EGamma Working Group the determination was based on. Applied to the electron objects of the four lepton analysis, the uncertainty on the EES was found to have a moderate impact of about 4 % on the resulting number of events in both signal regions, while the EER uncertainty had large effects of about 20 % for SR1 and $\sim 50\,\%$ for SR2.

The impact of varying the electron identification and reconstruction efficiency, used to correct the observed difference between data and MC, as described in Sec. 4.4.4, was studied by the EGamma Working Group in W and Z events and found to be between about 0.6 % and 1.8 % per electron (η- and E_{T}-dependent), rising to $\sim 10\,\%$ for electrons with $E_{\mathrm{T}} < 20\,\mathrm{GeV}$. Propagated to the final number of events, this translated into a moderate systematic uncertainty of $\sim 5\,\%$ for SR1 and $\sim 10\,\%$ for SR2.

Systematic uncertainties related to smearing and shifting the muon p_{T}, described in Sec. 4.3.2, were calculated using tools provided by the Muon Combined Performance Group, based on [66]. This was done separately for the inner detector and spectrometer tracks in both combined and segment-tagged muons. The effects on the resulting number of events for the four lepton analysis was found to be very small ($< 1\,\%$ in both signal regions).

The uncertainty in the muon reconstruction efficiency, provided by the Muon Combined Performance Group as a function of the muon momentum, only had a very small impact on the number of SM background events ($< 1\,\%$ in both signal regions).

The systematic uncertainty of the lepton isolation efficiency was found to have a negligible effect only.

As already mentioned, the jet and lepton systematic uncertainties described above were applied to the related objects in the event. Additionally, they were also propagated to the respective components of the $E_{\mathrm{T}}^{\mathrm{miss}}$. The uncertainty due to the $E_{\mathrm{T}}^{\mathrm{miss}}$ term summing up the contribution of calorimeter clusters not associated to reconstructed objects ($E_{x/y}^{\mathrm{miss,cl}}$ in Eq. 4.1) were studied by smearing the energy scale and resolution of the calorimeter clusters, but its effect was negligible for all SM samples studied.

The systematic uncertainty caused by the MC trigger reweighting procedure given in Sec. 4.4.1, found by propagating the uncertainties of the determined weights, was of negligible size as well.

The systematic uncertainty caused by the MC event reweighting used to account for the effects of multiple pp collisions (cf. Sec. 4.4.5) was assessed by comparing the results of the nominal pileup distribution, which best described the effects of out-of-time pileup, with a distribution better describing the in-time pileup (by not averaging across neighboring bunches). The impact on the number of SM background events was small ($\sim 1\,\%$).

To estimate the uncertainty due to the MC modeling of the local readout problem in the LAr calorimeter, present during part of the data-taking (cf. Sec. 4.4.1), the 40 GeV p_{T} threshold of the jets used for the event rejection was varied by 20 % in MC. The resulting uncertainty was about 1 % in SR1 and even less in SR2.

To estimate the systematic uncertainty of the fake rate of leptons from heavy flavor decays, the fake rate in $b\bar{b}$-enriched events was compared between data and MC using a tag-and-probe method. Agreement was found to be within 10 % and the same percentage was applied to the $t\bar{t}$, single top, $t\bar{t}V$ and Z+(c,b jets) MC samples as a additional systematic uncertainty. This amounted to systematic uncertainties of $\sim 3\,\%$ for SR1 and $\sim 1\,\%$ for SR2.

The uncertainty of the integrated luminosity for the 2011 dataset was determined to be 3.7 % in [14, 15].

The uncertainties applied to the theoretical fiducial cross sections were 5 % for the ZZ, WW, Z+(u,d,s jets) and Drell–Yan samples [45, 57], 7 % for the WZ samples [45], $^{+7.0}_{-9.6}$ % for the $t\bar{t}$ samples [49, 82], 7 % for the single top samples [51, 52] and 40 % for the $t\bar{t}V$ samples [54]. For the Z+(c,b jets) samples the uncertainty for the cross sections given in [58] was 30 %–40 %. As this uncertainty depended on the event topology of the analysis, though, a conservative uncertainty of 100 % was applied for these samples in the four lepton analysis. The effect of these uncertainties on the predicted number of SM background events was $\sim$ 12 % for SR1 and $\sim$ 6 % for SR2.

The effect of varying the parton distribution functions used for the MC simulation process was calculated with the full eigenset provided by the CTEQ collaboration for the CTEQ6.6 PDFs as used for samples generated with MC@NLO, while the full eigenset of the MSTW08LO PDFs was used for the Herwig samples. Since the $t\bar{t}V$ and Alpgen samples were generated with the PDF set CTEQ6L1 for which no PDF error sets were available, no PDF uncertainty was applied. The resulting effect on the number of SM events was $\sim$ 5 % for SR1 and $\sim$ 3 % for SR2.

To estimate the uncertainties due to different choices of the factorization/renormalization scale uncertainty for $t\bar{t}$, the yield from a $t\bar{t}$ sample generated with a different combination of MC generator and shower simulation, PowHeg [83] and Pythia, was compared to the nominal MC@NLO sample. Fluctuations of 46 % were seen within the small statistics available. As the 40 % uncertainty on the $t\bar{t}V$ cross section mentioned above already included the effect of such scale variations, no extra scale uncertainty was applied. Based on [84], the scale variations used for the ZZ, WZ and WW samples were 15 %, 16 % and 20 %, respectively. For all other backgrounds no scale uncertainties were applied since their contributions were either very small or currently known only with more than 100 % uncertainty. Applying the factorization/renormalization scale uncertainties had $\sim$ 6 % and $\sim$ 9 % effects on the SM background estimation in SR1 and SR2, respectively.

With a four lepton requirement, not enough MC statistics was available to conclusively study the systematic uncertainty caused by varying the amount of initial and final state radiation. Similar studies requiring only three leptons found the variation across the same MC samples to be < 10 %. Since these effects were not expected to have a dominant contribution, no systematic uncertainties were applied to account for them.

The large systematic effects seen for the jet energy scale and resolution as well as the electron energy resolution were caused by the fact that only one event remained of the Z+(u,d,s jets) MC samples after applying the selection criteria. To account for the possibility of one event fluctuating in or out of the selection a 100 % uncertainty was applied, making this the dominant contribution to the total systematic uncertainty on the MC background estimation in both signal regions.

A summary of the expected number of SM background events, the absolute statistical uncertainty on the MC samples and all non-negligible systematic uncertainties is shown in Tab. 4.6 for both signal regions. In cases where varying the input within its (usually $\pm 1\sigma$) extremes resulted in asymmetric uncertainties, the largest value was applied as a symmetric systematic

	SR1	SR2
Expected Events	1.70	0.66
MC statistics	0.59	0.57
Jet Energy Scale	0.35	0.34
Jet Energy Resolution	0.34	0.34
Electron Energy Scale	0.07	0.03
Electron Energy Resolution	0.34	0.34
Muon Inner Detector Track p Resolution	0.01	0.00
Muon Spectrometer Track p Resolution	0.01	0.00
Electron Identification/Reconstruction Efficiency	0.09	0.07
Muon Identification/Reconstruction Efficiency	0.01	0.00
Multiple pp collisions (Pileup)	0.02	0.01
LAr readout problem	0.02	0.00
PDF	0.08	0.02
Factorization/Renormalization scale	0.11	0.06
Cross section	0.20	0.04
Luminosity	0.06	0.02
Heavy flavor lepton fake rate	0.05	0.01
TOTAL systematic uncertainty	0.88	0.82

Table 4.6: Summary of the effect of systematic uncertainties on the background estimation for SR1 and SR2, normalized to $2.06\,\mathrm{fb}^{-1}$ of data. The expected numbers of events are listed, followed by the absolute MC statistical and the individual systematic uncertainties. Adapted from [41].

uncertainty. When calculating the total systematic uncertainty on the background estimation, the individual sources of uncertainty were assumed to be uncorrelated.

Selection	$\geq 4\ell$	$E_{\mathrm{T}}^{\mathrm{miss}} > 50\,\mathrm{GeV}$ (SR1)	Z-veto (SR2)
$t\bar{t}$	0.22 ± 0.15	0.17 ± 0.14	0.13 ± 0.11
Single t	0 ± 0.04	0 ± 0.04	0 ± 0.04
$t\bar{t}V$	0.59 ± 0.26	0.48 ± 0.21	0.07 ± 0.04
ZZ	19 ± 5	0.44 ± 0.19	0.019 ± 0.020
WZ	0.54 ± 0.17	0.25 ± 0.10	0.09 ± 0.05
WW	0 ± 0.015	0 ± 0.015	0 ± 0.015
$Z\gamma$	0 ± 0.5	0 ± 0.5	0 ± 0.5
Z+LFjets	3.8 ± 1.6	0.33 ± 0.67	0.33 ± 0.67
Z+HFjets	0.26 ± 0.28	0.024 ± 0.035	0.024 ± 0.035
Drell–Yan	0 ± 0.29	0 ± 0.05	0 ± 0.05
$\sum$ SM	25 ± 5	1.7 ± 0.9	0.7 ± 0.8
Data	24	4	0

Table 4.7: Summary of the numbers of SM MC and data events for different stages of the analysis. The uncertainties given are statistical and systematic, added in quadrature. All numbers are normalized to $2.06\,\mathrm{fb}^{-1}$.

4.9 Upper Limits on the Visible Cross Section

After all analysis cuts were decided on and the systematic uncertainties were estimated, the signal regions were unblinded. For $2.06\,\mathrm{fb}^{-1}$ at $7\,\mathrm{TeV}$ a total of 1.7 ± 0.9 events were predicted by the SM MC for the signal region with four or more signal leptons and more than $50\,\mathrm{GeV}$ of missing transverse energy (SR1), while four events were found in the analyzed ATLAS dataset. For the signal region with an additional Z-veto (SR2) 0.7 ± 0.8 events were predicted and none were observed. These numbers, with their combined statistical and systematic uncertainties, are summarized in Tab. 4.7, where the results at the four lepton stage and the individual SM contributions are given as well. Detailed numbers for the different lepton-flavor combinations in the two signal regions are given in Tab. 4.8.

Using a frequentist method based on a profile likelihood ratio, which will be further explained in Sec. 5.5, the total numbers of expected and observed events were used to derive upper limits ($95\,\%$, CL_s) on the number of events predicted by new physics models to still be compatible with this measurement. This can also be expressed in terms of the “visible” cross section, which here is defined as the product of cross section, branching ratio, acceptance and efficiency (i.e. without unfolding geometric, kinematic or detector effects), which was deduced from the number of events simply as $\sigma_{\text{vis}} = n \cdot (\int \mathcal{L}\,\mathrm{d}t)^{-1}$. Table 4.9 shows the expected and observed limits, the former based on the SM MC prediction and its uncertainties only, the latter making use of the measured values.

An interpretation of these limits in terms of concrete (SUSY) models was left to follow-up studies. The case of the BC1 scenario and the surrounding $m_{1/2}$–$\tan\beta$ parameter space will be the topic of the following chapter.

SR1	All	*eeee*	$eee\mu$	$ee\mu\mu$	$e\mu\mu\mu$	$\mu\mu\mu\mu$
$t\bar{t}$	0.17 ± 0.14	0.011 ± 0.042	0.027 ± 0.042	0.09 ± 0.06	0.05 ± 0.07	0 ± 0.018
Single t	0 ± 0.04	0 ± 0.04	0 ± 0.04	0 ± 0.04	0 ± 0.04	0 ± 0.04
$t\bar{t}V$	0.48 ± 0.21	0.072 ± 0.037	0.12 ± 0.06	0.14 ± 0.07	0.08 ± 0.04	0.059 ± 0.032
ZZ	0.44 ± 0.19	0.14 ± 0.08	0.016 ± 0.012	0.21 ± 0.12	0.047 ± 0.032	0.025 ± 0.045
WZ	0.25 ± 0.10	0.015 ± 0.022	0.07 ± 0.04	0.050 ± 0.032	0.11 ± 0.06	0 ± 0.011
WW	0 ± 0.015	0 ± 0.015	0 ± 0.015	0 ± 0.015	0 ± 0.015	0 ± 0.015
$Z\gamma$	0 ± 0.5	0 ± 0.5	0 ± 0.5	0 ± 0.5	0 ± 0.5	0 ± 0.5
Z+LFjets	0.33 ± 0.67	0.33 ± 0.67	0 ± 0.29	0 ± 0.29	0 ± 0.29	0 ± 0.29
Z+HFjets	0.024 ± 0.035	0 ± 0.17	0 ± 0.17	0 ± 0.17	0.024 ± 0.035	0 ± 0.17
Drell–Yan	0 ± 0.05	0 ± 0.05	0 ± 0.017	0 ± 0.017	0 ± 0.016	0 ± 0.017
$\sum$ SM	1.7 ± 0.9	0.6 ± 0.8	0.24 ± 0.57	0.5 ± 0.6	0.32 ± 0.55	0.08 ± 0.57
Data	4	0	1	2	0	1

SR2	All	*eeee*	$eee\mu$	$ee\mu\mu$	$e\mu\mu\mu$	$\mu\mu\mu\mu$
$t\bar{t}$	0.13 ± 0.11	0 ± 0.018	0.027 ± 0.042	0.05 ± 0.04	0.05 ± 0.07	0 ± 0.018
Single t	0 ± 0.04	0 ± 0.04	0 ± 0.04	0 ± 0.04	0 ± 0.04	0 ± 0.04
$t\bar{t}V$	0.07 ± 0.04	0.007 ± 0.007	0.024 ± 0.017	0.022 ± 0.021	0.011 ± 0.008	0.005 ± 0.005
ZZ	0.019 ± 0.020	0.008 ± 0.011	0 ± 0.012	0.010 ± 0.018	0 ± 0.012	0 ± 0.012
WZ	0.09 ± 0.05	0 ± 0.020	0.0021 ± 0.0024	0.050 ± 0.032	0.039 ± 0.028	0 ± 0.011
WW	0 ± 0.015	0 ± 0.015	0 ± 0.015	0 ± 0.015	0 ± 0.015	0 ± 0.015
$Z\gamma$	0 ± 0.5	0 ± 0.5	0 ± 0.5	0 ± 0.5	0 ± 0.5	0 ± 0.5
Z+LFjets	0.33 ± 0.67	0.33 ± 0.67	0 ± 0.29	0 ± 0.29	0 ± 0.29	0 ± 0.29
Z+HFjets	0.024 ± 0.035	0 ± 0.17	0 ± 0.17	0 ± 0.17	0.024 ± 0.035	0 ± 0.17
Drell–Yan	0 ± 0.05	0 ± 0.05	0 ± 0.017	0 ± 0.017	0 ± 0.016	0 ± 0.017
$\sum$ SM	0.7 ± 0.8	0.35 ± 0.83	0.05 ± 0.57	0.13 ± 0.57	0.12 ± 0.55	0.005 ± 0.567
Data	0	0	0	0	0	0

Table 4.8: Total and flavor-separated expected SM MC background and observed data for SR1 and SR2. Adapted from [42].

		SR1	SR2
Expected number of SM events predicted by MC		1.7 ± 0.9	0.7 ± 0.8
Observed number of events in data		4	0
Expected	upper limit on number of predicted signal events	4.3	3.0
Observed		7.1	3.0
Expected	upper limit on visible cross section [fb]	2.09	1.46
Observed		3.45	1.46
CL_b		0.07	0.78

Table 4.9: Summary of the ATLAS four lepton analysis results for 2.06 fb^{-1} at 7 TeV and upper limits derived from them.

CHAPTER 5

Interpretation

Going beyond the general result summarized in the previous chapter, the four lepton analysis strategy can now be applied to the BC1 model introduced in Sec. 3.2.8 as well as to models in the surrounding $m_{1/2}$–$\tan\beta$ parameter plane, which have a very similar phenomenology.

The production chain used to generate simulated events for such models will be summarized in Sec. 5.1. Following that, theoretical and experimental constraints for the placement of model points in the parameter plane will be discussed in Sec. 5.2. Phenomenological properties of the models, like sparticle masses, production cross sections, branching ratios, life times and decays will be presented in Sec. 5.3 to point out important or interesting features found in some regions of the parameter space. The results of applying the four lepton analysis strategy to these models will be summarized in Sec. 5.4. Finally Sec. 5.5 will explain the statistical method used to derive limits and present the expected and observed limits on the BC1-like scenarios discussed here.

5.1 MC Production Chain for Simulated Signal Events

Simulated events are generated for a grid of model points in the $m_{1/2}$–$\tan\beta$ plane to study the model phenomenology at generator level and include a simulation of the ATLAS detector response for the full analysis. The mass spectrum, couplings and mixing matrices for each point are derived from the GUT scale model parameters using SOFTSUSY 3.2.4 [85]. ISAJET 7.64 [86] and ISAWIG 1.200 are used to provide decay rates and an interface to the event generator Herwig 6.52 [43].

This emulates the setup which was used in the original work defining BC1 [37], as well as in [38] and [40], including the modifications to Herwig, which allow the generator to model the $\not{R}_p$ four-body decays of the $\tilde{\tau}_1$ LSP. As early studies using the four lepton analysis strategy indicated that an improved reach could be expected with the available integrated luminosity, compared to the results of the references above, a new and extended grid of models was defined

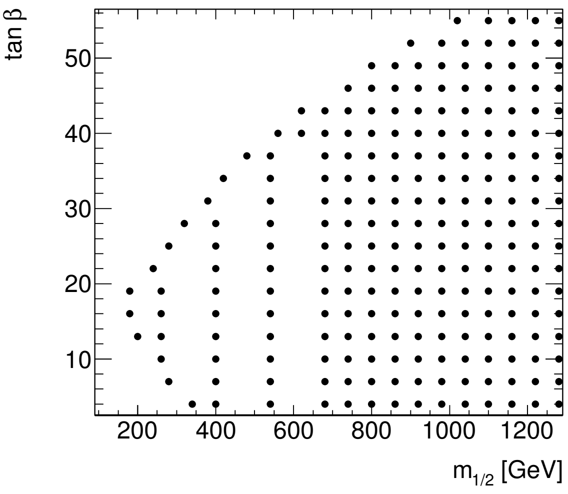

Figure 5.1: Positions of the generated model points.

and studied for this thesis. The newer version of SOFTSUSY was used to take advantage of a number of corrections to the spectrum generator code[1].

For each of the 224 chosen points 5000 events were generated. Their positions in the parameter plane are shown in Fig. 5.1. The points have a general spacing of 60 GeV in $m_{1/2}$ and 3 in $\tan\beta$. Due to limited computing resources and the expected increase in reach, the $m_{1/2}$-spacing was increased for $m_{1/2} < 680$ GeV, after testing that no irregularities were to be expected for models inside the area.

Furthermore the fast detector simulation AtlFast-II [88] had to be used instead of the full simulation as employed for the SM background MC. While the full GEANT4 simulation is still used for the inner detector and the muon system in this fast simulation, the full development of particle showers within the calorimeter is replaced by a parametrized treatment of the shower properties, tuned to provide a good description of each reconstructed object's key features. As a cross-check additional events using the full detector simulation were generated for a small subset of points from different areas of the parameter plane. A comparison of the properties of the reconstructed objects used for the analysis and of the selected event numbers showed good agreement within their respective uncertainties.

In addition to these officially created events, generator-level information was produced for further points with a smaller $m_{1/2}$-spacing, where necessary to define the boundaries discussed below and to allow further studies of general model properties.

---

[1] Table 3.4 already uses these numbers for BC1 instead of the original ones given in [37] or [87].

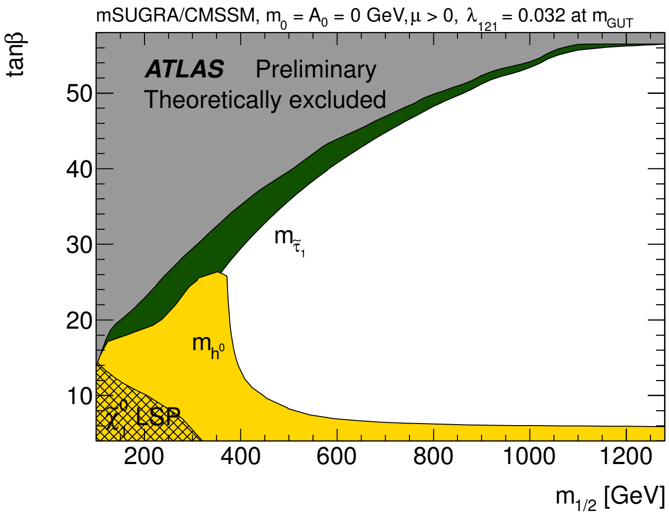

Figure 5.2: Constraints for BC1-like models. The shaded regions include a theoretically forbidden region producing tachyons, a region with a $\tilde{\chi}_1^0$ LSP, a region excluded by LEP Higgs bounds and a region with $m_{\tilde{\tau}_1}$ below the 80 GeV threshold considered in this analysis. [87]

5.2 Theoretical and Experimental Constraints

Figure 5.2 contains four shaded regions in the $m_{1/2}$–$\tan\beta$ plane, defined by theoretical or experimental constraints for BC1-like mSUGRA models ($m_0 = A_0 = 0\,\text{GeV}$, $\mu > 0$ and $\lambda_{121} = 0.032$ at M_{GUT}), which were taken into account when defining the grid of model points and also included for the interpretation of the results of the four lepton analysis.

The upper left (grey) region is theoretically excluded, as the resulting models contain tachyons, rendering these theories unstable. In the hatched region at low $m_{1/2}$ and $\tan\beta$, the LSP is the lightest neutralino instead of the $\tilde{\tau}_1$ targeted in this interpretation[2]. Both of these define outer bounds for the grid of model points.

For the final interpretation, two additional areas are excluded. The first is the (green-shaded) area, where the mass of the $\tilde{\tau}_1$-LSP is below 80 GeV. This is motivated by lower limits on the $\tilde{\tau}_1$ mass, found in direct searches for R-parity conserving and violating decays of the $\tilde{\tau}_1$ at LEP, as summarized in [18].

The second (yellow-shaded) area is given by the LEP experiments' lower limits on the mass of the lightest CP-even Higgs boson. In [37] a constraint of $m_h > 111.4\,\text{GeV}$ was directly applied to the Higgs mass computed for each model[3], which is shown in Fig. 5.3. For this interpretation the excluded area is determined in a more accurate procedure, using FeynHiggs 2.8.6 [89] and HiggsBounds 3.6.1beta [90].

For each point the full model information in the form of an SLHA [91, 92] file is passed on to FeynHiggs, which for the given model computes the decays of the Higgs bosons, as well as

---

[2] In principle, though, the $\tilde{\chi}_1^0$ LSP will also lead to four lepton final states via the $\not{R}_p$ three-body decay $\tilde{\chi}_1^0 \to \ell(\tilde{\ell})^* \to \ell\ell\nu$ (similar to Fig. 3.14 but with the $\tilde{\chi}_1^0$ on-shell).

[3] The actual LEP limit of 114.4 GeV at 95 % CL was lowered by 3 GeV to cover SOFTSUSY's uncertainty on the prediction of the mass.

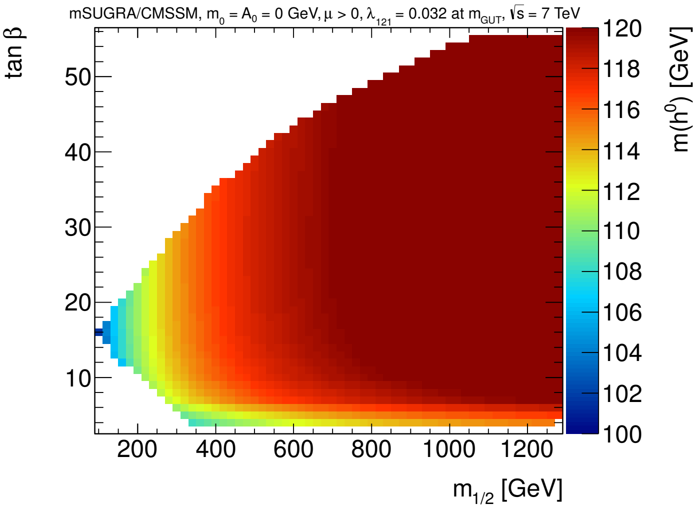

Figure 5.3: Mass of the lightest Higgs boson.

their effective couplings squared to bosons and fermions. While the determination of the Higgs boson masses in FeynHiggs includes more higher-order effects than the one that was used in SOFTSUSY, the former does not include $\not{R}_p$ effects. With only about 1 GeV in the region of interest and at most about 3 GeV at the high-$m_{1/2}$–$\tan\beta$ border of the grid, the difference in m_h is well within typical theoretical uncertainties, though.

The combined information is then passed on to HiggsBounds, which uses them to compute the ratios between studied model and SM cross sections and branching ratios. Out of all analysis results incorporated into HiggsBounds, the one with the highest statistical sensitivity for the studied model is determined. The observed limits of that analysis are then used to decide whether the studied model is excluded at 95 % confidence level. Following the publication defining the benchmark point, only LEP results are used to define the excluded region.

The discovery of a Higgs boson with a mass of about 126 GeV a posteriori excludes the models presented here. They are nevertheless a valuable benchmark for R-parity violating models with non-$\tilde{\chi}_1^0$ LSPs and multiple leptons and $E_{\mathrm{T}}^{\mathrm{miss}}$ in the final state, which are not limited to the very restrictive no-scale mSUGRA boundary conditions at the high scale, which the BC1-like models are derived from.

5.3 Model Properties in the Parameter Plane

To give an impression of the changes to some model properties as $m_{1/2}$ and $\tan\beta$ are varied in the parameter plane, a number of phenomenological details are presented in this section. Where color gradients are shown in the figures, they are based on linear interpolations between the values available at the simulated grid points. For logarithmic plots this interpolation is done on the log-values to reduce interpolation artifacts in areas where the changes in the plotted parameter are very big.

5.3.1 Sparticle Masses

Figures 5.4 and 5.5 show the masses of the squarks across the plane, Figs. 5.6, 5.7 those of the sleptons.

While the soft-breaking mass terms for all SM fermion partners start out with $m_0 = 0\,\mathrm{GeV}$ at M_{GUT}, they receive positive corrections from the soft-breaking mass terms of all gauginos they couple to in the RG evolution down to the SUSY/weak scale[4], analog to the example shown in Fig. 3.5. This effect is clearly visible in the figures, where squark and slepton masses can be seen to increase with $m_{1/2}$. As squarks have color charge, the M_3 contribution makes them heavier than the sleptons. Similarly the $SU(2)_L$ doublets are generally heavier than the singlets, because of the additional M_2 contribution.

The third family squarks and sleptons are generally lighter than those of the first two, with the $\tilde{t}_1$ as the lightest squark and the $\tilde{\tau}_1$ as the lightest slepton. This is expected, since the scalars' masses receive a negative contribution proportional to the corresponding Yukawa couplings, which are biggest for the SUSY partners of the top, bottom and tau. Another effect visible for the third family sfermions is the $\tan\beta$ dependence of the mass eigenstates, which has a small impact only for the heavy stops and sbottoms, but is a dominant effect for the LSP in these BC1-like models, as can be seen in Fig. 5.7c.

The masses of the gluino and those of the neutralinos and charginos are displayed in Figs. 5.8 and 5.9, respectively. Starting from the same $m_{1/2}$, their RG evolution is determined by the same coefficients found in Eq. 3.17.

Due to the different sign of their coefficients the gluino becomes heavy at the SUSY/weak scale, while the bino and wino become lighter. For the models discussed here the gluino becomes the heaviest particle in the spectrum, as seen in the figure. The $\tilde{\chi}_1^0$ is almost purely bino in this part of parameter space and, as mentioned before, one of the four lightest supersymmetric particles, together with the $\tilde{e}_{\mathrm{R}}$, $\tilde{\mu}_{\mathrm{R}}$ and the $\tilde{\tau}_1$.

---

[4] The full RGEs for the soft-breaking terms are given in [32].

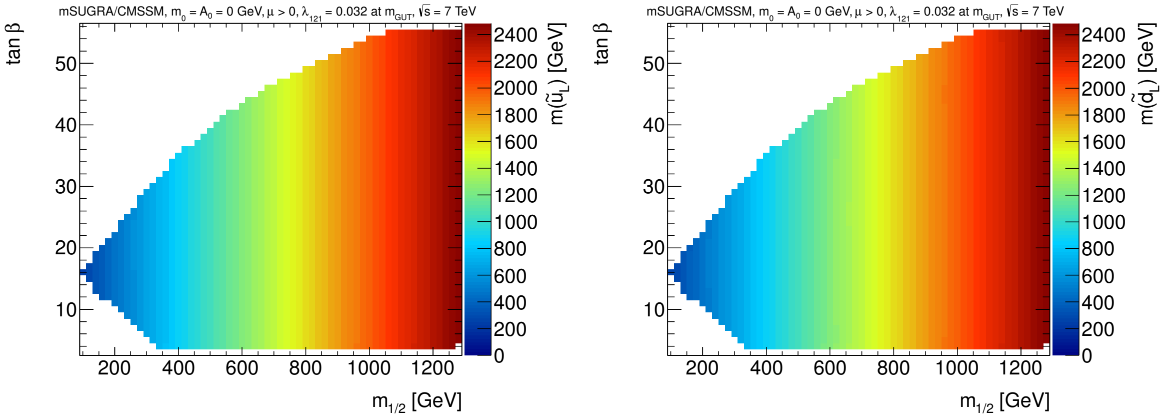

(a) $\tilde{u}_L$ mass (b) $\tilde{d}_L$ mass

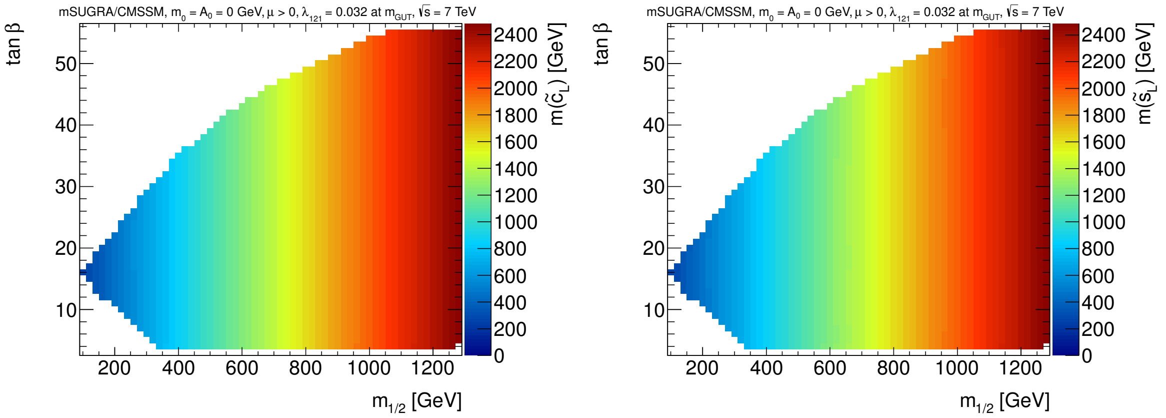

(c) $\tilde{c}_L$ mass (d) $\tilde{s}_L$ mass

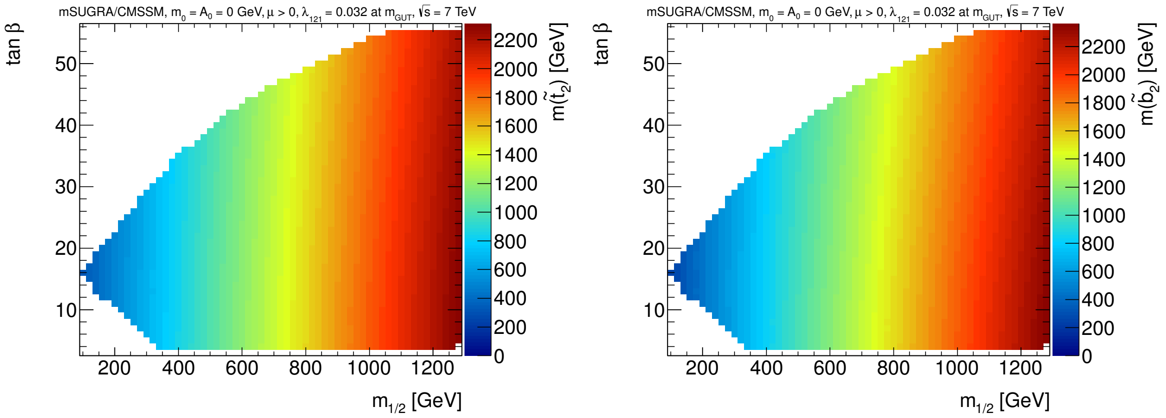

(e) $\tilde{t}_2$ mass (f) $\tilde{b}_2$ mass

Figure 5.4: Masses of the $\tilde{q}_{L/2}$.

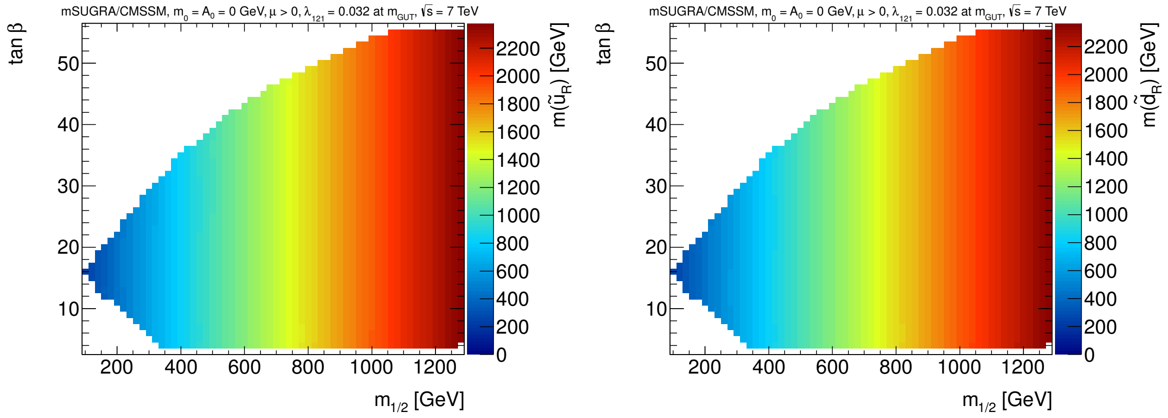

(a) $\tilde{u}_R$ mass (b) $\tilde{d}_R$ mass

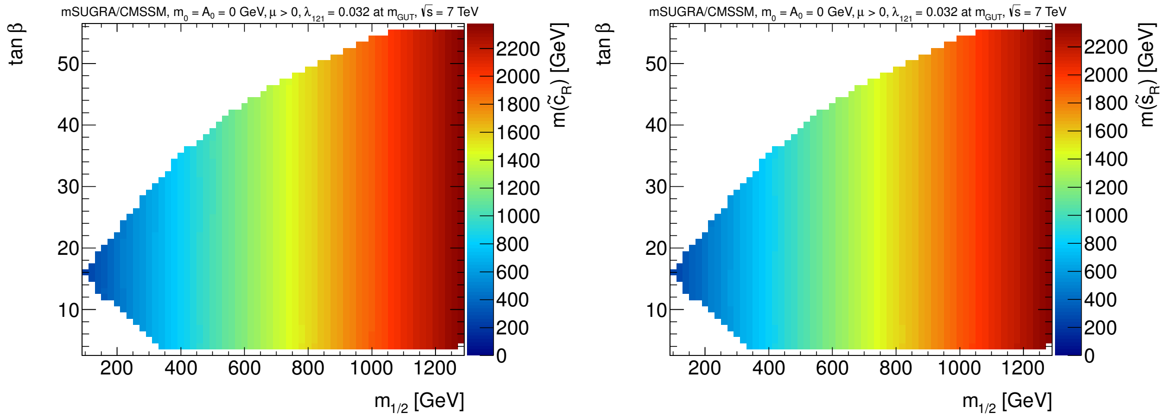

(c) $\tilde{c}_R$ mass (d) $\tilde{s}_R$ mass

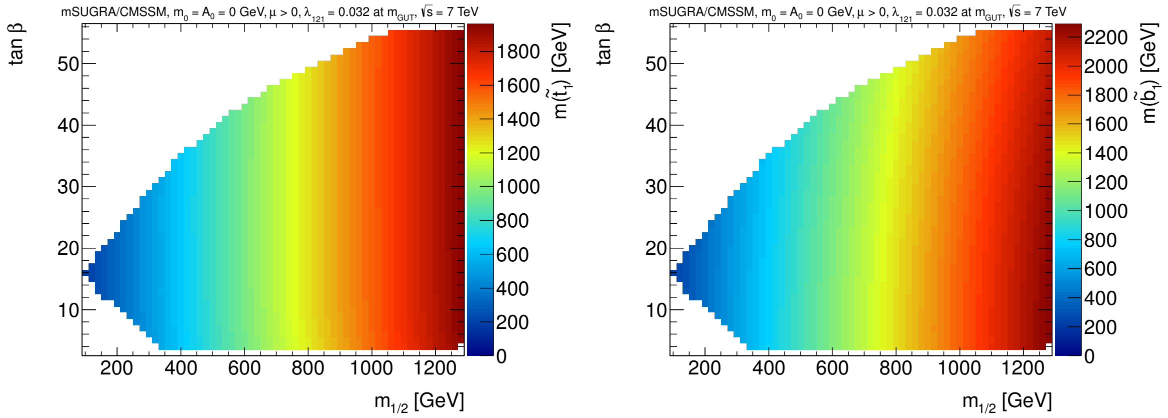

(e) $\tilde{t}_1$ mass (f) $\tilde{b}_1$ mass

Figure 5.5: Masses of the $\tilde{q}_{R/1}$.

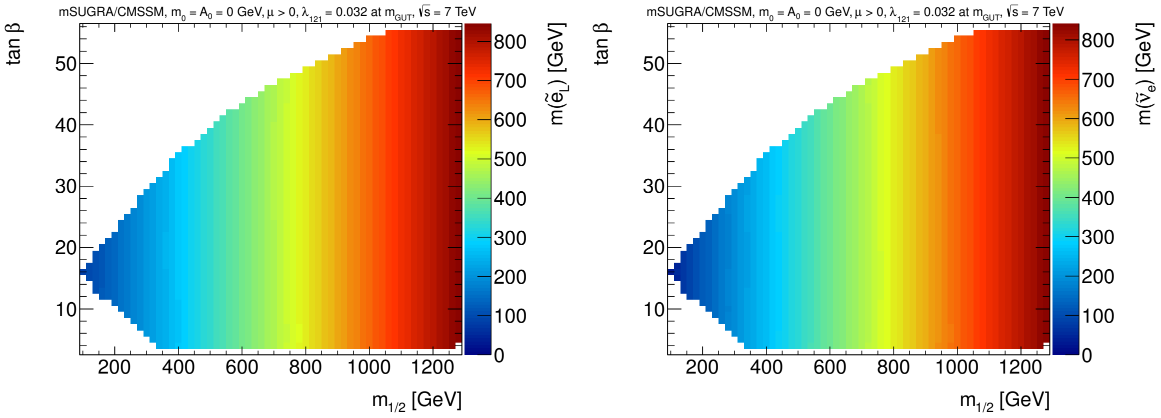

(a) $\tilde{e}_\mathrm{L}$ mass

(b) $\tilde{\nu}_e$ mass

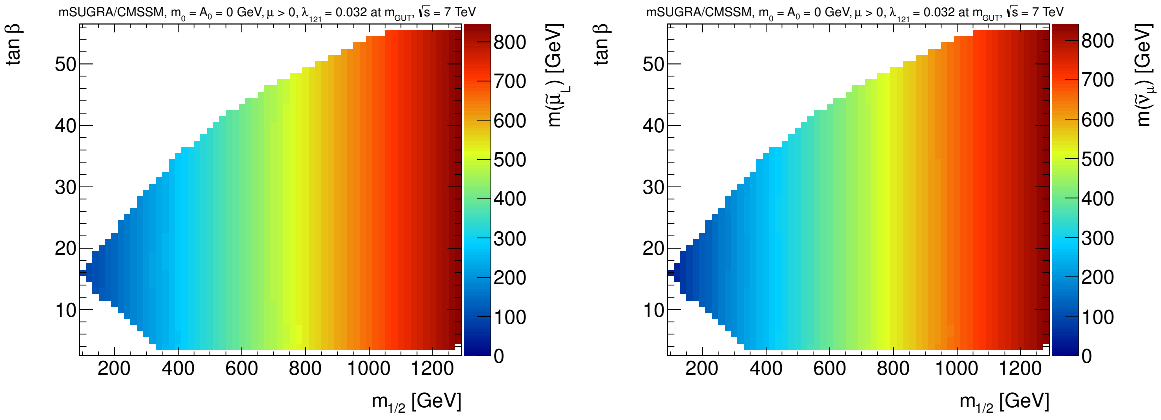

(c) $\tilde{\mu}_\mathrm{L}$ mass

(d) $\tilde{\nu}_\mu$ mass

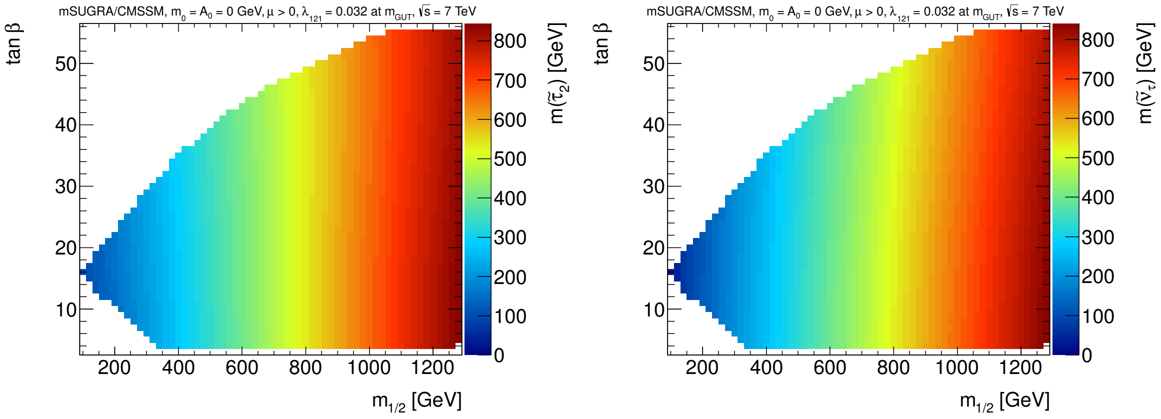

(e) $\tilde{\tau}_2$ mass

(f) $\tilde{\nu}_\tau$ mass

Figure 5.6: Masses of the $\tilde{\ell}_{L/2}$ and the sneutrinos.

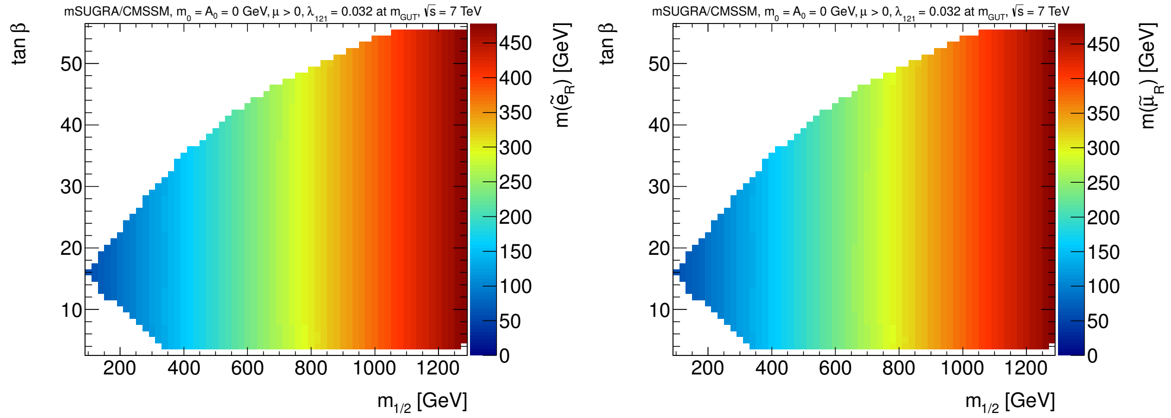

(a) $\tilde{e}_\mathrm{R}$ mass

(b) $\tilde{\mu}_\mathrm{R}$ mass

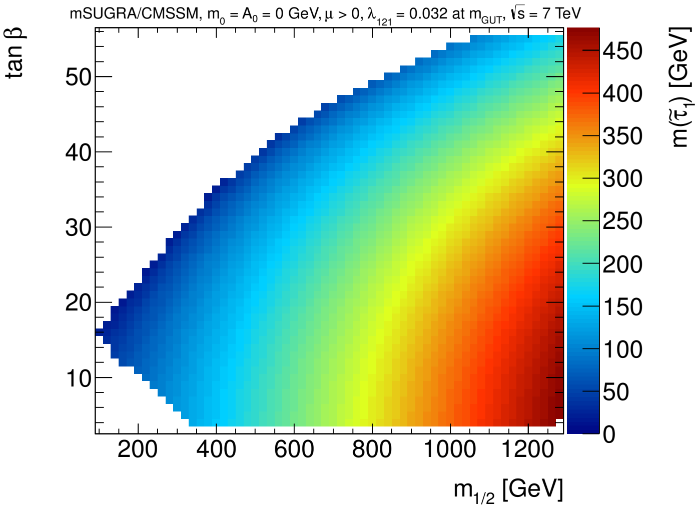

(c) $\tilde{\tau}_1$ mass

Figure 5.7: Masses of the $\tilde{e}_\mathrm{R}$, $\tilde{\mu}_\mathrm{R}$ and the $\tilde{\tau}_1$ LSP.

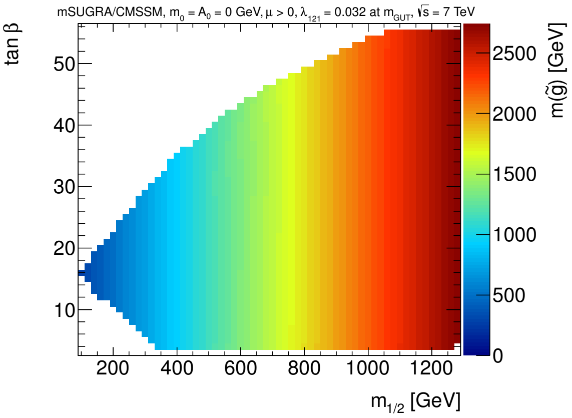

(a) $\tilde{g}$ mass

Figure 5.8: Mass of the gluino.

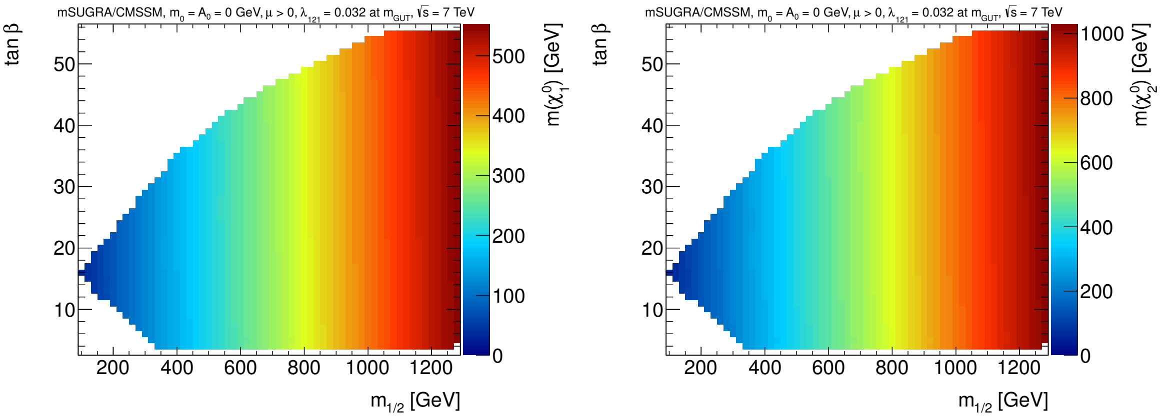

(a) $\tilde{\chi}_1^0$ mass

(b) $\tilde{\chi}_2^0$ mass

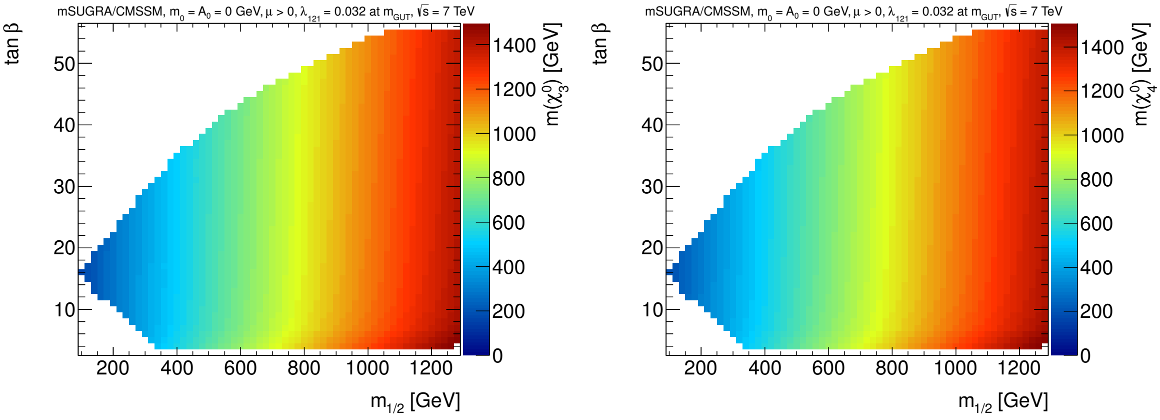

(c) $\tilde{\chi}_3^0$ mass

(d) $\tilde{\chi}_4^0$ mass

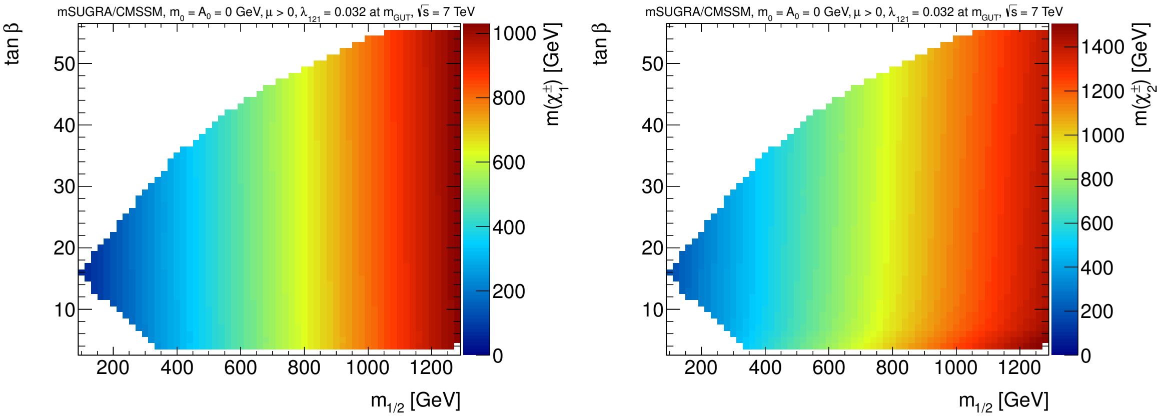

(e) $\tilde{\chi}_1^{\pm}$ mass

(f) $\tilde{\chi}_2^{\pm}$ mass

Figure 5.9: Masses of the neutralinos and charginos.

5.3.2 Production Cross Sections

The mass spectrum discussed above has a big influence on the total production cross section as well as on which combination of sparticles is dominantly produced in the hard interaction as will be shown below.

Production cross sections beyond the LO estimates of Herwig are computed for 65 different combinations of sparticles produced in the hard interaction, using Prospino 2.1 [93] and NLL-fast 1.2 [94]. These combinations are: $\tilde{q}\tilde{q}$, $\tilde{q}\tilde{g}$, $\tilde{g}\tilde{g}$, $\tilde{q}\tilde{q}^*$, $\tilde{t}\tilde{t}^*$ (2), $\tilde{\chi}\tilde{g}$ (8), $\tilde{\chi}\tilde{q}$ (8), $\tilde{\chi}\tilde{\chi}$ (30) and $\tilde{\ell}/\tilde{\nu}$ – $\tilde{\ell}/\tilde{\nu}$ (13). Here the left- and right-handed first and second family as well as bottom squarks are treated as mass-degenerate in the calculation of NLO/LO cross section K-factors, using the average of their masses as the squark mass. For the production of stop pairs the mass average does not include the sbottoms. The NLO cross sections then are the product of theses K-factors and the LO prediction, where Prospino does treat the squarks separately.

While Prospino provides NLO accuracy in SUSY QCD for all combinations, for some processes NLL-fast adds analytic corrections of next-to-leading-logarithmic (NLL) accuracy from the resummation of soft gluon emissions, matched to Prospino's NLO result, in the form of pre-computed look-up tables. These NLL results were available for strong production of squarks and gluinos with masses between 200 GeV and 2 TeV or in the case of direct stop-pair production between 100 GeV and 1 TeV. Additional numbers were available for squark masses up to 3.5 TeV for squark–gluino and 4.5 TeV for gluino–gluino production.

As in the case of the SM MC samples, the predicted cross sections and their "theory" uncertainties also depend on the choice of the set of parton distribution functions, factorization and renormalization scales, as well as the α_S uncertainty.

To test the influence of using different PDFs and the associated uncertainties on their fit parameters, the CTEQ6.6M [95] and the MSTW2008NLO [23] PDF sets are used. They each include a nominal set and a number of variations (e.g. 44 for the CTEQ set), where the values of the fit parameters are modified within their uncertainties in a consistent way. For the effect of a different value of α_S a second PDF set with a varied value of α_S, included with the CTEQ sets, is used.

The factorization and renormalization scales are simultaneously varied between their nominal value, set to the average of the two initially produced sparticles' masses, half and twice that value.

Then for each of the selected points in the $m_{1/2}$–$\tan\beta$ plane and each of the production processes the cross section is computed (or interpolated from fast lookup tables in the case of NLL-fast) for all of the mentioned variations. As the difference between the nominal values of the two PDF sets can be as big as the one resulting from their individual uncertainties, the results for both sets are used to define a common envelope. This envelope is given by the maximum (minimum) of the 68 % CL upward (downward) fluctuations of the CTEQ and MSTW sets, where the fluctuations in each set are given by the variations in alternative-fit-parameter-PDFs, scale and α_S, added in quadrature. The nominal cross section is then defined as the midpoint of the envelope and the cross section uncertainty is taken to be half the width.

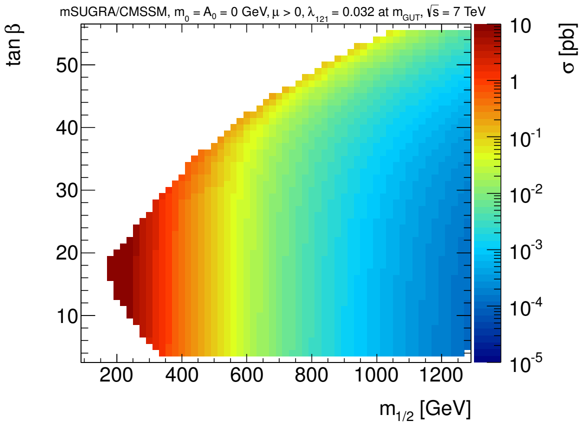

Figure 5.10: Total NLO(+NLL) production cross section.

Further details of the method used here to arrive at the values for the nominal NLO(+NLL) cross sections and their uncertainty estimates, which is based on the PDF4LHC recommendations [96], have been summarized in [97].

Since the ratio between LO and NLO cross sections is not the same for the production of all sparticle combinations, in the analysis, each simulated signal event has to be rescaled according to its combination's NLO cross section and the total number of events of this type found in the LO sample.

Figure 5.10 shows the total NLO(+NLL) sparticle production cross sections across the $m_{1/2}$–$\tan\beta$ plane around BC1, while the relative contributions of the production of squarks and gluinos, charginos and neutralinos, LSP pairs and other sleptons (charged sleptons as well as sneutrinos) are given in Fig. 5.11.

The total cross section falls with $m_{1/2}$, which increases the mass of the whole sparticle spectrum, while the total available center-of-mass energy stays the same. Above $\tan\beta$ values of about 30 this happens at higher values of $m_{1/2}$ under the influence of the very light $\tilde{\tau}_1$ (cf. Fig. 5.7c). While the typically dominant role of strong production processes at the LHC can also be seen here for models with low $m_{1/2}$, their contribution drops to a level comparable to that of direct production of neutralinos and charginos at about 700 GeV, where even the mass of the lightest squark is above 1 TeV, severely restricting the production phase space available at $\sqrt{s} = 7\,\text{TeV}$. Above about 1.1 TeV or for $\tan\beta \gtrsim 30$, direct LSP pair production becomes the dominant process. The remaining fraction is mainly due to the direct production of other slepton pairs.

As shown in Fig. 5.12a the maximum relative theoretical uncertainty on the cross sections can be up to about 100 % for individual production processes in the high $m_{1/2}$-region of the grid. The processes responsible for the highest relative uncertainties (associated, strong and at the highest $m_{1/2}$ values also weak gaugino production) only make up a (very) small fraction of the total production cross section in the affected region, though. As a way of taking into account the relative importance of the different production channels for each grid point, Fig. 5.12b displays the cross section weighted mean of the relative uncertainties, for comparison. This mean value is much smaller, with a maximum about 15 % at $m_{1/2}$ around 600 GeV and as small as 5 % in the high $\tan\beta$ region, where $\tilde{\tau}_1$ pair production dominates.

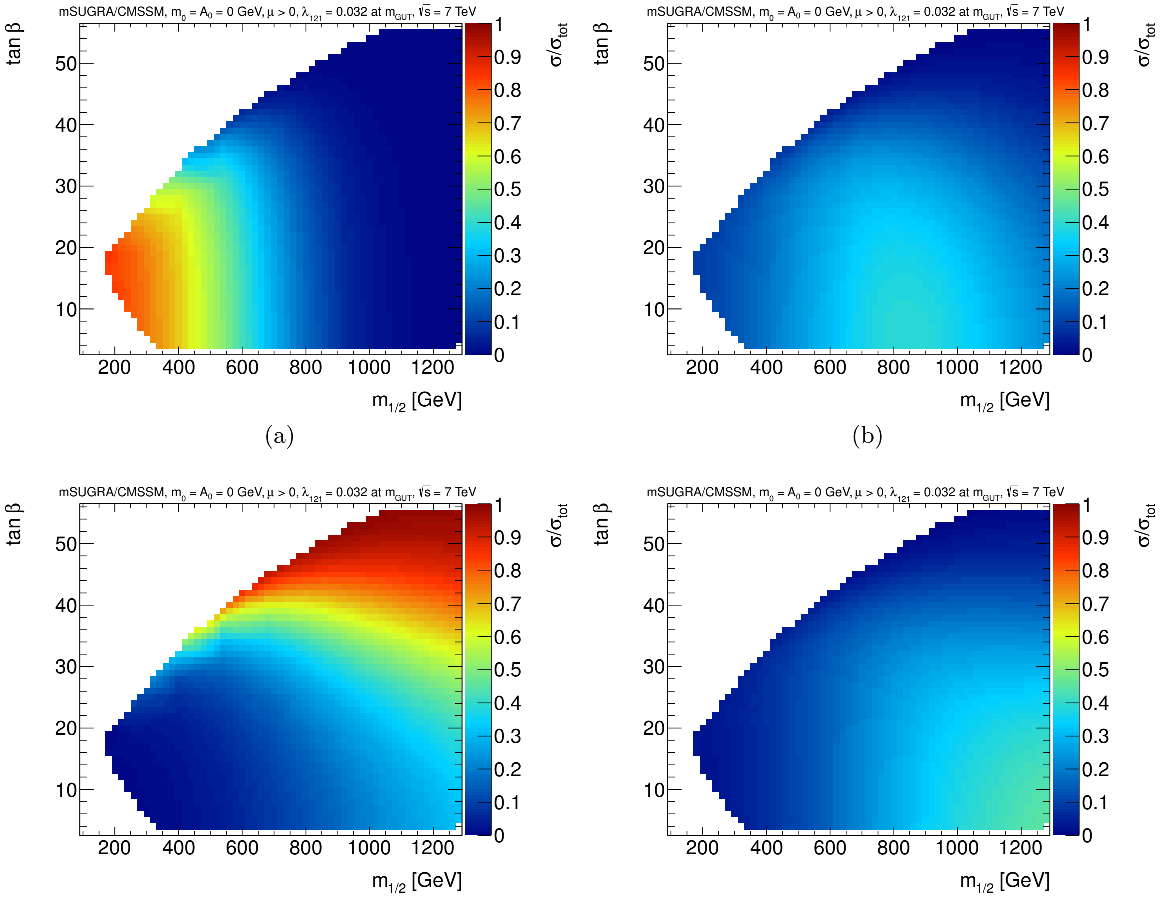

(a) (b)

(c) (d)

Figure 5.11: Relative contributions to the total cross section of squark and gluino (a), chargino and neutralino (b), $\tilde{\tau}_1$ pair (c) and other slepton–slepton production (d).

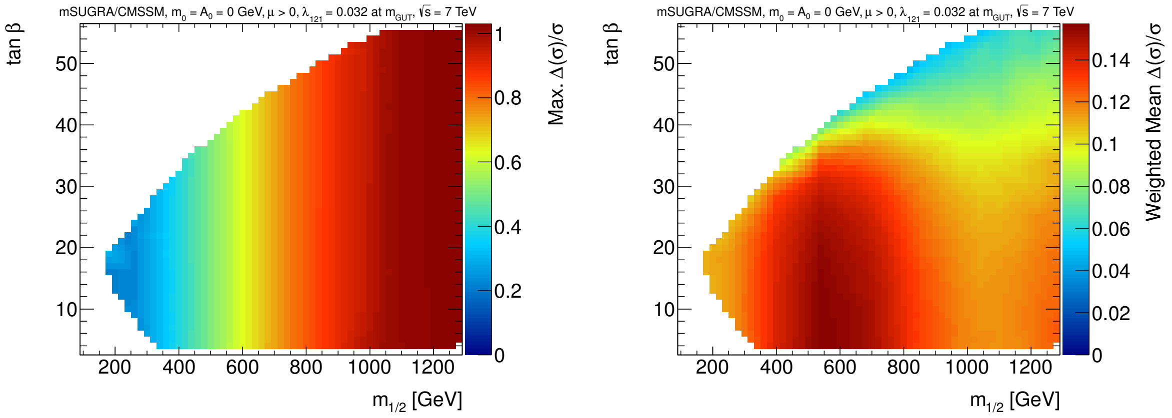

(a) (b)

Figure 5.12: Maximum (a) and cross section weighted mean (b) relative theoretical uncertainty on the production cross section.

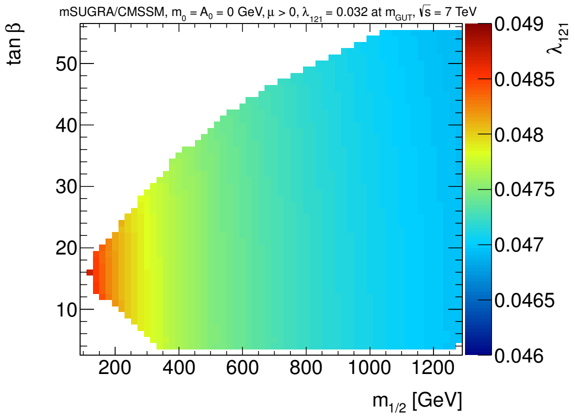

(a) generated λ_{121}

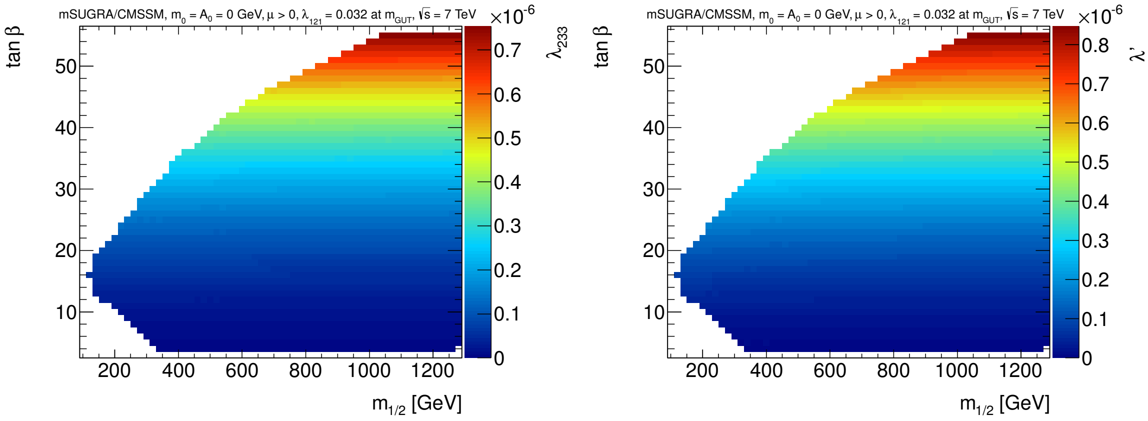

(b) generated λ_{233}

(c) generated λ'_{233}

Figure 5.13: Sizes of the R-parity violating couplings λ_{121} and the generated λ_{233} and λ'_{233} at M_{EW}.

5.3.3 Four- vs. Two-Body Decays of the LSP

As mentioned in Sec. 3.2.7, starting with only one non-zero $\not{R}_p$ coupling at M_{GUT}, further $\not{R}_p$ couplings can be generated in the RG evolution through loop effects as sketched in Fig. 3.11. While the size of this effect depends on the size of the original non-zero $\not{R}_p$ coupling and additional Yukawa couplings and is relevant mostly for third family sfermions, the effect plays a role in the very high $\tan\beta$ part of the parameter space, as can be seen in Fig. 5.13, where the values of the original coupling λ_{121}, as well as the two largest generated couplings, λ_{233} and λ'_{233}, are shown at the EW scale.

For the models discussed here the non-zero λ_{233} coupling allows additional R_p violating two-body decays of the $\tilde{\tau}_1$ LSP: $\tilde{\tau}_1 \xrightarrow{\lambda_{233}} \tau\nu_\mu$ or $\mu\nu_\tau$. Analogously to what is given in [98] and [32], the four- and two-body decay rates of the $\tilde{\tau}_1$ approximately depend on the $\not{R}_p$ couplings and the involved masses as follows:

$$\Gamma_4 \propto \lambda_{121}^2 \frac{m_{\tilde{\tau}_1}^7}{m_{\tilde{\chi}_1^0}^2 m_{\tilde{f}}^4} \qquad , \qquad \Gamma_2 \propto \lambda_{233}^2 m_{\tilde{\tau}_1} \tag{5.1}$$

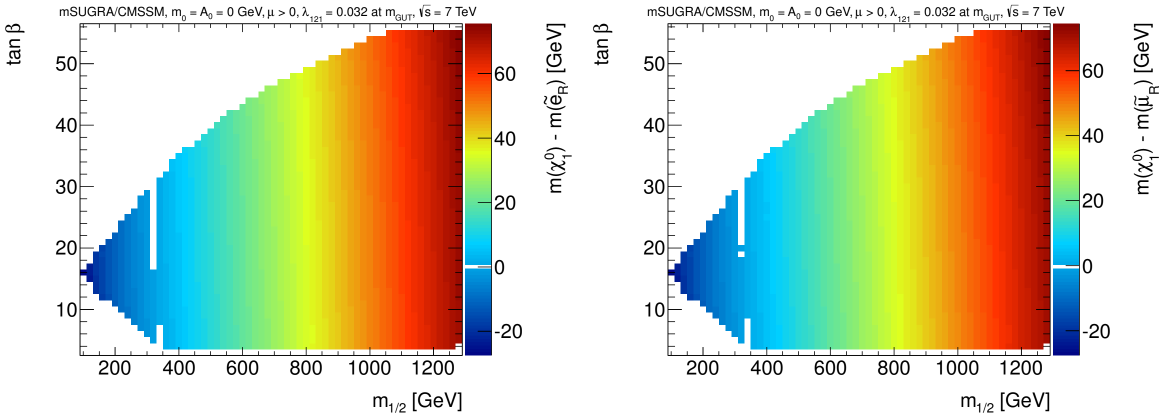

(a) $m(\tilde{\chi}_1^0) - m(\tilde{e}_\mathrm{R})$

(b) $m(\tilde{\chi}_1^0) - m(\tilde{\mu}_\mathrm{R})$

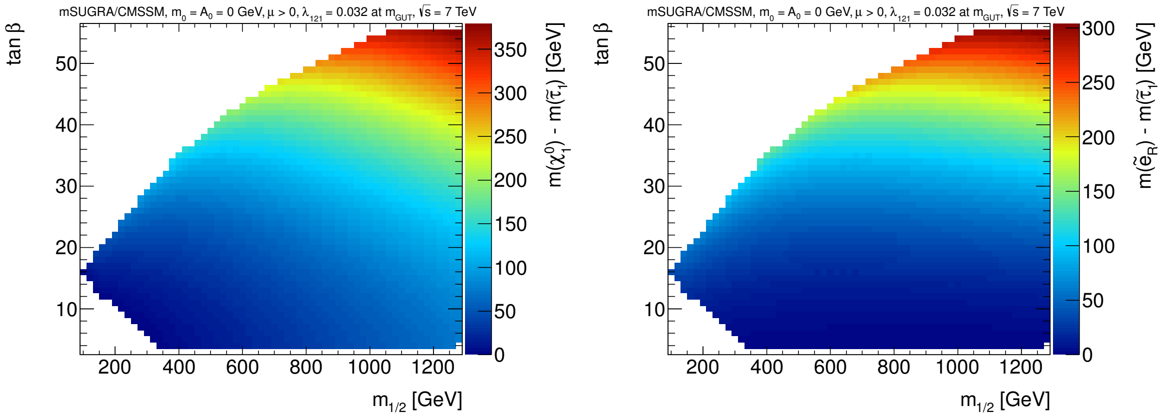

(c) $m(\tilde{\chi}_1^0) - m(\tilde{\tau}_1)$

(d) $m(\tilde{e}_\mathrm{R}) - m(\tilde{\tau}_1)$

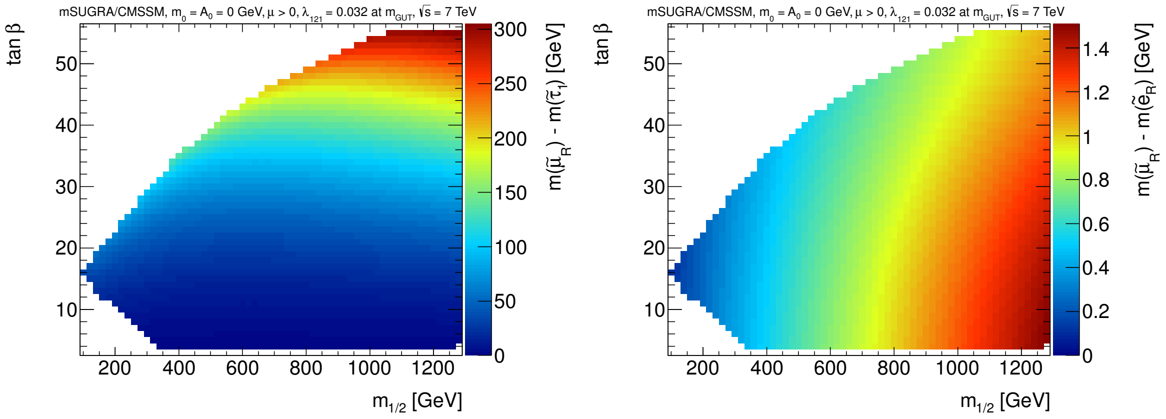

(e) $m(\tilde{\mu}_\mathrm{R}) - m(\tilde{\tau}_1)$

(f) $m(\tilde{\mu}_\mathrm{R}) - m(\tilde{e}_\mathrm{R})$

Figure 5.14: Mass differences between the four lightest sparticles, $\tilde{\chi}_1^0$, $\tilde{e}_\mathrm{R}$, $\tilde{\mu}_\mathrm{R}$ and $\tilde{\tau}_1$.

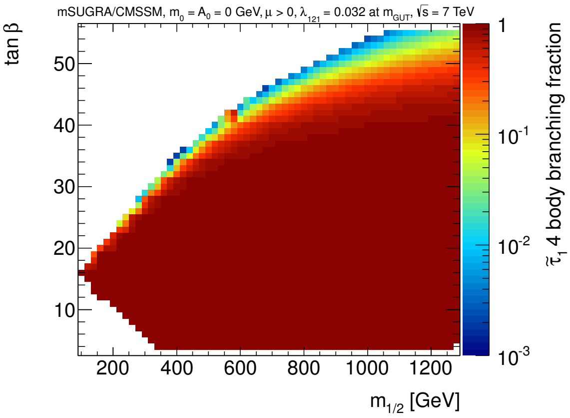

Figure 5.15: Fraction of four- vs. two-body decays of the $\tilde{\tau}_1$.

where $m_{\tilde{f}}$ is the mass of the virtual sfermion involved in the decay. This means that the relative importance of the two competing types of decay processes increases quadratically with the ratio of the $\not{R}_p$ couplings, but more rapidly with the growing mass differences between the $\tilde{\tau}_1$ and the other involved sparticles. These differences become large for high $\tan\beta$ values as shown in Fig. 5.14c–e for the four lightest sparticles.

The resulting fraction of the four-body decays of the $\tilde{\tau}_1$ across the $m_{1/2}$–$\tan\beta$ plane can be seen in Fig. 5.15. It shows that for most of the analyzed parameter space the assumption of a four-body decay of the LSP and the resulting multi-lepton signature is valid. Nevertheless, rapid changes can be seen close to the upper border of the grid, where two-body decays dominate.

5.3.4 Lifetime of the Lightest Sparticles

A second effect of the strong dependence of the $\tilde{\tau}_1$ four-body decay rate on its mass becomes apparent when looking at the inverse of the rate: the $\tilde{\tau}_1$ lifetime. As shown in Fig. 5.16a at the upper $\tan\beta$ border of the grid, it becomes larger than about 1 ps, equivalent to 0.3 mm before applying any boost factors, thus exceeding the limit of sensitivity for the four lepton analysis, given by the cosmic muon veto (c.f. Sec. 4.4.1) and for cm-distances also given by the track quality requirements for electron and muon, which include the number of hits in the vertex detector as one possible criterion.

Figure 5.16b shows a problem of the MC event generation concerning the simulated lifetime of the right-handed smuon at small $\tan\beta$, where the values very quickly increase from fractions of a ps up to 10^{11} ps, effectively rendering the smuon stable on detector scales. This happens for the following reason: For $\tan\beta$ values down to 7 the dominant decay is $\tilde{\mu}_\mathrm{R} \to (\tilde{\chi}_1^0)^*\mu \to \tilde{\tau}_1\tau\mu$. At $\tan\beta = 4$, though, the mass difference between the three lightest charged sleptons (c.f. Fig. 5.14) becomes smaller than the τ mass. While at $m_{1/2} = 340$ GeV the $\tilde{\chi}_1^0$ is still lighter than the smuon and $\tilde{\mu}_\mathrm{R} \to \tilde{\chi}_1^0\mu$ is kinematically possible, this is not the case for higher values of $m_{1/2}$. Since the right-handed smuon does not couple to the R-parity violating operator $L_1L_2\bar{E}_1$ directly and a four-body decay comparable to the $\tilde{\tau}_1$ case (e.g. $\tilde{\mu}_\mathrm{R} \to (\tilde{\chi}_1^0)^*\mu \to (\tilde{e}_\mathrm{R})^*e\mu \xrightarrow{\lambda_{121}} e\nu_\mu e\mu$) was not implemented in Herwig, only the R_p conserving decay $\tilde{\mu}_\mathrm{R} \to (\tilde{\chi}_1^\pm)^*\nu_\mu \to \tilde{\tau}_1\nu_\tau\nu_\mu$ via a far

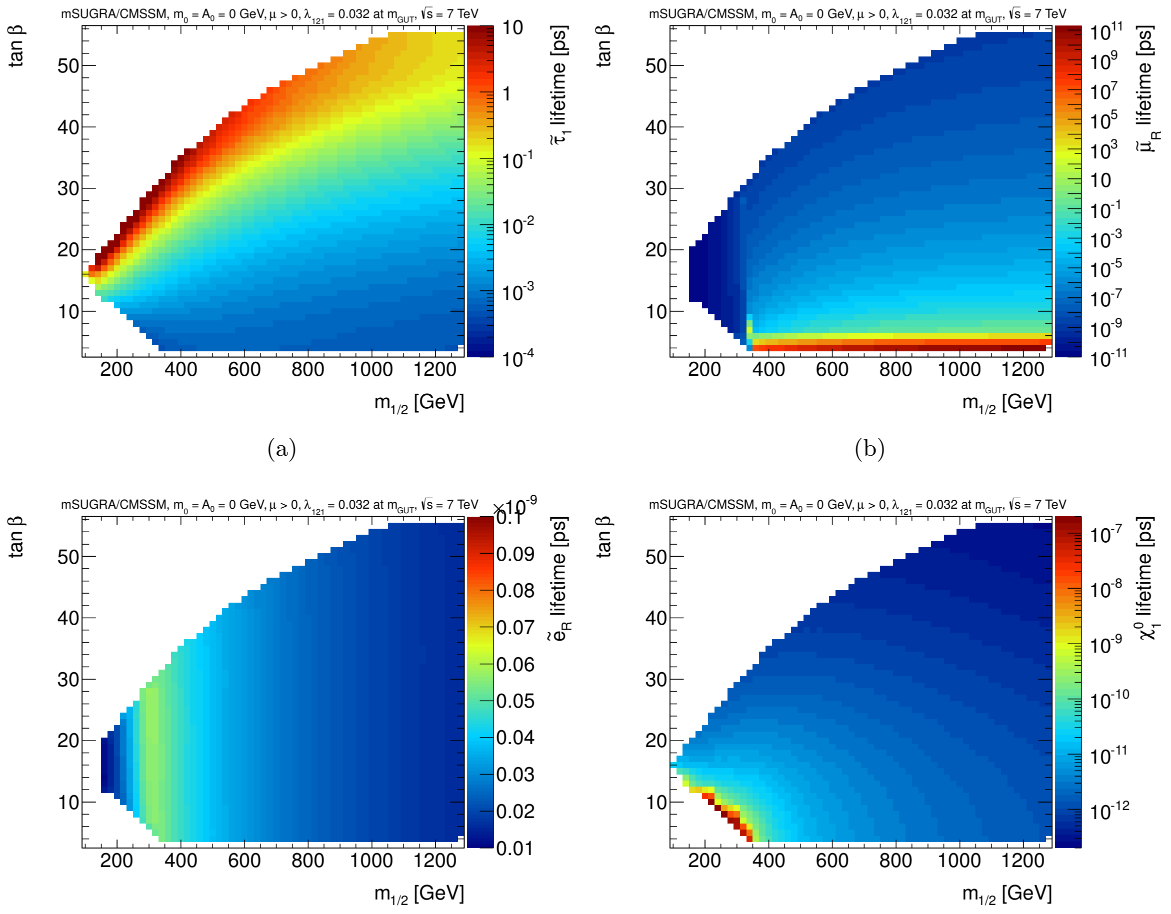

(a)

(b)

(c)

(d)

Figure 5.16: Lifetimes of the $\tilde{\tau}_1$ (a), $\tilde{\mu}_\mathrm{R}$ (b), $\tilde{e}_\mathrm{R}$ (c) and the $\tilde{\chi}_1^0$ (d).

off-shell virtual chargino was simulated, leading to the unphysical prediction shown here. This effect does not pose a significant problem for the analysis, though, since most of the affected region is already excluded from the search by the LEP Higgs limits and only a fraction of possible final states is affected.

In comparison to the previous two, the lifetimes of the right-handed selectron and the lightest neutralino pose no problem for the analysis. The $\tilde{e}_\mathrm{R}$ lifetime can be seen in Fig. 5.16c and only shows a slight increase near $m_{\tilde{e}_\mathrm{R}} = m_{\tilde{\chi}_1^0}$, where the dominant decay changes from an R-parity violating mode to a decay to the lightest neutralino. The $\tilde{\chi}_1^0$ lifetime is shown in Fig. 5.16d. As expected it increases close to the $m_{\tilde{\tau}_1} = m_{\tilde{\chi}_1^0}$ border, as the direct decay $\tilde{\chi}_1^0 \rightarrow \tilde{\ell}_{R/1}\ell$ is no longer kinematically possible and replaced by R-parity violating three-body decays like $\tilde{\chi}_1^0 \rightarrow \ell(\tilde{\ell})^* \xrightarrow{\lambda_{121}} \ell\ell\nu$, which are suppressed by the size squared of the $\not{R}_p$ coupling.

Due to the size of the increase and the placement of grid points in $\tan\beta$ some interpolation artifacts can be seen in 5.16b and d.

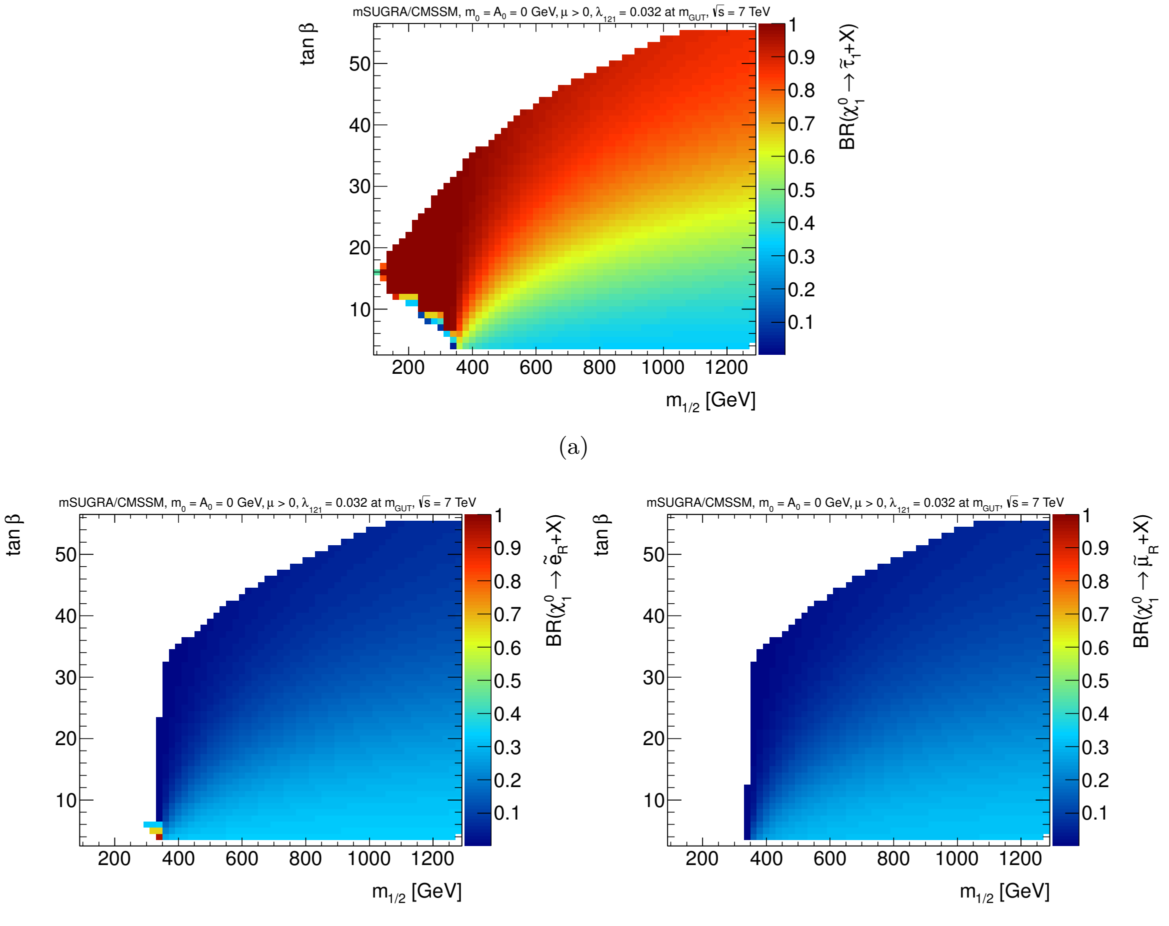

(a)

(b)

(c)

Figure 5.17: Branching ratios of the lightest neutralino into $\tilde{\tau}_1$ (a), $\tilde{e}_\mathrm{R}$ (b) and $\tilde{\mu}_\mathrm{R}$ (c).

5.3.5 Decays of the Lightest Neutralino into the Lightest Sleptons

Lastly, for the BC1 benchmark point the lightest neutralino mostly decays to a $\tilde{\tau}_1$ and a tau, leading to the possibility of a striking, but very challenging to select, four tau plus four lepton plus $E_\mathrm{T}^\mathrm{miss}$ signature. Figure 5.17 shows that this is also the case for $m_{1/2}$ values below about 350 GeV, where the $\tilde{\chi}_1^0$ becomes the NLSP. For $m_{1/2}$ values above that and low $\tan\beta$ this branching ratio approaches ⅓, though, as the $\tilde{\tau}_1$, the $\tilde{\mu}_\mathrm{R}$ and the $\tilde{e}_\mathrm{R}$ are almost mass degenerate and the decay itself is flavor-blind. As in the case of the lifetimes mentioned above, some interpolation artifacts can be seen at the $m_{\tilde{\tau}_1} = m_{\tilde{\chi}_1^0}$ border, where at the lower left edge in Fig. 5.17b only the decay $\tilde{\chi}_1^0 \to \tilde{e}_\mathrm{R} + e$ is kinematically possible and in Fig. 5.17a only R_p violating three body decays of the $\tilde{\chi}_1^0$ are open (e.g. $\tilde{\chi}_1^0 \to (\tilde{\mu}_\mathrm{R})^* + e \xrightarrow{\lambda_{121}} e\nu_e e$).

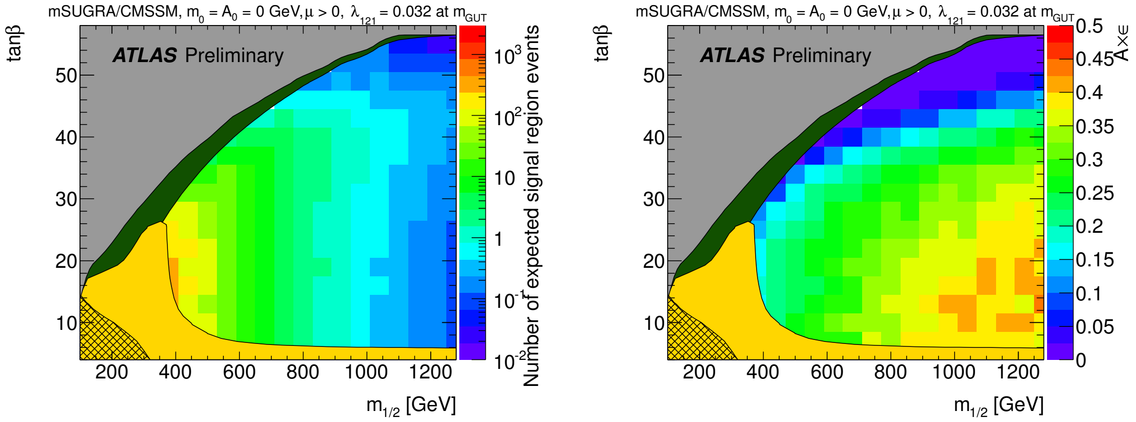

(a) (b)

Figure 5.18: Number of signal events expected in SR2 for $2.06\,\mathrm{fb}^{-1}$ (a) and signal acceptance times efficiency of the four lepton analysis, averaged over all production processes (b). [87]

5.4 Analysis Results in the Parameter Plane

While the model properties discussed in the previous sections can be seen as a point of reference, the generated events still have to pass through reconstruction and identification as well as all cuts defining the signal regions of the four lepton analysis, as discussed in the previous chapter. Since for the BC1-like models discussed above the presence of a Z boson is not necessary to produce the desired final state, the second signal region (SR2), which explicitly rejects lepton pairs of same sign and opposite flavor close to the Z peak is used for this interpretation. Figure 5.18a shows the number of signal events expected in SR2 for an integrated luminosity of $2.06\,\mathrm{fb}^{-1}$ as a function of $m_{1/2}$ and $\tan\beta$.

As noted in Sec. 4.9 this reflects the "visible" cross section, σ_{vis}, only. The ratio of visible and production cross section is given by the product of kinematic acceptance, A, and the selection efficiency, ϵ.

$$\sigma_{\mathrm{vis}} = \frac{N_{\mathrm{sel}}}{\int \mathcal{L}\,\mathrm{d}t} = A \times \epsilon \cdot \sigma \qquad \text{or} \qquad N_{\mathrm{sel}} = A \times \epsilon \cdot N_{\mathrm{gen}} \tag{5.2}$$

where N_{sel} is the number of events selected by the analysis and N_{gen} is the number of generated events for the model.

The value of $A \times \epsilon$ as a function of $m_{1/2}$ and $\tan\beta$, averaged over all production processes, is displayed in Fig. 5.18b. It increases towards high $m_{1/2}$ and low $\tan\beta$, becoming as large as 45 %. The same trend can be found for the separate types of production processes, as shown in Fig. 5.19 for strong production of squarks and gluinos and weak production of charginos and neutralinos (called "gauginos" in the figures of this section), LSP pairs, as well as combinations of the other leptons. Note the different color-scale of the latter two, though. The strong statistical fluctuations, which are clearly visible for the case of strong production in this and the following figures are due to the small number of events contributing to the signal region, as shown in Fig. 5.22.

Since theorists typically do not have access to the simulation and reconstruction frameworks

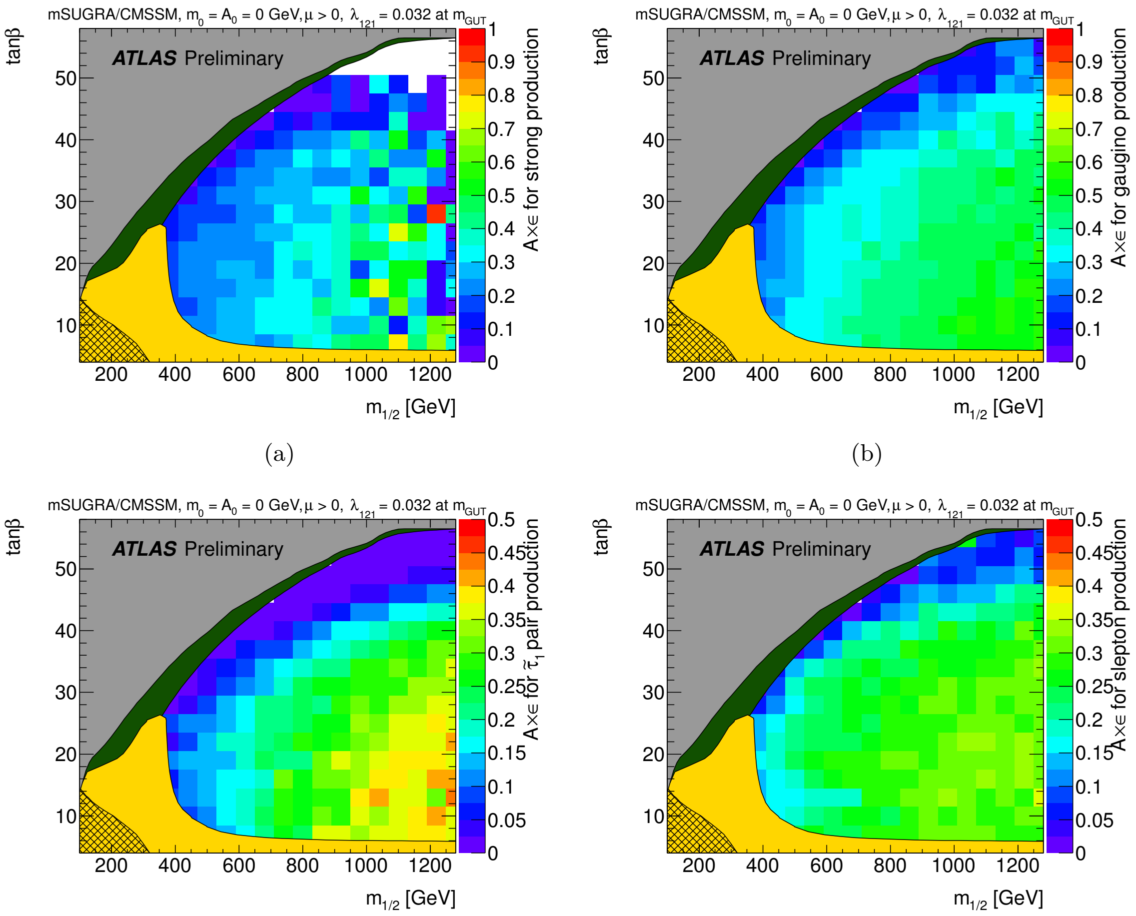

(a)

(b)

(c)

(d)

Figure 5.19: Signal acceptance times efficiency for squark and gluino (a), chargino and neutralino (b), $\tilde{\tau}_1$–$\tilde{\tau}_1$ (c) and other slepton–slepton (d) production. [87]

of the detector experiments, and can thus only estimate the efficiency of reconstruction and identification, it is important to either unfold these effects from the analysis results or provide numbers for the efficiency so that further studies and comparisons are possible.

On the experimentalists' side this information is helpful for understanding the different sources of limitations for the performance of the analysis (model/simulation vs. detector/reconstruction/identification) and for adjusting the future analysis strategy.

Using the truth information contained in the generated events and applying all cuts of the analysis related to the number of objects and their kinematic properties, it is possible to determine the acceptance, here defined as

$$A = \frac{N_{\mathrm{sel}}^{\mathrm{truth}}}{N_{\mathrm{gen}}} \tag{5.3}$$

and the efficiency

$$\epsilon = \frac{N_{\mathrm{sel}}}{N_{\mathrm{sel}}^{\mathrm{truth}}} \tag{5.4}$$

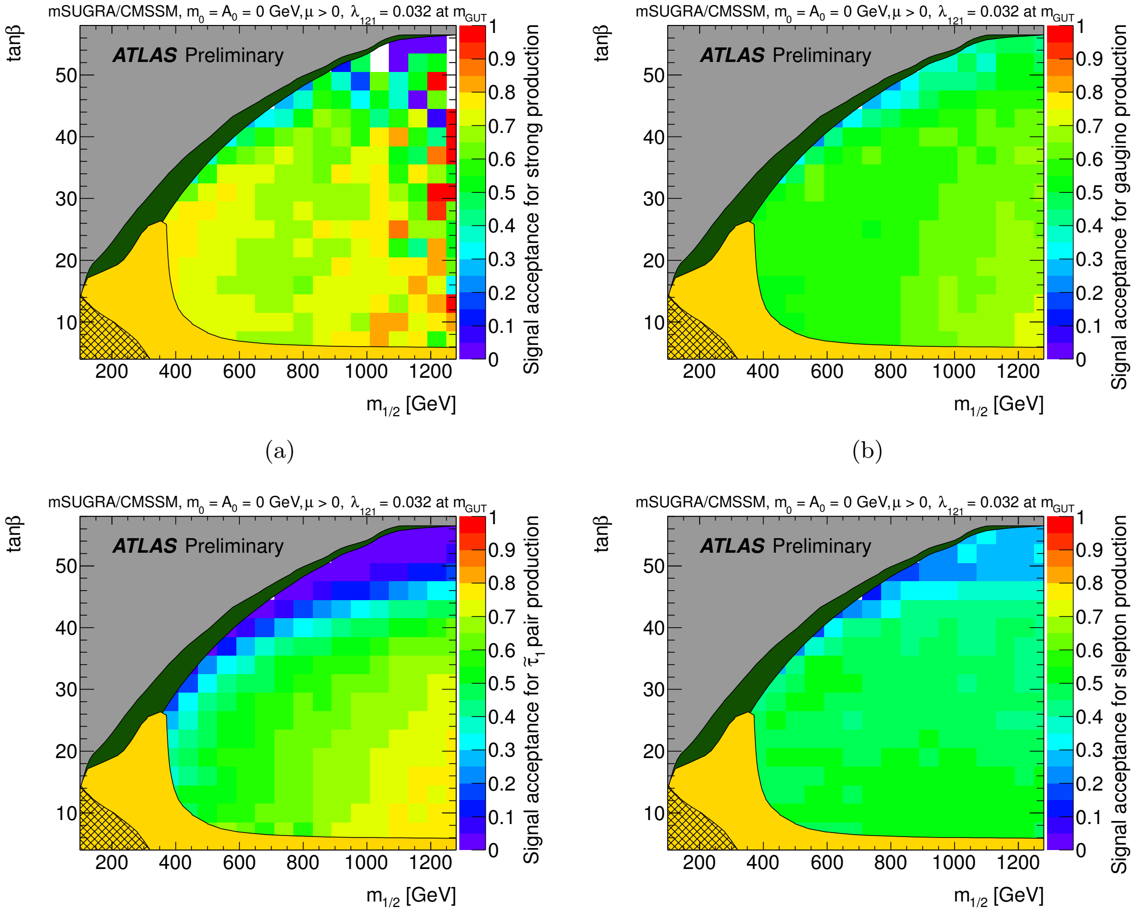

(a) (b)

(c) (d)

Figure 5.20: Signal acceptance for squark and gluino (a), chargino and neutralino (b), $\tilde{\tau}_1$–$\tilde{\tau}_1$ (c) and other slepton–slepton (d) production. [87]

where $N_{\mathrm{sel}}^{\mathrm{truth}}$ is the number of events selected at truth level. The resulting values of the acceptance across the $m_{1/2}$–$\tan\beta$ plane can be seen in Fig. 5.20 for the four different types of production processes.

For all types of production processes the acceptance is above 50 % over most of the parameter space. It reaches up to about 80 % for strong production at low $m_{1/2}$ and $\tilde{\tau}_1$ pair production at high $m_{1/2}$ and low $\tan\beta$. A general loss of acceptance is seen for all processes close to the region excluded due to a small $\tilde{\tau}_1$ mass, with the largest decrease down to a complete loss of sensitivity for LSP pairs at high $\tan\beta$, as generally expected from the model properties discussed in Sec. 5.3.

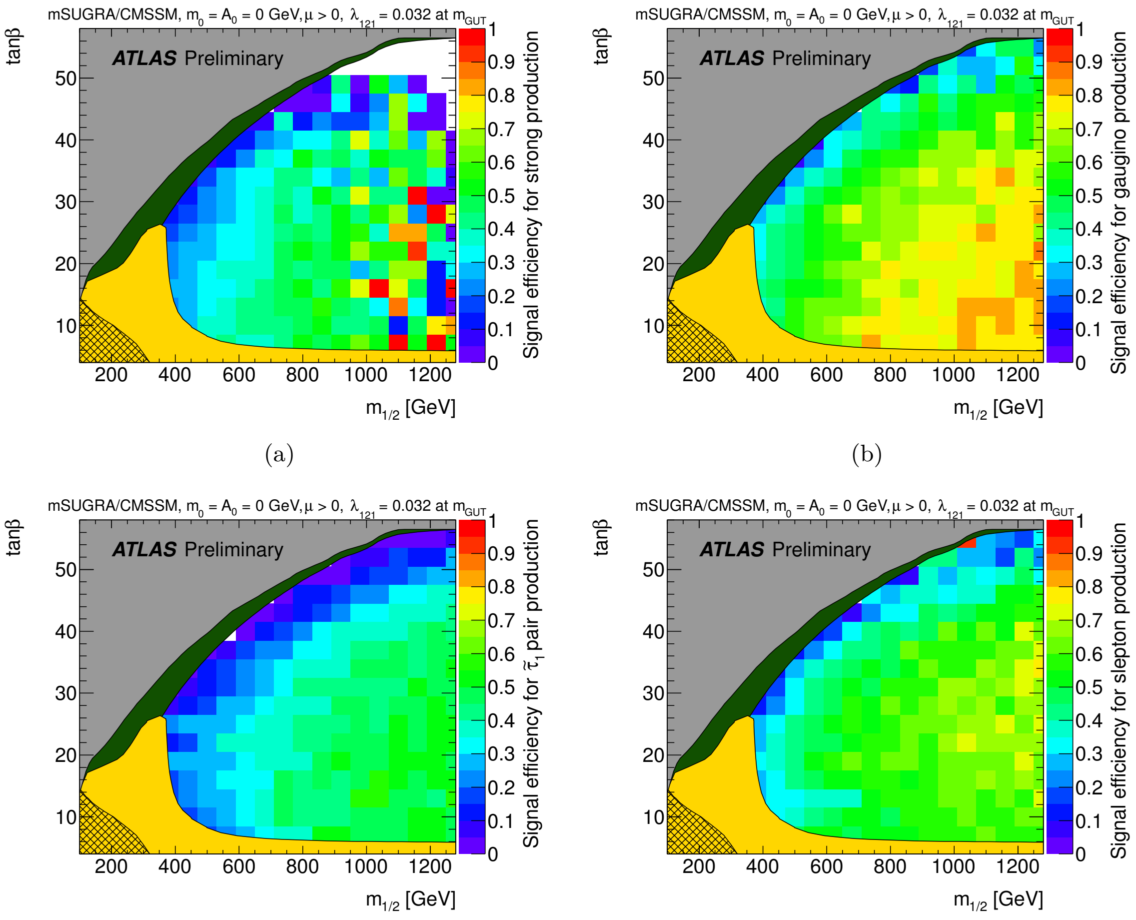

(a) (b)

(c) (d)

Figure 5.21: Signal efficiency for squark and gluino (a), chargino and neutralino (b), $\tilde{\tau}_1$–$\tilde{\tau}_1$ (c) and other slepton–slepton (d) production. [87]

The accompanying efficiency distributions are shown in Fig. 5.21. The efficiency is largest in the high $m_{1/2}$ and low $\tan\beta$ region with up to about 80 % for the production of weak gauginos and above 50 % for the other processes. Like the acceptance it drops towards higher $\tan\beta$ values and lower $m_{1/2}$, with the lowest values for LSP pairs and strong production.

Combining these acceptances and efficiencies with the corresponding fractional cross sections, which were given in Fig. 5.11, results in the relative contributions of the four types of production processes to the overall number of events expected in SR2, which are shown in Fig. 5.22. Over most of the parameter space the relative changes in cross section are the dominating effect. Close to the region excluded due to a light $\tilde{\tau}_1$ mass at high $\tan\beta$, however, the contributions of weak gaugino and non-$\tilde{\tau}_1$-pair slepton production show a strong relative gain in importance. The reason for this are the additional leptons that can be produced in the decay of the initial sparticles to a $\tilde{\tau}_1$, that can compensate for the smaller number of leptons expected from the two-body decays of the LSP, which is not possible in the case of direct $\tilde{\tau}_1$-pair production.

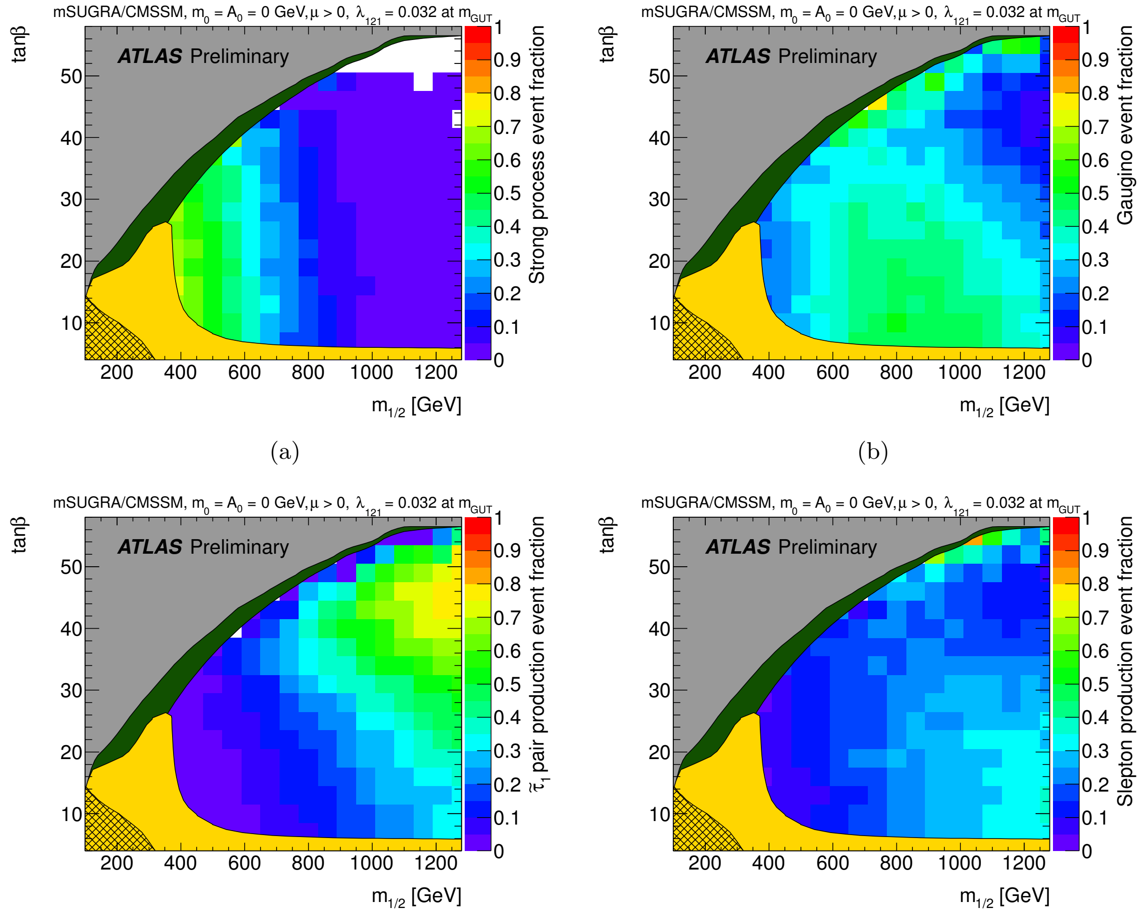

(a)

(b)

(c)

(d)

Figure 5.22: Relative contribution to the signal expectation from squark and gluino (a), chargino and neutralino (b), $\tilde{\tau}_1$–$\tilde{\tau}_1$ (c) and other slepton–slepton (d) production. [87]

5.5 Statistical Interpretation of Results

As the four lepton analysis found no significant disagreement between the SM MC predictions and the number of events observed in data, upper limits were set on the number of predicted signal events or the corresponding visible cross section, respectively, as summarized in Tab. 4.9. To test if a given signal model is excluded or not, as a first approximation, this limit can be directly applied to the number of predicted events in the signal region, as given in Fig. 5.18a. This neglects possible fluctuations of the predicted number of signal events due to theoretical (e.g. cross section) and experimental (e.g. electron energy scale) uncertainties as well as correlations of the uncertainties with those of the SM background prediction, though. Since these uncertainties have been computed for the BC1-like models discussed above, they are included in the limit setting procedure described below.

A frequentist method is used to assess the agreement between the observed data and the hypothesis of observing either the sum of a signal and background or background only. The method is based on the approach presented in [99], as implemented in the "ATLAS SUSY Combination" package [100]. The quantity used to measure the agreement can be expressed in terms of the probability to find results at least as incompatible with the prediction of the tested hypothesis as what was observed in data:

$$p = \int_{q_{\mathrm{obs}}}^{\infty} f(q|H)\,\mathrm{d}q \tag{5.5}$$

where the test statistic, q, used to quantify the incompatibility with the hypothesis, H, is distributed according to a probability density $f(q|H)$. Its value observed in data is q_{obs} and higher values of q express greater incompatibility.

This test statistic then has to incorporate all the information about the signal and background predictions and the observation that is to be used to judge compatibility. For this interpretation of BC1-like models and a number of other ATLAS SUSY searches, the test statistic is built around a profile likelihood ratio, where the likelihood is defined as

$$L(\mu, \boldsymbol{\theta}) = \mathrm{Pois}\Big(n, \mu s(\boldsymbol{\theta}) + b(\boldsymbol{\theta})\Big)\, P_{\mathrm{syst}}(\boldsymbol{\theta}) \tag{5.6}$$

The first term is the Poisson probability to observe n events if the expectation is $\mu s + b$. The signal strength parameter, μ, is introduced as a free parameter with the cases of $\mu = 1$ corresponding to the signal plus background hypothesis and $\mu = 0$ to the background-only hypothesis. The uncertainties of the signal and background predictions are accounted for by defining:

$$s(\boldsymbol{\theta}) = s_{\mathrm{tot}}\Big(1 + \sum_i \theta_i \sigma_i^s\Big) \qquad \text{and} \qquad b(\boldsymbol{\theta}) = b_{\mathrm{tot}}\Big(1 + \sum_j \theta_j \sigma_j^b\Big) \tag{5.7}$$

where s_{tot} and b_{tot} are the nominal values for signal and background expectation given by the MC, σ_i^s and σ_j^b are the corresponding relative systematic uncertainties and the $\theta_{i,j}$ are nuisance parameters.

The second term in Eq. 5.6, $P_{\mathrm{syst}}(\boldsymbol{\theta})$, describes the combined probability distribution of all nuisance parameters, which in this case is a product of Gaussians, each with zero mean and a standard deviation of one. They model the distributions of the uncertainties on the luminosity, the jet energy scale and the electron energy scale, which are treated as 100 % correlated between signal and background, as well as one combined uncertainty for the remaining systematics on the signal and one combined uncertainty for the remaining systematics on the background, which are assumed to be uncorrelated.

Based on this a profile likelihood ratio can be calculated:

$$\lambda(\mu) = \frac{L\left(\mu, \hat{\hat{\boldsymbol{\theta}}}(\mu)\right)}{L\left(\hat{\mu}, \hat{\boldsymbol{\theta}}\right)} \tag{5.8}$$

where the $\hat{\hat{\boldsymbol{\theta}}}(\mu)$ in the numerator maximizes the likelihood for a fixed value of μ, while $\hat{\mu}$ and $\hat{\theta}$ in the denominator maximize the likelihood with floating values of signal strength and the nuisance parameters. The profiling procedure, consisting of the maximum likelihood fits, reduces the dependencies of the resulting likelihood ratio to the strength parameter μ alone. Values for $\lambda(\mu)$ thus defined vary between zero and one.

Since the signal strength is supposed to only add to the overall number of events observed in the signal region (assuming no negative interference of amplitudes), physical values of μ should not be negative. To take this into account, the definition of the profile likelihood ratio is slightly altered, such that if the observed data leads to $\hat{\mu} < 0$ the likelihood in the denominator is instead maximized for fixed $\mu = 0$, as the smallest value that can be realized:

$$\tilde{\lambda}(\mu) = \begin{cases} \frac{L\left(\mu,\hat{\hat{\boldsymbol{\theta}}}(\mu)\right)}{L\left(\hat{\mu},\hat{\boldsymbol{\theta}}\right)} & \hat{\mu} \geq 0 \\ \frac{L\left(\mu,\hat{\hat{\boldsymbol{\theta}}}(\mu)\right)}{L\left(0,\hat{\hat{\boldsymbol{\theta}}}(0)\right)} & \hat{\mu} < 0 \end{cases} \tag{5.9}$$

Following the recommendation from [99] further, the test statistic for determining the one-sided upper limits, $\tilde{q}_\mu$, finally is defined as:

$$\tilde{q}_\mu = \begin{cases} -2\ln\tilde{\lambda}(\mu) & \hat{\mu} \leq \mu \\ 0 & \hat{\mu} > \mu \end{cases} = \begin{cases} -2\ln\frac{L\left(\mu,\hat{\hat{\boldsymbol{\theta}}}(\mu)\right)}{L\left(0,\hat{\hat{\boldsymbol{\theta}}}(0)\right)} & \hat{\mu} < 0 \\ -2\ln\frac{L\left(\mu,\hat{\hat{\boldsymbol{\theta}}}(\mu)\right)}{L\left(\hat{\mu},\hat{\boldsymbol{\theta}}\right)} & 0 \leq \hat{\mu} < \mu \\ 0 & \hat{\mu} > \mu \end{cases} \tag{5.10}$$

This transforms the range of values to $[0, \infty)$, so that higher values of the test statistic correspond to a higher incompatibility of data and hypothesis μ. In addition, in the large sample limit, $-2\ln\tilde{\lambda}(\mu)$ becomes a chi-squared-type distribution, making further analytic calculation of the asymptotic behavior possible and, as done in [100], even allowing a re-parametrization of the test statistic directly in the form of p-values, as the cumulative distribution is known.

Equation 5.10 also adds a second distinction of cases for $\hat{\mu} > \mu$, as μ-values smaller than the value corresponding to the maximum likelihood for a given observation are not regarded as less compatible to the data for the purpose of setting an upper limit.

In analogy to Eq. 5.5 the p-values for a hypothetical signal strength μ are then given by

$$p_\mu = \int_{\tilde{q}_{\mu,\mathrm{obs}}}^{\infty} f(\tilde{q}_\mu|\mu)\,\mathrm{d}\tilde{q}_\mu \tag{5.11}$$

As the size of the data sample in both signal regions is too small to rely on the asymptotic formulas given in the references, the distribution of the test statistic, $f(\tilde{q}_\mu|\mu)$, has to be determined with the help of pseudo-experiments. These simulate new measurements with new hypothetical values for n and new mean values for the distributions of the nuisance parameters $\boldsymbol{\theta}$, which are randomly drawn according to their initial distributions[5]. These pseudo-data sets are then used to first find the new maximum likelihood estimators, $\hat{\hat{\boldsymbol{\theta}}}(\mu)$, $\hat{\boldsymbol{\theta}}$ and $\hat{\mu}$, for the likelihood ratio, and then to re-evaluate the test statistic, resulting in the required distribution.

One possibility, called CL_{s+b} method, for an exclusion at 95 % confidence level (C.L.) is then to require the above probability, to be $p_\mu < 1 - 0.95 = 0.05$. A problem with this approach is that if $s \ll b$ then a downward fluctuation of the background can lead to the exclusion of a signal model, for which there is actually no sensitivity. Alternatively the definition of an exclusion can be modified to account for such cases, as done in the CL_s method [101], by factoring in the confidence in the background-only hypothesis for the same observation. While not strictly necessary for this interpretation of signal models, the CL_s method is adopted for setting limits, to be consistent with the four lepton analysis.

The exclusion criterion for a signal model then is defined as:

$$\mathrm{CL}_s \equiv \frac{\mathrm{CL}_{s+b}}{\mathrm{CL}_b} = \frac{p_{\mu=1}}{1-p_b} < 0.05 \tag{5.12}$$

with

$$\mathrm{CL}_b = 1 - p_b = \int_{\tilde{q}_{\mu,\mathrm{obs}}}^{\infty} f(\tilde{q}_\mu|0)\,\mathrm{d}\tilde{q}_\mu \tag{5.13}$$

where the distribution $f(\tilde{q}_\mu|0)$ is generated with pseudo-experiments as above, but setting $\mu = 0$.

The observed upper limit on the signal strength μ_{up} can be found numerically by solving:

$$\frac{p_{\mu_{\mathrm{up}}}}{1-p_b} = 0.05 \tag{5.14}$$

In addition to the observed limit, the median expected upper limit and its one sigma uncertainties are found by repeating the above procedure using pseudo-data sets produced assuming the background-only hypothesis in place of the observation, to generate a distribution of upper limits. The median limit then is the 50 % quantile of this distribution and the $\pm 1\sigma$ values are given by the 16 % and 84 % quantiles, respectively.

In the case of the four lepton analysis, which only assumed a specific final state instead of a complete signal model with a nominal cross section to relate to or theoretical uncertainties

---

[5] For generating the new pseudo-data set the signal strength is fixed to one for setting upper limits and to zero when computing deviations from the background-only hypothesis.

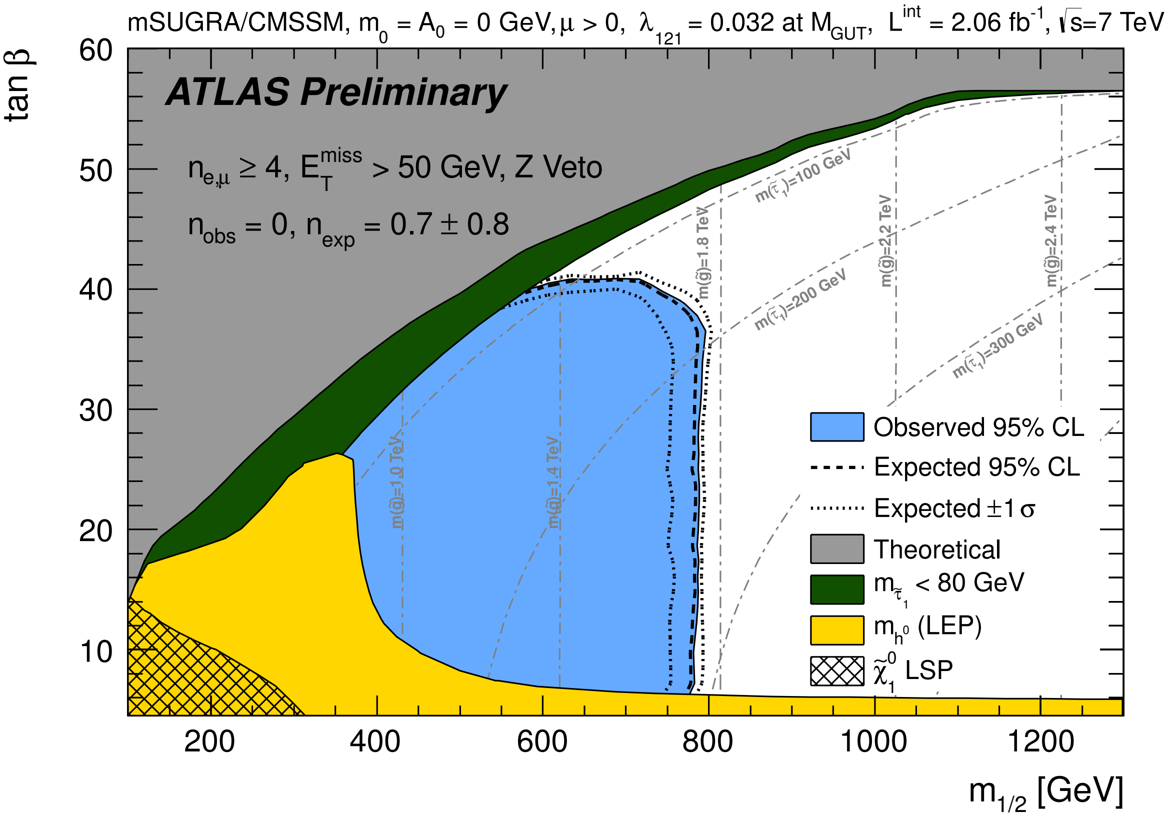

Figure 5.23: Observed and expected 95 % confidence level exclusion regions, calculated with the CL_s method for 2.06 fb^{-1}. [87]

on the signal, these limits were converted into a number of events and a visible cross section instead, as reported in [41] and summarized in Sec. 4.9.

For the BC1-like models discussed in this chapter, the observed and expected CL_s values for each grid point can be interpolated in the $m_{1/2}$–$\tan\beta$ plane, resulting in the exclusion regions shown in Fig. 5.23.

The observation of 0 events for a SM expectation of 0.7 ± 0.8 events excludes models in a region of $m_{1/2} \lesssim 800$ GeV and $\tan\beta \lesssim 40$. As indicated by the overlaid mass contours, this translates into a lower limit on gluino masses of about 1770 GeV in this framework.

These results were obtained for a nominal value of the R-parity violating parameter, $\lambda_{121} = 0.032$ (at M_{GUT}). As discussed in this chapter, the expected number of signal events depends mostly on the mass and the related lifetime and four-body branching fraction of the $\tilde{\tau}_1$. Comparing the nominal sparticle mass spectrum and decays of the $\tilde{\tau}_1$ with models where the GUT-scale λ_{121} values were changed by factors of 0.5 and 2, only small quantitative differences were found. The most significant effect is expected on the high-$\tan\beta$ border of the excluded region, due to the reduction in reconstruction efficiency for $\tilde{\tau}_1$ lifetimes above the sensitivity of the analysis of about 1 ps.

CHAPTER 6

Summary and Conclusions

The Standard Model of particle physics has been tested with high precision by many experiments in the decades since its formulation. With the observation of a SM-compatible Higgs boson by the ATLAS and CMS experiments, the SM's last missing elementary particle has by now been found, reaching the first of the LHC's main physics goals.

Despite its obvious successes, the SM contains a number of open issues pointing at physics beyond the SM. Among them are the questions of how the Higgs boson's mass is stabilized at higher orders in perturbation theory, if and how the electroweak and strong forces are unified at higher energies and how to incorporate the experimental observation of non-zero neutrino masses into the picture. Open issues such as these have lead to a plethora of possible extensions of the theory, thus defining the second main goal of the LHC: searching for signals predicted by these BSM physics models or excluding models where no such signal is found.

One widely studied class of BSM models are supersymmetric extensions of the SM, which address the Hierarchy Problem by predicting systematic cancellations. To explain why none of the superpartners has been observed so far, SUSY has to be broken, though. Nevertheless, at least some of the masses of the newly predicted elementary particles have to be at or below the TeV scale, in range of the LHC, to achieve the necessary effect of the cancellations. Although a grand unified theory is no requirement of SUSY, in case of the MSSM, the running of the couplings is modified compared to the SM in a way that more obviously hints at gauge unification.

To address the issue of rapid proton decay, which is possible in general SUSY models, one usually introduces an additional symmetry to prohibit some or all of the operators involved in these decays. One candidate is R-parity and searches for SUSY in ATLAS have largely been focussed on R_p conserving models with neutralinos or gravitinos as lightest supersymmetric particles in the past, motivated by the interpretation of the escaping LSP as candidate for dark matter.

An equally well motivated and less restrictive alternative in the R_p violating case is baryon triality, which only prohibits the baryon number violating operators in the superpotential. This allows SUSY models to have charged and decaying LSPs and re-opens large parts of parameter space excluded in the R_p conserving case. In addition, the lepton number violating B_3 mSUGRA models can address the question of non-zero neutrino masses without introducing additional fields into the theory. One benchmark scenario for this class of models is BC1, sampling a part of the mSUGRA parameter space where the $\tilde{\tau}_1$ is the LSP and which is excluded in the R_p conserving case.

The goal of this thesis was to search for events compatible with the predictions of BC1 and similar models in ATLAS data. After initial studies with an existing grid of BC1-like model points, created for prior phenomenological analyses based on a generic detector simulation, the search was split into two parts. On the one hand an analysis of the expected SM backgrounds and the systematic uncertainties, which was done in cooperation with similar searches for R_p conserving SUSY, and on the other hand studies of an extension of the grid of BC1-like model points and an interpretation of the observations made in data in terms of these models.

Motivated, in the case of BC1-like scenarios, by the decay products of the LSP and a very good rejection of SM backgrounds, a final state with four leptons and $E_{\mathrm{T}}^{\mathrm{miss}}$ was chosen for the analysis. The dominant backgrounds were $t\bar{t}$ (plus vector boson), dibosons and $Z+$ jets and could be reduced further by introducing a Z-veto. The dominant systematic uncertainties were the often extremely small remaining MC statistics, the jet energy scale and resolution and the electron energy resolution. No event was found in the first $2.06\,\mathrm{fb}^{-1}$ of data taken by ATLAS at $\sqrt{s} = 7\,\mathrm{TeV}$ in 2011, where a total of 0.7 ± 0.8 events were predicted for the considered SM backgrounds in the signal region including the Z-veto (SR2). Since no significant excess of events was found, compared to the SM prediction, in SR2 upper limits ($95\,\%$, CL_s) were set at 3.0 signal events or equivalently at a visible cross section of $1.46\,\mathrm{fb}$ to still be compatible with the observation. This coincided with the expected limits.

To interpret these numbers in terms of models in the $m_{1/2}$–$\tan\beta$ parameter plane around BC1 a new grid of 224 points was defined and MC events were simulated for each of them. This became necessary because the collected integrated luminosity and the expected sensitivity range of the signal selection exceeded those used for the prior simulation-only studies. Although the search strategy was not optimized for the exact predictions of the BC1 scenario as in these studies, a comparable average overall signal selection efficiency was achieved for the benchmark point itself. In contrast to those studies, a moderate cut on $E_{\mathrm{T}}^{\mathrm{miss}}$ was used instead of a harder one on the sum of p_{T} of the four hardest jets. This reduced the dependence on the properties of jets in signal events, which previously posed a problem for the heavier SUSY spectra at higher $m_{1/2}$ values, where the assumption of dominantly strong production is not valid any more and where in addition higher boosts of jets from the decay chain can become a problem for the applied isolation criteria. Combined with the possibility to include softer leptons, this change lead to an increased selection efficiency for BC1-like models at higher $m_{1/2}$.

Due to slightly different predictions of the more recent version of the spectrum calculator used for the new grid of models (e.g. for the $\tilde{\tau}_1$ mass) and the increased range in $m_{1/2}$ and $\tan\beta$, it was also necessary to revisit the properties of the models most important for the search. The experimental bounds of the grid were adjusted as well, introducing an area excluded from the search due to small $\tilde{\tau}_1$ masses and using a more accurate procedure to express the LEP bound on the Higgs mass.

Since the predictions used for the SM backgrounds' cross sections were at least at the NLO level in the strong coupling, NLO(+NLL) cross sections and their uncertainties were computed

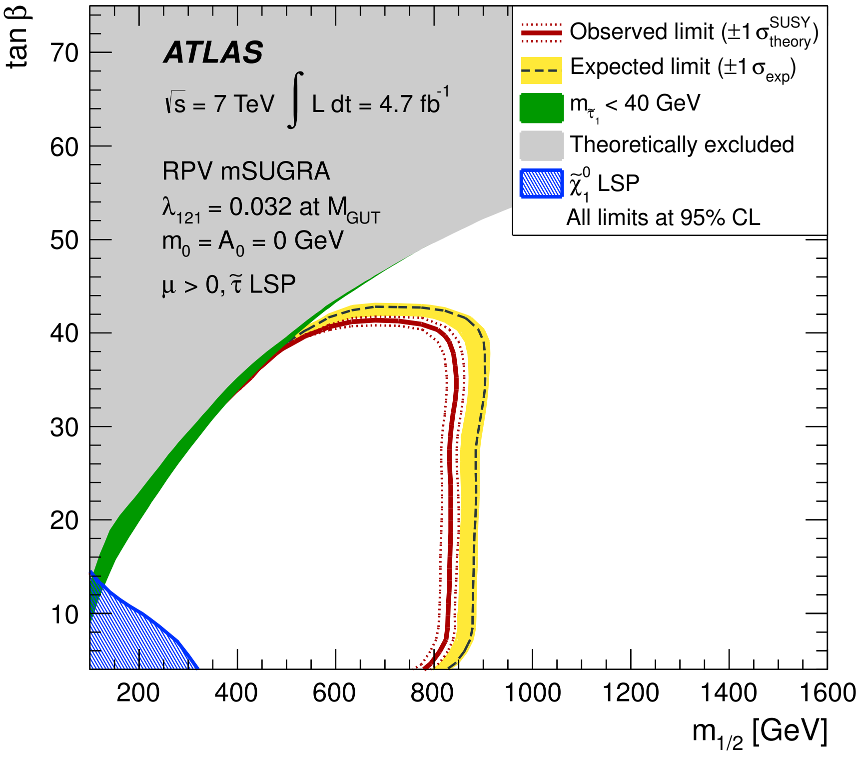

Figure 6.1: Observed and expected 95 % confidence level exclusion regions, calculated with the CL_s method for 4.7 fb^{-1}. [102]

for the BC1-like scenarios as well. Based on this, areas of dominantly strong, weak or direct slepton production were identified in the parameter plane. In addition to the sparticle masses, the lifetimes and decay modes of the lightest sparticles were examined as well. As expected, this revealed regions close to the high-tan β border of the grid where the $\tilde{\tau}_1$-lifetime is no longer compatible with the assumption of a prompt LSP decay or where the $\tilde{\tau}_1$ decays dominantly into two instead of four objects. Both of these effects restrict the range of the four lepton analysis in tan β direction. The overall effect of the studied properties can also be seen in the acceptance expected for the grid of signal models.

Finally, the number of expected signal events and its uncertainty at each point in the grid were combined with the result of the four lepton analysis to derive an excluded region in the parameter plane around BC1 using a frequentist method based on a profile likelihood ratio. At 95 % confidence level (CL_s) models with $m_{1/2} \lesssim 800$ GeV and tan $\beta \lesssim 40$ can be excluded. Within this framework this translates into a lower limit on gluino masses of about 1770 GeV.

The results found in this thesis were subsequently updated by ATLAS to the full 4.7 fb^{-1} of data taken at 7 TeV in 2011, using a newer version of the ATLAS software, with additional dilepton triggers and slightly changed object definitions on the analysis side. The corresponding exclusion region, as published in [102], is shown in Fig. 6.1 and roughly consistent with the expectation for the increase in integrated luminosity.

Generalized/simplified models, in which sparticle content, masses and branching ratios are more directly controlled, instead of being based on high-scale boundary conditions, are being studied by ATLAS as well. While not new for the R-parity conserving case, based on the experiences gained with the BC1-like models studied in this thesis, the effort was extended to $\not{R}_p$ models. In the context of multi-lepton models additional λ_{ijk} couplings are now covered, too.

With an increase in available statistics, a data-driven treatment of some of the SM backgrounds and uncertainty estimates has also become a viable option. And more recently the multi-lepton analysis for the 8 TeV dataset collected in 2012 has started including (non-leptonically decaying) τ leptons directly, as well.

Even though no significant excesses have been found in data so far, searches for signals indicating physics beyond the SM are still ongoing and will certainly benefit from the planned upgrades of the LHC and the detectors for running at 14 TeV.

Bibliography

[1] O. Bruning et al., eds., *LHC Design Report. 1. The LHC Main Ring*, CERN-2004-003-V-1, CERN-2004-003, 2004, URL: `https://cdsweb.cern.ch/record/782076`; O. Bruning et al., eds., *LHC Design Report. 2. The LHC infrastructure and general services*, CERN-2004-003-V-2, CERN-2004-003, 2004, URL: `https://cdsweb.cern.ch/record/815187`; M. Benedikt et al., eds., *LHC Design Report. 3. The LHC injector chain*, CERN-2004-003-V-3, CERN-2004-003, 2004, URL: `https://cdsweb.cern.ch/record/823808`; L. Evans and P. Bryant, "LHC Machine," *JINST* 3 (2008) S08001, DOI: `10.1088/1748-0221/3/08/S08001`.

[2] C. Lefèvre, "The CERN accelerator complex. Complexe des accélérateurs du CERN," Dec. 2008, URL: `https://cdsweb.cern.ch/record/1260465`.

[3] ATLAS Collaboration, G. Aad, et al., "The ATLAS Experiment at the CERN Large Hadron Collider," *JINST* 3 (2008) S08003, DOI: `10.1088/1748-0221/3/08/S08003`.

[4] CMS Collaboration, S. Chatrchyan, et al., "The CMS experiment at the CERN LHC," *JINST* 3 (2008) S08004, DOI: `10.1088/1748-0221/3/08/S08004`.

[5] LHCb Collaboration, J. Alves A. Augusto, et al., "The LHCb Detector at the LHC," *JINST* 3 (2008) S08005, DOI: `10.1088/1748-0221/3/08/S08005`.

[6] ALICE Collaboration, K. Aamodt, et al., "The ALICE experiment at the CERN LHC," *JINST* 3 (2008) S08002, DOI: `10.1088/1748-0221/3/08/S08002`.

[7] TOTEM Collaboration, G. Anelli, et al., "The TOTEM experiment at the CERN Large Hadron Collider," *JINST* 3 (2008) S08007, DOI: `10.1088/1748-0221/3/08/S08007`.

[8] LHCf Collaboration, O. Adriani, et al., "The LHCf detector at the CERN Large Hadron Collider," *JINST* 3 (2008) S08006, DOI: `10.1088/1748-0221/3/08/S08006`.

[9] MoEDAL Collaboration, "Technical Design Report of the MoEDAL Experiment," CERN-LHCC-2009-006, MoEDAL-TDR-001, CERN, June 2009, URL: `https://cds.cern.ch/record/1181486`.

[10] W. J. Stirling,
Standard Model cross sections as a function of collider energy, with 125 GeV Higgs, private communication,
URL: `http://www.hep.phy.cam.ac.uk/~wjs/plots/crosssections2012_v5.pdf`.

[11] R. R. Wilson, "The Tevatron," *Phys. Today* 30N10 (1977) 23–30.

[12] ATLAS Collaboration,
"ATLAS: Detector and physics performance technical design report. Volume 1,"
CERN-LHCC-99-14, ATLAS-TDR-14, 1999,
URL: `https://cdsweb.cern.ch/record/391176`; ATLAS Collaboration,
"ATLAS: Detector and physics performance technical design report. Volume 2,"
CERN-LHCC-99-15, ATLAS-TDR-15, 1999,
URL: `https://cdsweb.cern.ch/record/391177`.

[13] ATLAS Collaboration, G. Aad, et al.,
"Expected Performance of the ATLAS Experiment - Detector, Trigger and Physics,"
CERN-OPEN-2008-020, SLAC-R-980, 2009, arXiv:`0901.0512 [hep-ex]`.

[14] ATLAS Collaboration, "Luminosity Determination in pp Collisions at $\sqrt{s} = 7$ TeV using the ATLAS Detector in 2011," ATLAS-CONF-2011-116, CERN, Aug. 2011,
URL: `http://cdsweb.cern.ch/record/1376384`.

[15] ATLAS Collaboration, G. Aad, et al., "Luminosity Determination in pp Collisions at $\sqrt{s}$=7 TeV Using the ATLAS Detector at the LHC," *Eur. Phys. J. C* 71 (2011) 1630,
DOI: `10.1140/epjc/s10052-011-1630-5`, arXiv:`1101.2185 [hep-ex]`.

[16] ATLAS Collaboration, G. Aad, et al., "Improved luminosity determination in *pp* collisions at $\sqrt{s} = 7$ TeV using the ATLAS detector at the LHC,"
Eur. Phys. J. C 73 (2013) 2518, DOI: `10.1140/epjc/s10052-013-2518-3`,
arXiv:`1302.4393 [hep-ex]`.

[17] ATLAS Collaboration, *ATLAS Luminosity Public Results*, URL:
`https://twiki.cern.ch/twiki/bin/view/AtlasPublic/LuminosityPublicResults`.

[18] J. Beringer et al., "Review of Particle Physics (RPP)," *Phys. Rev. D* 86 (2012) 010001,
DOI: `10.1103/PhysRevD.86.010001`.

[19] F. Halzen and A. D. Martin,
Quarks and Leptons: An Introductory Course in Modern Particle Physics, 1984.

[20] D. Griffiths, *Introduction to Elementary Particles*, 2008.

[21] M. E. Peskin and D. V. Schroeder, *An Introduction to Quantum Field Theory*, 1995.

[22] H. Fritzsch, M. Gell-Mann, and H. Leutwyler,
"Advantages of the Color Octet Gluon Picture," *Phys. Lett.* B47 (1973) 365–368,
DOI: `10.1016/0370-2693(73)90625-4`.

[23] A. Martin et al., "Parton distributions for the LHC,"
Eur. Phys. J. C 63 (2009) 189–285, DOI: `10.1140/epjc/s10052-009-1072-5`,
arXiv:`0901.0002 [hep-ph]`.

[24] S. Glashow, "Partial Symmetries of Weak Interactions," *Nucl. Phys.* 22 (1961) 579–588, DOI: `10.1016/0029-5582(61)90469-2`; A. Salam and J. C. Ward, "Electromagnetic and weak interactions," *Phys. Lett.* 13 (1964) 168–171, DOI: `10.1016/0031-9163(64)90711-5`; S. Weinberg, "A Model of Leptons," *Phys. Rev. Lett.* 19 (1967) 1264–1266, DOI: `10.1103/PhysRevLett.19.1264`.

[25] P. W. Higgs, "Broken symmetries, massless particles and gauge fields," *Phys. Lett.* 12 (1964) 132–133, DOI: `10.1016/0031-9163(64)91136-9`; P. W. Higgs, "Broken Symmetries and the Masses of Gauge Bosons," *Phys. Rev. Lett.* 13 (1964) 508–509, DOI: `10.1103/PhysRevLett.13.508`; F. Englert and R. Brout, "Broken Symmetry and the Mass of Gauge Vector Mesons," *Phys. Rev. Lett.* 13 (1964) 321–323, DOI: `10.1103/PhysRevLett.13.321`.

[26] ATLAS Collaboration, G. Aad, et al., "Observation of a new particle in the search for the Standard Model Higgs boson with the ATLAS detector at the LHC," *Phys. Lett. B* 716 (2012) 1–29, DOI: `10.1016/j.physletb.2012.08.020`, arXiv:`1207.7214 [hep-ex]`.

[27] CMS Collaboration, S. Chatrchyan, et al., "Observation of a new boson at a mass of 125 GeV with the CMS experiment at the LHC," *Phys. Lett. B* 716 (2012) 30–61, DOI: `10.1016/j.physletb.2012.08.021`, arXiv:`1207.7235 [hep-ex]`.

[28] R. Peccei and H. R. Quinn, "Constraints Imposed by CP Conservation in the Presence of Instantons," *Phys. Rev. D* 16 (1977) 1791–1797, DOI: `10.1103/PhysRevD.16.1791`; R. Peccei and H. R. Quinn, "CP Conservation in the Presence of Instantons," *Phys. Rev. Lett.* 38 (1977) 1440–1443, DOI: `10.1103/PhysRevLett.38.1440`.

[29] J. Wess and B. Zumino, "A Lagrangian Model Invariant Under Supergauge Transformations," *Phys. Lett. B* 49 (1974) 52, DOI: `10.1016/0370-2693(74)90578-4`; J. Wess and B. Zumino, "Supergauge Transformations in Four-Dimensions," *Nucl. Phys. B* 70 (1974) 39–50, DOI: `10.1016/0550-3213(74)90355-1`.

[30] M. Drees, "An Introduction to supersymmetry," 1996, arXiv:`hep-ph/9611409 [hep-ph]`.

[31] S. P. Martin, "A Supersymmetry primer," 1997, arXiv:`hep-ph/9709356 [hep-ph]`.

[32] B. Allanach, A. Dedes, and H. Dreiner, "R parity violating minimal supergravity model," *Phys. Rev. D* 69 (2004) 115002, DOI: `10.1103/PhysRevD.69.115002,10.1103/PhysRevD.72.079902`, arXiv:`hep-ph/0309196 [hep-ph]`.

[33] H. K. Dreiner, C. Luhn, and M. Thormeier, "What is the discrete gauge symmetry of the MSSM?" *Phys. Rev. D* 73 (2006) 075007, DOI: `10.1103/PhysRevD.73.075007`, arXiv:`hep-ph/0512163 [hep-ph]`.

[34] Y. Kao and T. Takeuchi, "Single-Coupling Bounds on R-parity violating Supersymmetry, an update," 2009, arXiv:`0910.4980 [hep-ph]`.

[35] H. Dreiner, M. Hanussek, and S. Grab, "Bounds on R-parity Violating Couplings at the Grand Unification Scale from Neutrino Masses," *Phys. Rev. D* 82 (2010) 055027, DOI: `10.1103/PhysRevD.82.055027`, arXiv:`1005.3309 [hep-ph]`.

[36] H. Dreiner, M. Kramer, and B. O'Leary, "Bounds on R-parity violating supersymmetric couplings from leptonic and semi-leptonic meson decays," *Phys. Rev. D* 75 (2007) 114016, DOI: `10.1103/PhysRevD.75.114016`, arXiv:`hep-ph/0612278 [hep-ph]`.

[37] B. Allanach et al., "Mass Spectrum in R-Parity Violating mSUGRA and Benchmark Points," *Phys. Rev. D* 75 (2007) 035002, DOI: `10.1103/PhysRevD.75.035002`, arXiv:`hep-ph/0609263 [hep-ph]`.

[38] K. Desch et al., "Stau as the Lightest Supersymmetric Particle in R-Parity Violating SUSY Models: Discovery Potential with Early LHC Data," *Phys. Rev. D* 83 (2011) 015013, DOI: `10.1103/PhysRevD.83.015013`, arXiv:`1008.1580 [hep-ph]`.

[39] S. Ovyn, X. Rouby, and V. Lemaitre, "DELPHES, a framework for fast simulation of a generic collider experiment," 2009, arXiv:`0903.2225 [hep-ph]`.

[40] S. Fleischmann, "Tau lepton reconstruction with energy flow and the search for R-parity violating supersymmetry at the ATLAS experiment," CERN-THESIS-2011-291, BONN-IR-2012-09, URN: urn:nbn:de:hbz:5n-27310, PhD thesis: Rheinische Friedrich-Wilhelms-Universität, Bonn, 2012, URL: `http://hss.ulb.uni-bonn.de/diss_online`.

[41] ATLAS Collaboration, "Search for supersymmetry in events with four or more leptons and missing transverse momentum in pp collisions at $\sqrt{s} = 7$ TeV with the ATLAS detector," ATLAS-CONF-2012-001, CERN, Jan. 2012, URL: `https://cdsweb.cern.ch/record/1418920`.

[42] A. Ahmad et al., "Search for supersymmetry in events with four or more leptons and missing transverse momentum in pp collisions at $\sqrt{s} = 7$ TeV with the ATLAS detector," internal report ATL-PHYS-INT-2012-001, URL: `https://cdsweb.cern.ch/record/1418923`.

[43] G. Corcella et al., "HERWIG 6: An Event generator for hadron emission reactions with interfering gluons (including supersymmetric processes)," *JHEP* 0101 (2001) 010, DOI: `10.1088/1126-6708/2001/01/010`, arXiv:`hep-ph/0011363 [hep-ph]`; G. Corcella et al., "HERWIG 6.5 release note," 2002, arXiv:`hep-ph/0210213 [hep-ph]`; S. Moretti et al., "Implementation of supersymmetric processes in the HERWIG event generator," *JHEP* 0204 (2002) 028, arXiv:`hep-ph/0204123 [hep-ph]`.

[44] A. Sherstnev and R. S. Thorne, "Parton Distributions for LO Generators," *Eur. Phys. J. C* 55 (2008) 553–575, DOI: `10.1140/epjc/s10052-008-0610-x`, arXiv:`0711.2473 [hep-ph]`.

[45] ATLAS Collaboration, "Measurement of the $W^{\pm}Z$ Production Cross-Section in Proton-Proton Collisions at $\sqrt{s} = 7$ TeV with the ATLAS Detector," ATLAS-CONF-2011-099, CERN, July 2011, URL: `https://cdsweb.cern.ch/record/1369214`.

[46] J. Alwall et al., "MadGraph/MadEvent v4: The New Web Generation," *JHEP* 0709 (2007) 028, DOI: `10.1088/1126-6708/2007/09/028`, arXiv:`0706.2334 [hep-ph]`.

[47] ATLAS Collaboration, G. Aad, et al., "Measurement of Wgamma and Zgamma production in proton-proton collisions at $\sqrt{s} = 7$ TeV with the ATLAS Detector," *JHEP* 1109 (2011) 072, DOI: `10.1007/JHEP09(2011)072`, arXiv:`1106.1592 [hep-ex]`.

[48] P. M. Nadolsky et al., "Implications of CTEQ global analysis for collider observables," *Phys. Rev. D* 78 (2008) 013004, DOI: `10.1103/PhysRevD.78.013004`, arXiv:`0802.0007 [hep-ph]`.

[49] S. Moch and P. Uwer, "Theoretical status and prospects for top-quark pair production at hadron colliders," *Phys. Rev. D* 78 (2008) 034003, DOI: `10.1103/PhysRevD.78.034003`, arXiv:`0804.1476 [hep-ph]`.

[50] S. Moch and P. Uwer, "Heavy-quark pair production at two loops in QCD," *Nucl. Phys. Proc. Suppl.* 183 (2008) 75–80, DOI: `10.1016/j.nuclphysbps.2008.09.085`, arXiv:`0807.2794 [hep-ph]`.

[51] N. Kidonakis, "Next-to-next-to-leading-order collinear and soft gluon corrections for t-channel single top quark production," *Phys. Rev. D* 83 (2011) 091503, DOI: `10.1103/PhysRevD.83.091503`, arXiv:`1103.2792 [hep-ph]`.

[52] N. Kidonakis, "NNLL resummation for s-channel single top quark production," *Phys. Rev. D* 81 (2010) 054028, DOI: `10.1103/PhysRevD.81.054028`, arXiv:`1001.5034 [hep-ph]`.

[53] S. Frixione and B. R. Webber, "The MC@NLO 3.2 event generator," 2006, arXiv:`hep-ph/0601192 [hep-ph]`.

[54] A. Kardos, Z. Trocsanyi, and C. Papadopoulos, "Top quark pair production in association with a Z-boson at NLO accuracy," *Phys. Rev. D* 85 (2012) 054015, DOI: `10.1103/PhysRevD.85.054015`, arXiv:`1111.0610 [hep-ph]`.

[55] M. L. Mangano et al., "ALPGEN, a generator for hard multiparton processes in hadronic collisions," *JHEP* 0307 (2003) 001, DOI: `10.1088/1126-6708/2003/07/001`, arXiv:`hep-ph/0206293 [hep-ph]`.

[56] ATLAS Collaboration, G. Aad, et al., "Measurement of the production cross section for W-bosons in association with jets in pp collisions at $\sqrt{s} = 7$ TeV with the ATLAS detector," *Phys. Lett. B* 698 (2011) 325–345, DOI: `10.1016/j.physletb.2011.03.012`, arXiv:`1012.5382 [hep-ex]`.

[57] ATLAS Collaboration, G. Aad, et al.,
"Measurement of the production cross section for $Z/gamma^*$ in association with jets in pp collisions at $\sqrt{s} = 7$ TeV with the ATLAS detector,"
Phys. Rev. D 85 (2012) 032009, DOI: `10.1103/PhysRevD.85.032009`,
arXiv:`1111.2690 [hep-ex]`.

[58] ATLAS Collaboration, G. Aad, et al., "Measurement of the cross-section for b-jets produced in association with a Z boson at $\sqrt{s} = 7$ TeV with the ATLAS detector,"
Phys. Lett. B 706 (2012) 295–313, DOI: `10.1016/j.physletb.2011.11.059`,
arXiv:`1109.1403 [hep-ex]`.

[59] J. Butterworth, J. R. Forshaw, and M. Seymour,
"Multiparton interactions in photoproduction at HERA,"
Z. Phys. C 72 (1996) 637–646, DOI: `10.1007/s002880050286`,
arXiv:`hep-ph/9601371 [hep-ph]`.

[60] T. Sjostrand, S. Mrenna, and P. Z. Skands, "PYTHIA 6.4 Physics and Manual,"
JHEP 0605 (2006) 026, DOI: `10.1088/1126-6708/2006/05/026`,
arXiv:`hep-ph/0603175 [hep-ph]`.

[61] ATLAS Collaboration, G. Aad, et al., "The ATLAS Simulation Infrastructure,"
Eur. Phys. J. C 70 (2010) 823–874, DOI: `10.1140/epjc/s10052-010-1429-9`,
arXiv:`1005.4568 [physics.ins-det]`.

[62] GEANT4 Collaboration, S. Agostinelli, et al., "GEANT4: A Simulation toolkit,"
Nucl. Instrum. Meth. A 506 (2003) 250–303, DOI: `10.1016/S0168-9002(03)01368-8`.

[63] ATLAS Collaboration, G. Aad, et al., "Electron performance measurements with the ATLAS detector using the 2010 LHC proton-proton collision data,"
Eur. Phys. J. C 72 (2012) 1909, DOI: `10.1140/epjc/s10052-012-1909-1`,
arXiv:`1110.3174 [hep-ex]`.

[64] S. Hassani et al.,
"A muon identification and combined reconstruction procedure for the ATLAS detector at the LHC using the (MUONBOY, STACO, MuTag) reconstruction packages,"
Nucl. Instrum. Meth. A 572 (2007) 77–79, DOI: `10.1016/j.nima.2006.10.340`.

[65] ATLAS Collaboration, G. Aad, et al.,
"Studies of the performance of the ATLAS detector using cosmic-ray muons,"
Eur. Phys. J. C 71 (2011) 1593, DOI: `10.1140/epjc/s10052-011-1593-6`,
arXiv:`1011.6665 [physics.ins-det]`.

[66] ATLAS Collaboration, "Muon Momentum Resolution in First Pass Reconstruction of pp Collision Data Recorded by ATLAS in 2010,"
ATLAS-CONF-2011-046, ATLAS-COM-CONF-2011-003, 2011,
URL: `https://cdsweb.cern.ch/record/1338575`.

[67] M. Cacciari, G. P. Salam, and G. Soyez, "The Anti-k(t) jet clustering algorithm,"
JHEP 0804 (2008) 063, DOI: `10.1088/1126-6708/2008/04/063`,
arXiv:`0802.1189 [hep-ph]`.

[68] W. Lampl et al., "Calorimeter clustering algorithms: Description and performance,"
ATL-LARG-PUB-2008-002, ATL-COM-LARG-2008-003, 2008,
URL: `https://cdsweb.cern.ch/record/1099735`.

[69] ATLAS Collaboration, “Properties of Jets and Inputs to Jet Reconstruction and Calibration with the ATLAS Detector Using Proton-Proton Collisions at $\sqrt{s} = 7$ TeV,” ATLAS-CONF-2010-053, CERN, July 2010, URL: `https://cdsweb.cern.ch/record/1281310`.

[70] ATLAS Collaboration, G. Aad, et al., “Jet energy measurement with the ATLAS detector in proton-proton collisions at $\sqrt{s} = 7$ TeV,” *Eur. Phys. J. C* 73 (2013) 2304, DOI: `10.1140/epjc/s10052-013-2304-2`, arXiv:`1112.6426 [hep-ex]`.

[71] ATLAS Collaboration, G. Aad, et al., “Jet energy resolution in proton-proton collisions at $\sqrt{s} = 7$ TeV recorded in 2010 with the ATLAS detector,” *Eur. Phys. J. C* 73 (2013) 2306, DOI: `10.1140/epjc/s10052-013-2306-0`, arXiv:`1210.6210 [hep-ex]`.

[72] ATLAS Collaboration, *Update of the jet energy resolution for 2011 data*, 2013, URL: `https://twiki.cern.ch/twiki/bin/view/AtlasPublic/JetEtmissApproved2013Jer2011`.

[73] A. Ahmad et al., “Measurement of the cross-section for jets produced in association with a W-boson in pp collisions at $\sqrt{s} = 7$ TeV,” internal report ATL-PHYS-INT-2011-020, CERN, Mar. 2011, URL: `https://cdsweb.cern.ch/record/1334839`.

[74] ATLAS Collaboration, G. Aad, et al., “Measurement of the WW cross section in $\sqrt{s} = 7$ TeV pp collisions with ATLAS,” *Phys. Rev. Lett.* 107 (2011) 041802, DOI: `10.1103/PhysRevLett.107.041802`, arXiv:`1104.5225 [hep-ex]`.

[75] ATLAS Collaboration, G. Aad, et al., “Performance of Missing Transverse Momentum Reconstruction in Proton-Proton Collisions at 7 TeV with ATLAS,” *Eur. Phys. J. C* 72 (2012) 1844, DOI: `10.1140/epjc/s10052-011-1844-6`, arXiv:`1108.5602 [hep-ex]`.

[76] ATLAS Collaboration, “Performance of Missing Transverse Momentum Reconstruction in ATLAS with 2011 Proton-Proton Collisions at $\sqrt{s} = 7$ TeV,” ATLAS-CONF-2012-101, CERN, July 2012, URL: `https://cdsweb.cern.ch/record/1463915`.

[77] S. Heim et al., “Update of Electron Efficiency Plots (Sep 2013): For Approval,” ATL-COM-PHYS-2013-1287, CERN, Sept. 2013, URL: `https://cdsweb.cern.ch/record/1598869`.

[78] ATLAS Collaboration, “Determination of the muon reconstruction efficiency in ATLAS at the Z resonance in proton-proton collisons at $\sqrt{s}$=7 TeV,” ATLAS-CONF-2011-008, CERN, Feb. 2011, URL: `https://cdsweb.cern.ch/record/1330715`.

[79] ATLAS Collaboration, “Performance of the ATLAS Secondary Vertex b-tagging Algorithm in 7 TeV Collision Data,” ATLAS-CONF-2010-042, ATLAS-COM-CONF-2010-042, 2010, URL: `https://cdsweb.cern.ch/record/1277682`; ATLAS Collaboration, “Calibrating the b-Tag and Mistag Efficiencies of the SV0 b-Tagging Algorithm in 3 pb^{-1} of Data with the ATLAS Detector,” ATLAS-CONF-2010-099, ATLAS-COM-CONF-2010-103, 2010, URL: `https://cdsweb.cern.ch/record/1312145`.

[80] ATLAS Collaboration,
"Jet energy scale and its systematic uncertainty for jets produced in proton-proton collisions at $\sqrt{s} = 7$ TeV and measured with the ATLAS detector,"
ATLAS-CONF-2010-056, CERN, July 2010,
URL: `https://cdsweb.cern.ch/record/1281329`.

[81] ATLAS Collaboration, "Jet energy resolution and selection efficiency relative to track jets from in-situ techniques with the ATLAS Detector Using Proton-Proton Collisions at a Center of Mass Energy $\sqrt{s} = 7$ TeV," ATLAS-CONF-2010-054, CERN, July 2010,
URL: `https://cdsweb.cern.ch/record/1281311`.

[82] U. Langenfeld, S. Moch, and P. Uwer,
"New results for t anti-t production at hadron colliders," 2009,
arXiv:`0907.2527 [hep-ph]`.

[83] P. Nason,
"A New method for combining NLO QCD with shower Monte Carlo algorithms,"
JHEP 0411 (2004) 040, DOI: `10.1088/1126-6708/2004/11/040`,
arXiv:`hep-ph/0409146 [hep-ph]`; S. Frixione, P. Nason, and C. Oleari, "Matching NLO QCD computations with Parton Shower simulations: the POWHEG method,"
JHEP 0711 (2007) 070, DOI: `10.1088/1126-6708/2007/11/070`,
arXiv:`0709.2092 [hep-ph]`; S. Alioli et al., "A general framework for implementing NLO calculations in shower Monte Carlo programs: the POWHEG BOX,"
JHEP 1006 (2010) 043, DOI: `10.1007/JHEP06(2010)043`, arXiv:`1002.2581 [hep-ph]`.

[84] J. Campbell et al.,
"Normalizing Weak Boson Pair Production at the Large Hadron Collider,"
Phys. Rev. D 80 (2009) 054023, DOI: `10.1103/PhysRevD.80.054023`,
arXiv:`0906.2500 [hep-ph]`.

[85] B. Allanach, "SOFTSUSY: a program for calculating supersymmetric spectra,"
Comput. Phys. Commun. 143 (2002) 305–331, DOI: `10.1016/S0010-4655(01)00460-X`,
arXiv:`hep-ph/0104145 [hep-ph]`; B. Allanach and M. Bernhardt,
"Including R-parity violation in the numerical computation of the spectrum of the minimal supersymmetric standard model: SOFTSUSY,"
Comput. Phys. Commun. 181 (2010) 232–245, DOI: `10.1016/j.cpc.2009.09.015`,
arXiv:`0903.1805 [hep-ph]`.

[86] F. E. Paige et al.,
"ISAJET 7.69: A Monte Carlo event generator for pp, anti-p p, and e^+e^- reactions,"
2003, arXiv:`hep-ph/0312045 [hep-ph]`.

[87] ATLAS Collaboration, "Constraining R-parity violating Minimal Supergravity with $\tilde{\tau}_1$ LSP in a four lepton final state with missing transverse momentum,"
ATLAS-CONF-2012-035, CERN, Mar. 2012,
URL: `https://cdsweb.cern.ch/record/1432202`.

[88] ATLAS Collaboration et al., "The simulation principle and performance of the ATLAS fast calorimeter simulation FastCaloSim,"
ATL-PHYS-PUB-2010-013, ATL-COM-PHYS-2010-838, 2010,
URL: `https://cdsweb.cern.ch/record/1300517`.

[89] S. Heinemeyer, W. Hollik, and G. Weiglein, "FeynHiggs: A Program for the calculation of the masses of the neutral CP even Higgs bosons in the MSSM," *Comput. Phys. Commun.* 124 (2000) 76–89, DOI: `10.1016/S0010-4655(99)00364-1`, arXiv:`hep-ph/9812320 [hep-ph]`; S. Heinemeyer, W. Hollik, and G. Weiglein, "The Masses of the neutral CP - even Higgs bosons in the MSSM: Accurate analysis at the two loop level," *Eur. Phys. J. C* 9 (1999) 343–366, DOI: `10.1007/s100529900006`, arXiv:`hep-ph/9812472 [hep-ph]`; G. Degrassi et al., "Towards high precision predictions for the MSSM Higgs sector," *Eur. Phys. J. C* 28 (2003) 133–143, DOI: `10.1140/epjc/s2003-01152-2`, arXiv:`hep-ph/0212020 [hep-ph]`; M. Frank et al., "The Higgs Boson Masses and Mixings of the Complex MSSM in the Feynman-Diagrammatic Approach," *JHEP* 0702 (2007) 047, DOI: `10.1088/1126-6708/2007/02/047`, arXiv:`hep-ph/0611326 [hep-ph]`.

[90] P. Bechtle et al., "HiggsBounds: Confronting Arbitrary Higgs Sectors with Exclusion Bounds from LEP and the Tevatron," *Comput. Phys. Commun.* 181 (2010) 138–167, DOI: `10.1016/j.cpc.2009.09.003`, arXiv:`0811.4169 [hep-ph]`; P. Bechtle et al., "HiggsBounds 2.0.0: Confronting Neutral and Charged Higgs Sector Predictions with Exclusion Bounds from LEP and the Tevatron," *Comput. Phys. Commun.* 182 (2011) 2605–2631, DOI: `10.1016/j.cpc.2011.07.015`, arXiv:`1102.1898 [hep-ph]`, URL: `http://www.ippp.dur.ac.uk/HiggsBounds`.

[91] P. Z. Skands et al., "SUSY Les Houches accord: Interfacing SUSY spectrum calculators, decay packages, and event generators," *JHEP* 0407 (2004) 036, DOI: `10.1088/1126-6708/2004/07/036`, arXiv:`hep-ph/0311123 [hep-ph]`.

[92] B. Allanach et al., "SUSY Les Houches Accord 2," *Comput. Phys. Commun.* 180 (2009) 8–25, DOI: `10.1016/j.cpc.2008.08.004`, arXiv:`0801.0045 [hep-ph]`.

[93] W. Beenakker et al., "Squark and gluino production at hadron colliders," *Nucl. Phys. B* 492 (1997) 51–103, DOI: `10.1016/S0550-3213(97)00084-9`, arXiv:`hep-ph/9610490 [hep-ph]`; W. Beenakker et al., "Stop production at hadron colliders," *Nucl. Phys. B* 515 (1998) 3–14, arXiv:`hep-ph/9710451 [hep-ph]`; W. Beenakker et al., "The Production of charginos / neutralinos and sleptons at hadron colliders," *Phys. Rev. Lett.* 83 (1999) 3780–3783, DOI: `10.1103/PhysRevLett.100.029901,10.1103/PhysRevLett.83.3780`, arXiv:`hep-ph/9906298 [hep-ph]`; M. Spira, "Higgs and SUSY particle production at hadron colliders," 2002 217–226, arXiv:`hep-ph/0211145 [hep-ph]`; T. Plehn, "Measuring the MSSM Lagrangean," *Czech. J. Phys.* 55 (2005) B213–B220, arXiv:`hep-ph/0410063 [hep-ph]`.

[94] A. Kulesza and L. Motyka, "Threshold resummation for squark-antisquark and gluino-pair production at the LHC," *Phys. Rev. Lett.* 102 (2009) 111802, DOI: `10.1103/PhysRevLett.102.111802`, arXiv:`0807.2405 [hep-ph]`; A. Kulesza and L. Motyka, "Soft gluon resummation for the production of gluino-gluino and squark-antisquark pairs at the LHC," *Phys. Rev. D* 80 (2009) 095004, DOI: `10.1103/PhysRevD.80.095004`, arXiv:`0905.4749 [hep-ph]`; W. Beenakker et al.,

"Soft-gluon resummation for squark and gluino hadroproduction," *JHEP* 0912 (2009) 041, DOI: `10.1088/1126-6708/2009/12/041`, arXiv:`0909.4418 [hep-ph]`; W. Beenakker et al., "Squark and gluino hadroproduction," *Int. J. Mod. Phys. A* 26 (2011) 2637–2664, DOI: `10.1142/S0217751X11053560`, arXiv:`1105.1110 [hep-ph]`; W. Beenakker et al., "Supersymmetric top and bottom squark production at hadron colliders," *JHEP.* 1008 (2010) 098, arXiv:`1006.4771 [hep-ph]`.

[95] P. M. Nadolsky et al., "Implications of CTEQ global analysis for collider observables," *Phys. Rev. D* 78 (2008) 013004, DOI: `10.1103/PhysRevD.78.013004`, arXiv:`0802.0007 [hep-ph]`.

[96] M. Botje et al., "The PDF4LHC Working Group Interim Recommendations" (2011), arXiv:`1101.0538 [hep-ph]`.

[97] M. Kramer et al., "Supersymmetry production cross sections in *pp* collisions at $\sqrt{s} = 7$ TeV," 2012, arXiv:`1206.2892 [hep-ph]`.

[98] H. Dreiner, S. Grab, and M. Trenkel, "$S\tau$ LSP Phenomenology: Two versus Four-Body Decay Modes. Example: Resonant Single Slepton Production at the LHC," *Phys. Rev. D* 79 (2009) 016002, DOI: `10.1103/PhysRevD.79.016002,10.1103/PhysRevD.79.019902`, arXiv:`0808.3079 [hep-ph]`.

[99] G. Cowan et al., "Asymptotic formulae for likelihood-based tests of new physics," *Eur. Phys. J. C* 71 (2011) 1554, DOI: `10.1140/epjc/s10052-011-1554-0`, arXiv:`1007.1727 [physics.data-an]`.

[100] R. Bruneliere et al., "Setting exclusion limits in ATLAS supersymmetry searches with a likelihood ratio based method," internal report ATL-PHYS-INT-2011-032, CERN, Apr. 2011, URL: `https://cdsweb.cern.ch/record/1342545`.

[101] A. L. Read, "Presentation of search results: The CL_s technique," *J. Phys. G* 28 (2002) 2693–2704, DOI: `10.1088/0954-3899/28/10/313`.

[102] ATLAS Collaboration, G. Aad, et al., "Search for R-parity-violating supersymmetry in events with four or more leptons in $\sqrt{s} = 7$ TeV *pp* collisions with the ATLAS detector," *JHEP* 1212 (2012) 124, DOI: `10.1007/JHEP12(2012)124`, arXiv:`1210.4457 [hep-ex]`.

List of Figures

List of Tables

Acknowledgements

First of all I would like to thank Klaus Desch for his support and patience and for giving me the opportunity to work not only on one, but two very different and interesting topics, even if the first one didn't make it into this thesis.

Sebastian Fleischmann, Sebastian Grab, Tim Stefaniak and Herbie Dreiner deserve my gratitude for everything that violates R-parity, for providing general technical and theoretical background and many helpful insights and discussions about BSM models, prior studies of BC1 and bounds.

I'm indebted to Michael Flowerdew for picking up the reigns during my absence and for bringing up and somehow keeping together the whole project of getting that interpretation CONF note out in time, which also would not have worked without the input of Tina Potter and Sigve Haug. None of this would have been possible, of course, without the work of the whole ATLAS SUSY multi-lepton group, the members of which I have to thank for "adopting" me and my part of the analysis into their otherwise neatly R_p conserving world.

For everything related to getting that Tier-3 grid site up and running, I'd like to thank Simon Nderitu, Peter Wienemann and the GridKa team, as well as all the people who are tirelessly keeping the WLCG up and running, so that physicists all over the world can "just" submit millions of jobs running over all that LHC data at 3am in the morning even on a public holiday. This gratitude of course extends to all sysadmins at the institute, Gizo Nanava and Helmut Kortmann, to pick just two, who I've had the pleasure of working with over the years.

All current and former members of the Desch and Brock groups, colleagues and friends, I'd like to thank for their help, many fruitful discussions and a whole bunch of fun of the type that makes for a nice overall work-experience.

Special thanks also to Verena Schönberg, Steffen Schaepe, Philip Bechtle and Till Nattermann for test-reading of and providing comments on parts of the manuscript.

Finally, I'd like to express my gratitude to my parents and to Melanie Klöß, for their love and for always supporting me.